## ABSTRACT

## NEAR-FIELD IMAGING WITH TERAHERTZ PULSES

**by**
**Oleg Mitrofanov**

High spatial resolution imaging is implemented with a novel collection mode near-field terahertz (THz) probe. Exceptional sensitivity of the probe allows imaging with spatial resolution of few microns using THz pulses with spectral content of 120 to 1500 microns. In the present study, the principle of the probe operation as well as the probe design and characteristics are described.

The probe performance is related to effective detection of radiation coupled into the probe aperture. Propagation of short single-cycle electromagnetic pulses through apertures as small as 1/300 of the wavelength is experimentally and numerically studied. Finite-difference time-domain method is used to model propagation of THz pulses through the probe aperture in order to optimize the probe design. It is shown that the probe sensitivity is significantly improved if the detecting antenna measures electric field coupled through the aperture in the near-field zone rather than in the far-field zone. Effects of temporal and spectral pulse shaping are described by frequency-dependent transmission at the near- or below cutoff regimes of the aperture. Imaging schemes, properties, and artifacts are considered. The technique provides the best to date spatial resolution capabilities in the THz range of the electromagnetic spectrum.

# NEAR-FIELD IMAGING WITH TERAHERTZ PULSES

by
**Oleg Mitrofanov**

**A Dissertation**
**Submitted to the Faculty of**
**New Jersey Institute of Technology and**
**Rutgers, The State University of New Jersey – Newark**
**in Partial Fulfillment of the Requirements of the Degree of**
**Doctor of Philosophy**

**Federated Physics Department**

**May 2001**

**APPROVAL PAGE**

**NEAR-FIELD IMAGING**
**WITH TERAHERTZ PULSES**

**Oleg Mitrofanov**

---

Dr. John F. Federici, Dissertation Advisor — Date
Associate Professor of Physics, NJIT

---

Dr. Anthony M. Johnson — Date
Chairperson and Distinguished Professor of Physics, NJIT

---

Dr. Mark Lee — Date
Member of Technical Staff, Bell Laboratories, Lucent Technologies,
Murray Hill, NJ

---

Dr. Edip Niver — Date
Associate Professor of Electrical and Computer Engineering, NJIT

---

Dr. Earl D. Shaw — Date
Chairperson and Professor of Physics, Rutgers – Newark

## BIOGRAPHICAL SKETCH

**Author:** Oleg Mitrofanov

**Degree:** Doctor of Philosophy

**Date:** May 2001

**Undergraduate and Graduate Education:**

- Doctor of Philosophy in Applied Physics,
  New Jersey Institute of Technology, Newark, NJ, 2001

- Master of Science in Materials Science and Engineering,
  New Jersey Institute of Technology, Newark, NJ, 1998

- Bachelor of Science in Physics,
  Moscow State University, Moscow, Russia, 1997

**Major:** Applied Physics

**Presentations and Publications:**

O. Mitrofanov, M. Lee, J. W. P. Hsu, L. N. Pfeiffer, K. W. West, J. D. Wynn, and J. F. Federici, 'Terahertz Pulse Propagation through Small Apertures', submitted to Appl. Phys. Lett.

O. Mitrofanov, R. Harel, M. Lee, J. W. P. Hsu, J. D. Wynn, and J. Federici, 'Design Optimization of Terahertz Near-Field Detectors', submitted to OSA TOPS on Ultrafast Electronics and Optoelectronics.

O. Mitrofanov, M. Lee, J. W. P. Hsu, I. Brener, R. Harel, J. Federici, J. D. Wynn, L. N. Pfeiffer, and K. W. West, 'Collection mode near-field imaging with 0.5 THz pulses', submitted to J. Select. Top. in Quantum Electronics, Ultrafast Phenomena.

O. Mitrofanov, R. Harel, M. Lee, L. N. Pfeiffer, K. W. West, J. D. Wynn, and J. Federici, 'THz transmission near-field imaging with very high spatial resolution', CLEO 2001.

O. Mitrofanov, R. Harel, M. Lee, J. D. Wynn, and J. Federici, 'Design Optimization of Terahertz Near-Field Detectors', UEO 2001.

J. Federici, O. Mitrofanov, I. Brener, R. Harel, M. Lee, J. D. Wynn, L. N. Pfeiffer, and K. W. West, 'Far-Infrared Near Field Microscopy', LEOS 2000.

O. Mitrofanov, R. Harel, M. Lee, L. N. Pfeiffer, K. W. West, J. D. Wynn, and J. Federici,' Study of Single-Cycle Pulse Propagation inside a Terahertz Near-Field Probe', Appl. Phys. Lett. 78, 252-54 (2001).

O. Mitrofanov, R. Harel, M. Lee, L. N. Pfeiffer, K. W. West, J. D. Wynn, and J. Federici, 'Terahertz near-field microscopy based on a collection mode detector', Appl. Phys. Lett. 77, 3496-98 (2000).

O. Mitrofanov, I. Brener, M. Wanke, R. R. Ruel, J. D. Wynn, A. J. Bruce, and J. Federici, 'Near-field microscope probe for far infrared time domain measurements', Appl. Phys. Lett. 77, 591-93 (2000).

O. Mitrofanov, I. Brener, M. C. Wanke, R. R. Ruel, J. D. Wynn, A. J. Bruce, and J. Federici, 'Thin terahertz detectors and emitters based on low temperature grown GaAs on sapphire', CLEO 2000.

To my father

## ACKNOWLEDGMENT

I would like to express my appreciation to Dr. John F. Federici, Dr. Mark Lee, and Dr. Igal Brener, who served as my research advisors, providing valuable guidance, insight, and support over the years of my studies. Special thanks are given to Dr. Anthony M. Johnson, Dr. Edip Never, and Dr. Earl D. Shaw for actively participating in my committee.

Most of this work has been accomplished using facilities at Bell Laboratories, Lucent Technologies at Murray Hill, NJ. I would like to acknowledge Richart E. Slusher, the director of the Optical Physics Research Department, for support, as well as Roey Harel, James D. Wynn, Mike C. Wanke, Sanghee Hui, Rafi DePicciotto, Hugo Safar, Andrea Markelz, Anthony L. Campillo, William H. Burkett, Loren N. Pfeiffer, and Ken W. West, who assisted me and participated in useful discussions. I particularly wish to thank Julia W. P. Hsu for very productive discussions.

Special thanks to my father, Valeriy Mitrofanov, for continuous encouragement and support. I also would like to acknowledge Vladimir Braginsky for insight and interesting conversations. Lastly, my deepest appreciation is given to my beloved family and Olya, who supported me over these years of research.

## TABLE OF CONTENTS

## TABLE OF CONTENTS
## (Continued)

## TABLE OF CONTENTS
## (Continued)

## LIST OF TABLES

## LIST OF FIGURES

## LIST OF FIGURES
## (Continued)

## LIST OF FIGURES
## (Continued)

## LIST OF FIGURES
## (Continued)

## LIST OF FIGURES
## (Continued)

## LIST OF FIGURES
## (Continued)

## LIST OF FIGURES
## (Continued)

# CHAPTER 1

# INTRODUCTION

After the first demonstration of imaging with far-infrared, or terahertz (THz), pulses in 1995 by Hu and Nuss, the question of spatial resolution has remained at the far front of THz research. Far-infrared radiation is characterized by a long wavelength, typically 100-1,500 $\mu$m. Imaging of objects, whose size is smaller than the wavelength, is not possible with conventional techniques because of diffraction. According to Abbe's theory, which describes image formation by the superposition of interference fringes, the highest possible spatial resolution is $\sim\lambda/2$ [for example, Reynolds *et al.* 1989, or Born & Wolf 1999]. Solid immersion lenses provide improvement by a factor of $n$, where $n$ is a refractive index of the lens, but it is usually not sufficient for a wavelength of few hundred microns. An obvious solution is application of alternative methods such as near-field imaging [Pohl *et al.* 1991].

Optical near-field microscopy is widely used, when resolution of 1/10–1/20 of the wavelength is required. The concept of near-field imaging includes a variety of methods, which share one common feature: the technique employs interaction of the sample and a small external object (a subwavelength aperture or a sharp metallic tip [Knoll & Keilmann 2000]) placed in the near-zone of the sample. The optical field in the near-zone ($r<<\lambda$) reflects local properties of the sample. If a small object is introduced in the near-zone, the local optical field is perturbed both by the object and the sample. A measure of this perturbation reflects the local optical field and, therefore, the sample properties.

In order to construct the near-field image, the external object is scanned with respect to the sample and their interaction is measured for every position of the object. The spatial resolution of this imaging method is determined by the characteristic interaction length.

In the most common aperture-type near-field microscopy, a probe with a small aperture is introduced into the near zone of the sample. The aperture either illuminates the sample or it collects the light transmitted or scattered by the sample (the arrangements are referred to as the illumination and collection mode respectively). The aperture serves to confine the incident electromagnetic field in the first case and to sample the scattered field in the second case. The amount of light that couples through the aperture depends on the optical properties of the sample in the point where the aperture is placed. Spatial resolution of this method is determined by the size of the aperture or, to be exact, by its effective size [Durig *et al.* 1986]. Electromagnetic waves are known to penetrate into metal [Jackson 1962]. As a result, the field in the plane of the aperture is not confined by its physical boundary, but extends outside by the value of the penetration depth. At a frequency of 1 THz the penetration depth of gold is ~50 nm and, in principle, light can be confined to a size smaller than 1 $\mu$m ($\sim\lambda/300$) using a small aperture. Therefore, the aperture-type near-field microscopy potentially is capable of high-resolution imaging.

Despite the fact that resolution is independent of the wavelength in the near-field imaging, it is a challenge to build an instrument with resolution better than $\lambda/20$. The main reason is a low throughput of a subwavelength aperture. A circular hole in a thin metallic screen with diameter $d=\lambda/20$ transmits $\sim 10^{-6}$ of the total power in a beam focused on the hole. Further reduction of the aperture size decreases the transmission at the rate of

the $d^6$ law [Bethe 1944]. Consequently, the intensity of light transmitted through the aperture rapidly drops to a level, at which detection is not possible.

High intensity sources do not solve the problem because a fraction of the incident power transmits through the aperture screen. The intensity of this wave eventually exceeds the signal transmitted through the aperture as the aperture size decreases. By making the screen thicker, transmission through the screen decreases, however, transmission through the aperture decreases as well, since the aperture acts as an undersized waveguide, which exponentially reduces the wave intensity along its length. When the screen thickness becomes comparable with the aperture size, this attenuation mechanism becomes important and the intensity reduces much faster than the $d^6$ law as $d$ decreases. The required optical power increases exponentially and implementation of the very small aperture becomes impractical.

Extremely strong attenuation of waves transmitted through a subwavelength aperture limits the spatial resolution. In the visible near-field imaging, the resolution on the order of $\sim\lambda/20$ is sufficient for many applications since the wavelength is short (few hundred nanometers). In the terahertz (THz) regime, however, the wavelength is so large that desired resolution is less than 1/100 of the wavelength. The scope of this work is to investigate possibilities of very high resolution imaging with THz waves. In the course of this study, a near-field probe, which provides a better resolution than the conventional near-field technique, has been developed. It was demonstrated that spatial resolution as high as 7 $\mu$m at wavelengths of 120-1500 $\mu$m is possible with signal-to-noise ratio >10.

The advantage of the developed collection mode probe design is that the detecting element is located in the near-zone of the probe aperture. It is known that electromagnetic

energy is mostly concentrated in the near-zone (at the distance from the aperture smaller than the aperture size) [Leviatan 1986]. This energy exists in evanescent modes and does not propagate into the far-field zone ($z>>\lambda$) [Grober *et al.* 1996]. The conventional near-field scanning optical microscope (NSOM) setup only detects light transmitted to the far-field zone. In the numerical and experimental studies of electromagnetic pulse propagation through small apertures, it has been shown that evanescent modes dominate at distance $z<d/2$. The intensity of electric field within this region is significantly larger than in the far-field.

Due to relatively long wavelengths of THz waves, it is possible to implement the idea of near-field detection by fabricating a probe with a few micron large aperture and a detecting element located at a short distance $L<d$ from it. For instance, a photoconducting antenna, which is essentially a planar structure ~1-2 $\mu$m thick, is well suited for his purpose. A novel fabrication process, which allows building near-field probes with lithographically defined apertures and the controlled separation between the aperture and the detecting element has been developed. The sensitivity of these probes is shown to improve by 1-2 orders of magnitude. In addition, the antenna measures electric field of the radiation rather than the intensity. The electric field decreases only as the third power of the aperture size $d$ (the intensity decreases as $d^{6}$). Therefore attenuation of the signal measured using our probe is not as severe as in the conventional probe.

THz near-field probes with an aperture as small as 5 $\mu$m (which is smaller than $\lambda/100$ for the central wavelength) has been fabricated and tested. Spatial resolution of the probes is defined by the aperture size and independent of wavelength throughout the

spectrum of the THz pulses (120-1500 $\mu$m). A record-high resolution of 7 $\mu$m has been demonstrated in collection mode. Performance of the probes has been evaluated.

Electromagnetic pulses, especially the THz pulses, which have large fractional bandwidth, experience spectral and temporal deformation as they transmit through the subwavelength aperture of the probe (the aperture size is smaller than the central wavelength). Transmission is wavelength dependent and different spectral components transmit with different amplitude. In order to study these effects, a numerical method based on two-dimensional finite-difference time-domain algorithm has been developed to model the THz pulse coupling into the near-field probe. The simulation has shown a good agreement with experimental measurements of the waveforms and spectra. The numerical method allows studying coupling of THz pulses of an arbitrary waveform and spectrum into the near-field probe, geometry of which can be modeled as well.

Any object in front of the aperture alters the pulse coupling into the probe. In order to interpret near-field images, the transmission through the aperture has to be well understood first. The spectral and temporal transformation of the THz pulses in the process of transmission through a subwavelength aperture has been described. Depending on the aperture size the spectrum width changes and the central wavelength usually shifts to the shorter values. The pulse duration changes as well, resulting in effects of pulse compression and temporal advancing. It has been demonstrated that these effects are described by wavelength dependent transmission through the aperture.

Reconstruction of the sample properties from a near-field image is a difficult task, since many parameters such as illumination conditions, field polarization, topography of the sample, its composition, size, and shape affect the process of image formation.

Interaction of the sample with the optical field and the probe is a basis of the near-field imaging and, to our knowledge, it has not been studied in detail for THz pulses. Description of basic properties of THz near-field imaging, and experimental demonstration near-field effects, such as variation of signal amplitude with the probe-sample separation, shallow depth of field, and polarization sensitive image formation is presented in this work. It is shown that analysis of entire time-domain information is required for accurate image interpretation.

This work is presented in seven chapters including Introduction and Conclusion and two appendices. Terahertz time-domain spectroscopy technique (THz TDS), its principle, possibilities and limitations are described in Chapter 2. Imaging in THz waves is discussed in Chapter 3, where the concept of the collection mode near-field probe is introduced. Design of the near-field probe, the issue of efficient coupling of THz pulses, and details of fabrication are presented in Chapter 4. Propagation of single-cycle THz pulses through subwavelength apertures and effects of pulse shaping and spectrum deformation are discussed in Chapter 5. The limit of spatial resolution of the technique is analyzed in that chapter as well. Chapter 6 is devoted to near-field imaging, where the system properties, image artifacts, and methods of image analysis are presented. The appendices discuss in detail characterization of the photoconducting material for THz dertectors (Appendix A) and one-dimensional finite-difference algorithm for the THz pulse propagation modeling (Appendix B).

# CHAPTER 2

# TERAHERTZ TIME DOMAIN SPECTROSCOPY

## 2.1 Introduction

The far-infrared, or terahertz, part of electromagnetic spectrum is one of the least explored. Until recently, the main reason for the low attention to physical phenomena at this frequency range had been a lack of efficient sources and detectors. Development of the Terahertz Time Domain Spectroscopy (THz-TDS) technique induced considerable interest in the spectral range of 0.1-2.0 THz [for example, Nuss & Orenstain 1998]. The advantages of the THz-TDS are the exceptional sensitivity and the possibility to access the amplitude and phase information of the propagating THz waves. In addition, THz-TDS is a broad-band technique and it provides the possibility of complete characterization of the dielectric function of materials in the terahertz regime. In this chapter an overview of THz TDS technique is given, its principle, possibilities, and limitations are discussed.

## 2.2 The Principle of THz TDS Technique

### 2.2.1 Spectral Analysis

THz TDS technique is based on measurements of short electromagnetic pulses, which are deformed due to transmission or reflection from a sample. If a pulse propagates through a medium, its waveform and spectrum change due to dispersion and absorption. Most media are dispersive (i.e. the dielectric constant is a function of frequency of the field) and the phase velocity is not the same for each frequency component of the pulse.

Consequently different components travel with different speeds and tend to change phase with respect to one another. This leads to a change in the shape of a pulse as it travels. Frequency (Fourier) analysis of the pulse waveform allows characterization of the medium dispersion.

In THz regime, many media are dissipative as well. A travelling THz wave can excite vibrational or rotational modes of molecules, for example water molecules [Cheville & Grischkowsky 1999] or proteins [Markelz 2000]. The dissipative effects are usually functions of frequency of the field and traveling pulse experiences distortion along with attenuation. The distortion usually appears in long lasting electric field oscillations, which follow the field transient of the pulse and/or in attenuation of the pulse amplitude.

As an example, Figure 2.1 demonstrates the effects of transmission on the waveform and spectrum of the single-cycle pulse. The medium is characterized by a single absorption line. Since the medium absorbs electromagnetic waves only at particular frequency $\omega_0$, and otherwise is absolutely transparent, most of the spectral components of the pulse propagate through the medium without a change. At frequency $\omega_0$, however, the electromagnetic pulse excites the molecules, for example into their rotational states. The coherent ensemble of molecules rotates with rotational frequency and remits THz radiation after the external force (the incident pulse) disappears. This emission is seen in the time-domain as slowly decaying electric field oscillations at frequency $\omega_0$. Collision between the molecules of the ensemble causes dephasing and a corresponding decay of the emitted THz radiation (and line broadening in the frequency domain).

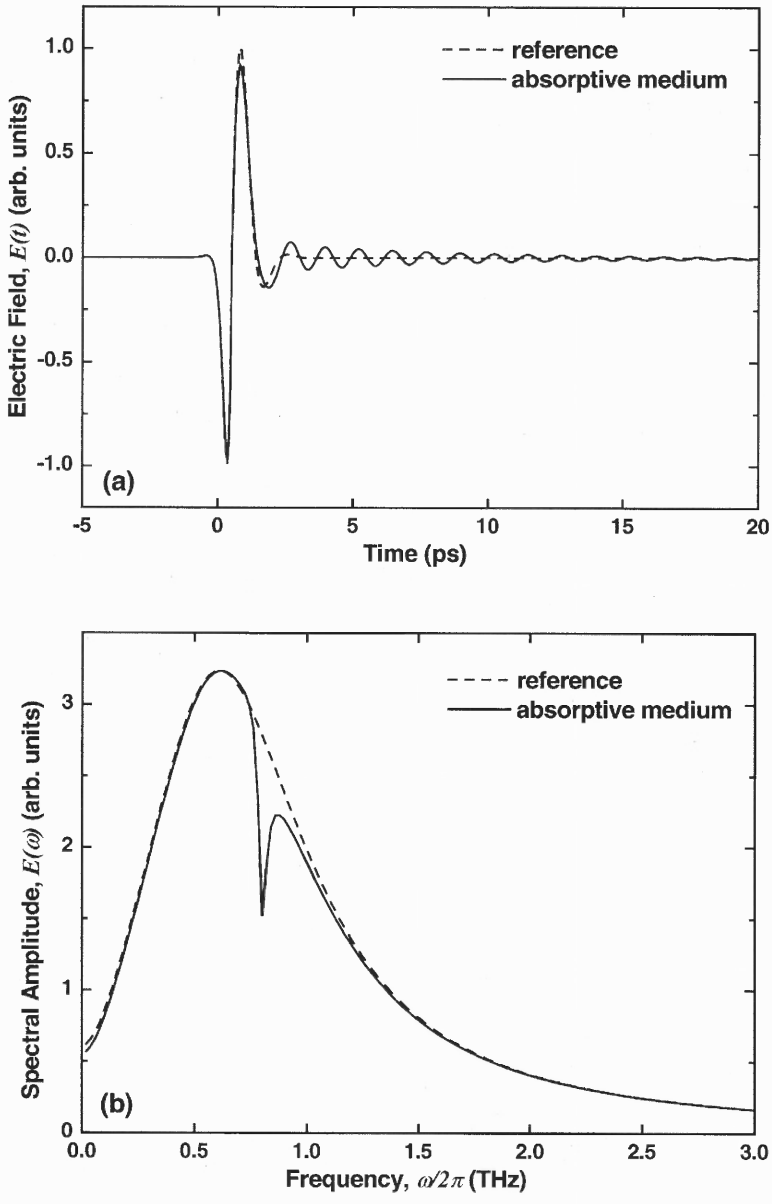


**Fig. 2.1.** The time domain waveform (a) and the spectral amplitude (b) of a short electromagnetic pulse transmitted through a medium with one absorption line at $\omega_0/2\pi$=0.8 THz. The incident characteristics are shown by the dashed curves. The waveform exhibits electric field oscillations at frequency $\omega_0$ lasting after the incident pulse transient. In the frequency domain the spectrum contains a distinctive absorption line.

The optical properties of the medium are directly obtained from the time-domain measurements. The electric field transient can be expressed as a superposition of monochromatic waves.

$$E(t) = \frac{1}{\sqrt{2\pi}} \int_{-\infty}^{\infty} E(\omega) e^{-i\omega t} d\omega \tag{2.1}$$

$E(\omega)$ is a complex function and it is given by the Fourier transform of the time domain waveform $E(t)$

$$E(\omega) = \frac{1}{\sqrt{2\pi}} \int_{-\infty}^{\infty} E(t) e^{i\omega t} dt \tag{2.2}$$

The complex amplitude can be expressed in an exponential form, where the absolute value of $E(\omega)$ describes the weight of spectral components in the pulse

$$E(\omega) = |E(\omega)| e^{i\varphi(\omega)} \tag{2.3}$$

Separation of two frequency dependent parameters, the amplitude and the phase, allows the use of the time domain measurements for the sample characterization at different frequencies simultaneously. In further discussions, the absolute value notation will be omitted and $E(\omega)$ will be referred to the absolute value of the spectral amplitude.

Next, consider the waveform and the spectrum of the pulse as it passes through a linear medium with complex index of refraction $\hat{n}(\omega) = n(1 + i\kappa)$. The different spectral components propagate at different phase velocities and, in general, suffer attenuation along the path in the medium. After traveling distance $l$ the pulse waveform becomes

$$E(t,l) = \frac{1}{\sqrt{2\pi}} \int_{-\infty}^{\infty} E(\omega) e^{-\frac{\omega n \kappa l}{c}} e^{i\frac{\omega n l}{c}} e^{-i\omega t} d\omega \tag{2.4}$$

Using the exponential representation [Eq. 2.3], the real and imaginary parts of the index (or the dielectric function) are conveniently expressed in terms of the Fourier transforms [Eq. 2.2] of the pulse waveforms $E(t, x)$ and $E(t, x+l)$

$$\mathrm{Re}(\hat{n}(\omega)) = \frac{c}{\omega l}(\varphi(\omega,l) - \varphi(\omega)) \quad , \tag{2.5}$$

$$\mathrm{Im}(\hat{n}(\omega)) = \frac{c}{\omega l}\left|\ln\left(\frac{E(\omega,l)}{E(\omega)}\right)\right| . \tag{2.6}$$

According to the last equations, the complex refractive index of the media can be found using the experimentally measured amplitude and phase. The technique requires two measurements: a reference waveform, measured without the sample and, a second measurement, the waveform of the pulse, which interacts with the sample.

### 2.2.2 Spectral Resolution and Time-windowing of Data

Short optical pulses ($\tau$=100 fs) are used to measure the electric field of the THz pulse in the TDS setup. The field is sampled using either a gated photoconducting antenna or an electro-optic crystal [Cai *et al.* 1998]. The measured electric field corresponds to a moment when the optical pulse turns on the detector. The time-domain waveform is constructed by measuring the electric field as the time difference between the arrival of the THz pulse and the gating optical pulse at the detector is varied. When the instrument detects the peak electric field of the pulse, it is called to be in the zero time delay state. As the delay stage is moved and the time difference increases, the electric field of the pulse vanishes, corresponding to a later moment in time. Calibration of the time-axis is simply accomplished by transforming the delay stage displacement into the time delay.

The spectral resolution of the instrument is determined by the length of the recorded waveform [Nuss & Orenstein 1998]. THz pulses, as generated, are very short, lasting only a half- or single cycle. The only radiation contributing to the non-zero electric field after the pulse field vanishes is the individual absorption spectral peaks in the

medium of propagation [Fig. 2.1]. The peak width is inversely proportional to the time duration of the created field oscillations. A narrow time window allows detection of the broad spectral peaks. Contribution of the narrow band lines is measured by increasing the time-domain scan interval. Eventually, a few hundred of picoseconds after the pulse arrival, the waveform oscillations decay to the noise level. This time interval, $T$, limits the useful length of the waveform and, hence, the instrument spectral resolution, defined as the inverse of the interval

$$\Delta\nu = \frac{1}{T}. \tag{2.7}$$

A long time-domain scan is required for high spectral resolution THz TDS measurements.

Truncation of the waveform allows excluding some of the undesirable signals, such as substrate reflection, which arrive at the detector at a later time. In principle, this operation results in limited spectral resolution. However, it simplifies the post measurement analysis, since the pulse passes through the sample only once, provided that reflections from the sample interfaces do not overlap in time. Multiple beam interference effects can be removed also numerically.

### 2.2.3 Frequency Range of THz-TDS

Frequency range of the THz-TDS is directly related to the generation and detection of the THz pulses. Short electromagnetic pulses provide substantial fractional bandwidth. The frequency and time distributions of the pulse field are related [Jackson 1962]

$$\Delta\omega\Delta t \geq \frac{1}{2}. \tag{2.8}$$

The duration of the single cycle pulses $\Delta t$ is on the order of the inverse of the central frequency. Consequently, the fractional bandwidth $\frac{\Delta\omega}{\omega}$ can be larger than unity.

The lower frequency limit of the THz-TDS technique is defined, as the spectral resolution, by the measured temporal window. The upper limit, in principle, is determined by the time increment of the acquired data, but practically, it is limited by the detector speed, which depends on the detector type and will be discussed later. A typical THz-TDS system that uses photoconducting antennas as the THz pulse generator and detector provides a working range of 0.2–1.5 THz. Systems that use electro-optic sampling usually extend the upper limit to 2-3 THz (if 100 fs optical pulses are used), because the electro-optic detection scheme is not limited by the carrier relaxation dynamics in semiconductors.

## 2.3 THz Transmitters and Detectors

### 2.3.1 THz Transmitters

A number of various sources of the THz pulses has been developed over the past two decades [Cai 1998]. The most efficient one in the range of 0.2-1.0 THz remains the photoconducting (Auston) switch [Cai *et al.* 1998], which consists of a fast photoconductor bridging the gap in the transmission line structure. THz pulses can be also generated in the process of optical rectification in crystals [for example Zhang *et al.* 1990]. A ZnTe crystal excited by 800 nm optical pulses with duration of 100 fs, for example, emits mostly at 1 THz and higher. The choice of a particular source is directed by the application. In this study, the photoconducting dipole antennas are used in most of

the experiments for its relatively large emission power. Generation of THz pulses using antennas is discussed in detail in the next section.

### 2.3.2. Generation of THz pulses using Photoconducting Antennas

It is known that when a short optical pulse is incident on semiconductor in the presence of dc electric field, a far-infrared electromagnetic transient is emitted. There are two mechanisms known to account for generation of this radiation: the transient photocurrent radiation [for example Benicevicz *et al.* 1994], and optical rectification [Corchia *et al.* 2000]. The first mechanism is dominant when the electromagnetic pulse is generated in a biased photoconducting antenna, excited by a short optical pulse with the photon energy larger than the semiconductor bandgap.

A schematic diagram of a typical antenna structure is shown in Figure 2.2(a). The structure consists of two 10 $\mu$m wide metal lines deposited on a semiconductor surface, separated by 40-100 $\mu$m, and a dipole antenna with a photoconducting gap of 5-10 $\mu$m. A voltage of about 10V is applied across the two lines, creating a very strong electric field $E$ near the contacts. A schematic diagram of the response of the voltage-biased photoconducting antenna to a short optical pulse focused onto the gap between the two dipole arms is illustrated in Figure 2.2(b-e). The femtosecond laser pulses ($\tau_{FWHM}$ =100 fs) are focused to ~10 $\mu$m diameter spot on the dipole gap. The pulse generates electron-hole pairs in semiconductor at a rate proportional to the intensity function $I_{opt}(t)$ of the incident pulse (b). The current through the antenna rises rapidly due to the carrier injection and acceleration in the external bias field. The transient photocurrent radiates THz pulses into the free space (c).

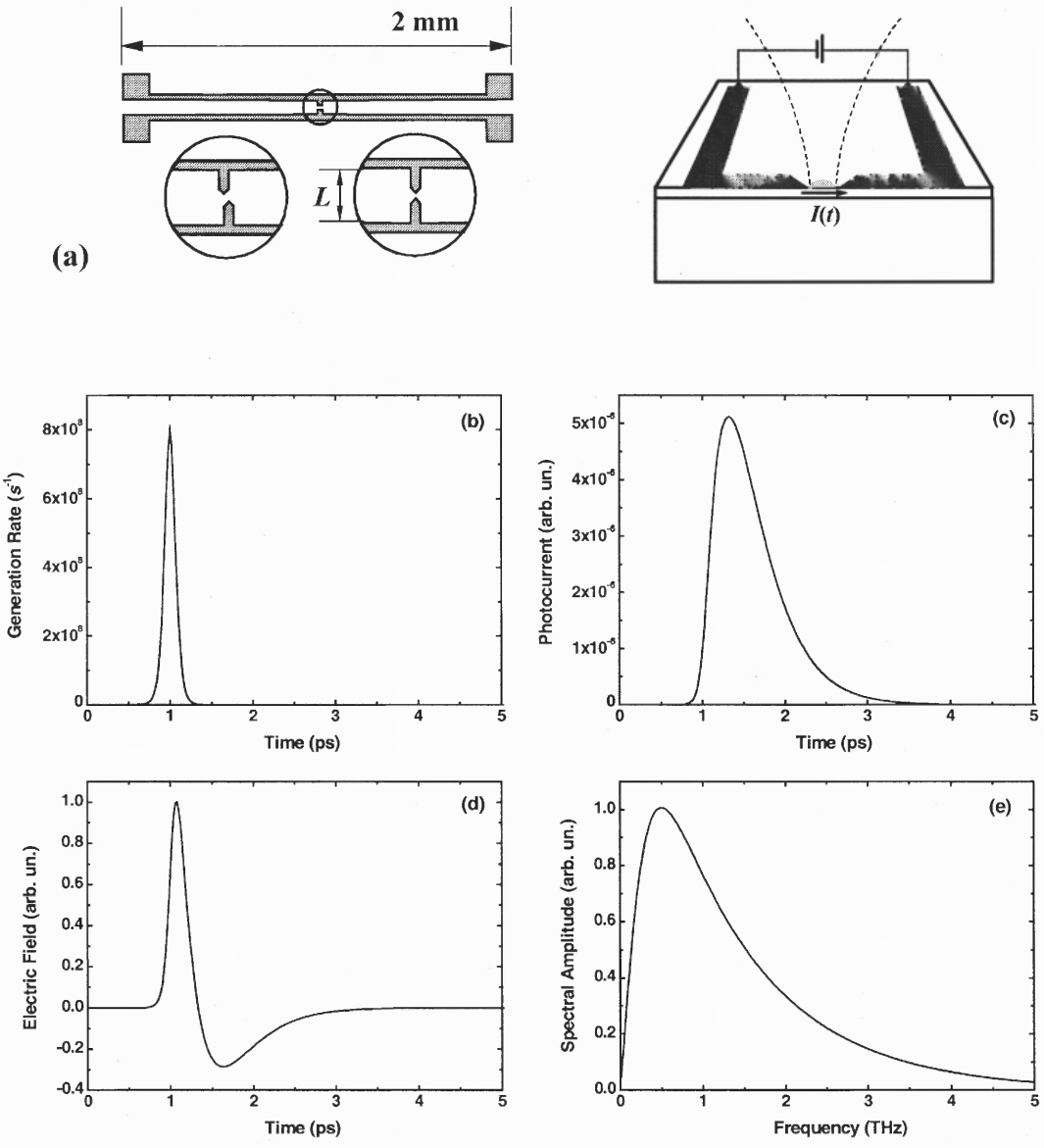


**Fig. 2.2.** The schematic diagram of the photoconducting antenna (a). Response of the biased antenna to the short optical pulse excitation (b-e). (b) The photocarrier generation rate follows the optical intensity function. (c) The photocurrent through the antenna. (d) The radiated electric field as the time derivative of the current transient and (e) its spectrum.

The current transient in a simple approximation of the ballistic motion of electrons can be expressed as follows

$$I(t) = \int_{-\infty}^{t} \frac{I_{opt}(t')}{\eta\omega} \exp\left(\frac{t-t'}{\tau_e}\right) \cdot \frac{e^2 E}{m}(t-t')dt' . \qquad (2.9)$$

The first term gives the number of carriers at the moment $t$, generated by the optical pulse at the moment $t'$. The second term gives the current due to the photocarriers accelerated in the external field in the ballistic approximation. The carrier recombination process and electron velocity saturation limit the transient current, which decays with a characteristic time given by the carrier lifetime $\tau_e$ in the semiconductor.

The radiated electric field can be derived from Maxwell's equations, where the sources of field are the charge $\rho$ and the current density $J$. The vector and scalar potentials are convenient to use. The electric and magnetic field vectors are expressed in terms of the potentials as follows [Jackson 1962]

$$\vec{B} = \nabla \vec{A}, \qquad (2.10)$$

$$\vec{E} = -\nabla\Phi - \frac{1}{c}\frac{\partial \vec{A}}{\partial t}. \qquad (2.11)$$

The dynamic behavior of the fields is determined by the two inhomogeneous Maxwell's equations

$$\nabla \times \vec{H} = \vec{J} + \frac{\partial \vec{D}}{\partial t}, \qquad (2.12)$$

$$\nabla \times \vec{E} + \frac{\partial \vec{B}}{\partial t} = 0. \qquad (2.13)$$

These equations expressed in terms of the potentials result in two in homogeneous wave equations if the Lorentz condition is satisfied

$$\nabla \cdot \vec{A} + \frac{\partial \Phi}{\partial t} = 0. \qquad (2.14)$$

The two uncoupled wave equations for the potentials:

$$\nabla^2 \vec{A} - \varepsilon\mu \frac{\partial^2 \vec{A}}{\partial t^2} = -\mu \vec{J}, \tag{2.15}$$

$$\nabla^2 \Phi - \varepsilon\mu \frac{\partial^2 \Phi}{\partial t^2} = -\frac{\varepsilon}{c}\rho. \tag{2.16}$$

The solution to the wave equation for the vector potential in the infinite space with current $\vec{J}$ as the only current source

$$\vec{A}(\vec{r},t) = \frac{1}{4\pi\varepsilon_0 c^2}\int d^3\vec{r}' \int \frac{\vec{J}(\vec{r}',t')}{|\vec{r}-\vec{r}'|}\delta(t'-t+\frac{|\vec{r}-\vec{r}'|}{c})dt'. \tag{2.17}$$

The Dirac $\delta$-function evaluates the surface current in the photoconductor at the retarded time. Integration is taken over the optically illuminated area. In the far field,

$$|\vec{r}-\vec{r}'| = r\left(1-\frac{\hat{r}\cdot\vec{r}'}{r}\right) \approx r, \tag{2.18}$$

and Eq. 2.17 for the vector potential on the axis perpendicular to the surface current plane reduces to a simple form

$$\vec{A}(z,t) \cong \frac{1}{4\pi\varepsilon_0 c^2}\frac{\vec{I}_s(t-\frac{z}{c})}{z}, \tag{2.19}$$

where $\vec{I}_s$ denotes the total surface current in the gap of the antenna.

The equation for the electric field vector [Eq. 2.11] implies that there are two contributions to the radiated field. One is due to the transient current and the other is due to created charge density. The latter depends on illumination condition and will not be discussed here. It must be mentioned, however, that the photogenerated carriers create a screening field, which reduce the applied external field and, therefore, the transient

current. Eq. 2.11 and Eq. 2.19 imply that the radiated electromagnetic field due to optical excitation of the biased photoconducting antenna is proportional to the first time derivative of the current

$$E(t) \propto \frac{\partial I(t)}{\partial t}. \tag{2.20}$$

The waveform of the radiated field, calculated according to Eq. 2.20 is shown in Figure 2.2 (d). The radiated electric field starts with arrival of the optical pulse. As the transient current saturates, electric field experiences a negative swing and decays slowly to zero. Figure 2.2(e) shows the spectrum obtained by applying the Fourier transform to the electric field function in Figure 2.2(d).

The time-domain waveform of the electromagnetic pulses depends on dynamics of the carriers as suggested by Eq. 2.20. Generation of THz radiation in semiconductors and the dynamics of the photoexcited electron-hole pairs have been discussed theoretically and experimentally by many researchers [for example, Son *et al.* 1994 and Benicewicz *et al.* 1994]. This interesting topic is out of the scope of the present work and we will mention only few aspects of the problem.

The photocurrent rise depends on the optical field envelope and acceleration in the external applied field. Motion of the carriers is determined by the band structure of the semiconductor, the momentum scattering rate, and the size of electric field. The band structure is important in GaAs, where velocity saturation can occur on a subpicosecond time scale due to intervalley transfer of the electrons into the low-mobility satellite valley. If the carriers are injected close to the satellite valleys, the acceleration time can increase to 2 ps, compared to 200 fs for carriers infected close to the band edge [Hu *et al.* 1995].

Because of the time derivative, the radiated field is dominated by the rising edge of the photocurrent transient, which is determined mostly by the optical pulse envelope and which is much faster than the decay. The tail of the photocurrent decays at the rate of the carrier recombination process, which in most semiconductors is large compared to 1 ps. In some materials with high defect density, carrier lifetime is <1ps, and the tail of the photocurrent also contributes to the radiated field [Fig. 2.2(d)].

Enhancement of THz radiation can be achieved by focusing the laser beam close to the electrode corners or fabricating sharp electrode ends. Electric field is stronger at the sharp features of the electrodes. In addition, band bending at the metal-semiconductor interface increases the potential slope [Cai *et al.* 1997].

The transient transport current is not the only source of THz radiation in biased semiconductors. It has been shown that the THz radiation can be generated by the displacement current [Planken *et al.* 1992]. In the presence of the field, electrons and holes are excited into states that are spatially displaced from each other. This process results in an "instantaneous" polarization of the electron-hole pairs, time derivative of which corresponds to a current. The temporal behavior of this transient is as fast as the optical pulse envelope function. In bulk semiconductors, the displacement component dominates for photoexcitation below the bandgap [Hu *et al.* 1994, Kuznetsov *et al.* 1996]. The mechanism may be also regarded as optical rectification through the nonlinear susceptibility $\chi^{(2)}$. A nonlinear dipole moment is also created by displacement of electrons optically excited into conduction band without any external or surface field [Khurgin 1994].

Besides the carrier dynamics, the actual dipole structure affects the radiated field. The dipole antenna narrows the spectrum around the resonance frequency. Provided that the transient current creates a broad spectrum of radiation, the central frequency of the radiated field can be tuned by varying the length of the dipole.

### 2.3.3 Generation of THz Pulses Using Nonlinear Crystals

THz radiation is also generated in large bandgap materials when a short optical pulse induces nonlinear polarization [Corchia *et al.* 2000]. The physical mechanism of this process is bulk optical rectification ($\chi^{(2)}$- difference frequency mixing (DFM)). Short laser pulses create a time varying dielectric polarization in a nonliner medium, which radiates electromagnetic transient.

$$E_i^{THz}(\omega) \propto \frac{\partial^2 P_i^{(2)}}{\partial t^2} = \frac{\partial^2}{\partial t^2} \sum_{j,k} \chi_{ijk}^{(2)}(\omega = \omega_1 - \omega_2; \omega_1; -\omega_2;) E_j^{vis}(\omega_1) E_k^{vis}(\omega_2), \qquad (2.21)$$

where $E^{viz}$ is the visible exciting field, $\omega_1$ and $\omega_2$ are the beat frequencies in the visible pulse and P is the induced polarization.

Most of the materials used to generate THz radiation (e.g. GaAs and ZnTe) have a zincblende structure, for which the only non-vanishing elements of $\chi^{(2)}$ are those without repeated indices, such as $\chi_{xyz}^{(2)}$ [Corchia *et al.* 2000]. The sum in Eq. 2.11 becomes

$$E_i^{THz}(\omega) \propto \frac{\partial^2 P_i^{(2)}}{\partial t^2} = \frac{\partial^2}{\partial t^2} \chi_{ijk}^{(2)}(\omega = \omega_1 - \omega_2; \omega_1; -\omega_2;) E_j^{vis}(\omega_1) E_k^{vis}(\omega_2). \qquad (2.22)$$

### 2.3.4 THz Detectors

THz transients are usually detected using electro-optic or photoconducting sampling technique. Both methods rely on changes of some property of the detecting element in the

presence of the incident THz pulse and a short optical pulse. A relative arrival time of the THz pulse and the gating optical pulse is varied and the THz field is sampled in time. In this section the principle of the photoconducting sampling is discuss in detail. A review of the electro-optic detection of terahertz radiation can be found in Gallot & Grischkowsky 1999. The performance comparison of the two methods was discussed by Cai *et al.* 1998.

### 2.3.5 Photoconducting Sampling

The electric field of the incident pulses is detected using another photoconducting antenna [Fig. 2.2(a)]. Electronics are not fast enough to measure the THz transients directly, and repetitive photoconducting sampling is used instead. In the off-state, when there is no photocarriers in the photoconducting gap, the antenna is highly resistive. The incident field induces a bias between the antenna electrodes. Injection of carriers by the laser pulses causes the resistance to drop substantially. Consequently, a photocurrent flows through the antenna when both the incident field and the carriers are present. If the photocarrier lifetime, $\tau_e$, is much shorter than the THz pulse, the photoconducting antenna acts as a sampling gate, which samples the THz field within a time $\tau_e$. During the photocarrier lifetime, a current proportional to the instantaneous electric field induced by the incident THz pulse in the gap flows in the detecting antenna.

The laser pulses, which trigger the transmitter and gate the detector, originate from the same source. Therefore, the phase relation between the generated THz pulse and the sampling pulse is controlled by position of the delay stage. By varying the time delay

of the gating pulse the entire THz transient is mapped without the need for fast electronics.

The bandwidth of the detector is determined by two factors, the photoconductor response to the optical excitation and the frequency-dependent response of the antenna structure. The photoconductor response imposes the high-frequency limit due to finite duration of the sampling intervals. In general, the photoconductor response is the convolution of the transient photoconductivity $\sigma(t)$ and the electric field across the photoconductor

$$I_{PC}(t) = \int \sigma(t - t')E(t')dt'. \qquad (2.23)$$

The electric field in the gap of the antenna is precisely sampled if the transient conductivity becomes the delta function. The finite duration sampling intervals in a real antenna, however, removes the high frequency oscillations from the measured signal $I_{PC}(t)$. Figure 2.3 illustrates the sampling process in the gap of the antenna. In order to resolve variations of the electric field at 1 THz, the photocurrent decay time must be less than ~0.5 ps.

The photogenerated electron-hole pairs do not necessarily have to recombine within 1 ps. One effective way to realize the fast decay of the photocurrent is to introduce defects with the fast carrier capture rate. The photoexcited carriers are quickly trapped by the defect states and then recombine with a slower characteristic time. Trapping of electrons can occur within a few hundred picoseconds, while recombination in semiconductors with low defect density is usually longer than hundreds of picoseconds. For example, the recombination time in bulk semi-insulating GaAs is ~300 ps. This time decreases substantially if defects are introduced. This is accomplished during the crystal

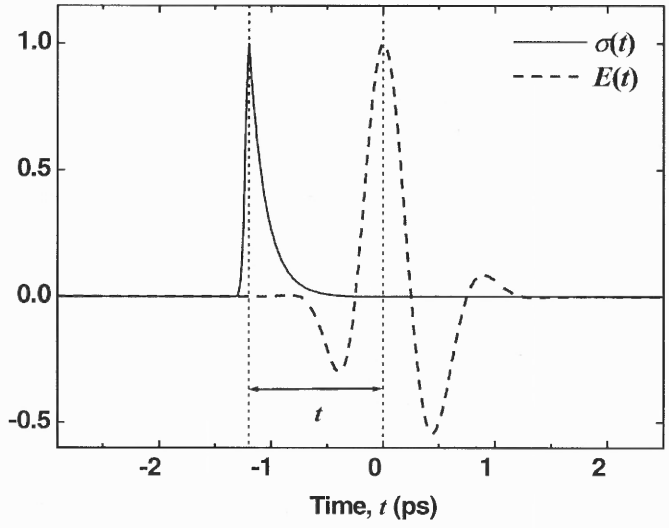


**Fig. 2.3.** Photoconducting sampling of the incident THz field. The THz pulse induced potential difference across the semiconductor $E(t)$, the gating optical pulse switched on the conductivity of the antenna for a short period of time. A current proportional to the convolution of the field and the photoconductivity flows in the antenna.

growth or afterwards by ion implantation. For example, annealed GaAs epitaxial films grown at low (below crystallization) temperatures have been shown to have carrier lifetimes as short as few hundred femtoseconds [Gupta *et al.* 1991]. Subpicosecond lifetime has been demonstrated in radiation-damaged silicon-on-sapphire, in which dislocations are formed by implanting argon, silicon, or oxygen ions [Doany *et al.* 1987].

The second factor that limits the bandwidth is the resonance properties of the dipole antenna. The electric field across the gap of the antenna differs from the THz pulse in free space due to the frequency dependent response of the antenna structure. As in the case of the antenna radiation, the length of the dipole determines the central frequency of the detector response In standard spectroscopic measurement, however, this effect is eliminated when the spectrum of the sample is normalized to the reference spectrum, measured with the same frequency response.

## 2.4 THz-TDS System

In the previous sections, the principle of THz –TDS technique, the THz pulse sources and detectors were discussed. In this section, the rest of the system components, including a femtosecond laser, THz optics, and electronics are discribed. A schematic diagram of a typical THz-TDS system is shown in Figure 2.4. It consists of a femtosecond laser source, a variable time delay line, the THz pulse transmitter, collimating and focusing optics, the sample, the optically gated THz detector, a current amplifier, and a lock-in amplifier. The measurements are automated by means of the computer control of the delay line and the lock-in amplifier.

### 2.4.1 Experimental Setup

A solid-state mode-locked Ti:Sapphire laser (*Tsunami* by Spectra-Physics, Inc., *Lexel 480* by Lexel Lasers, Inc.) pumped with Ar-ion laser (*Innova 400* by Coherent, Inc.) produces short $\tau_{FWHM}$~100 fs pulses (measured by autocorrelation technique). The central

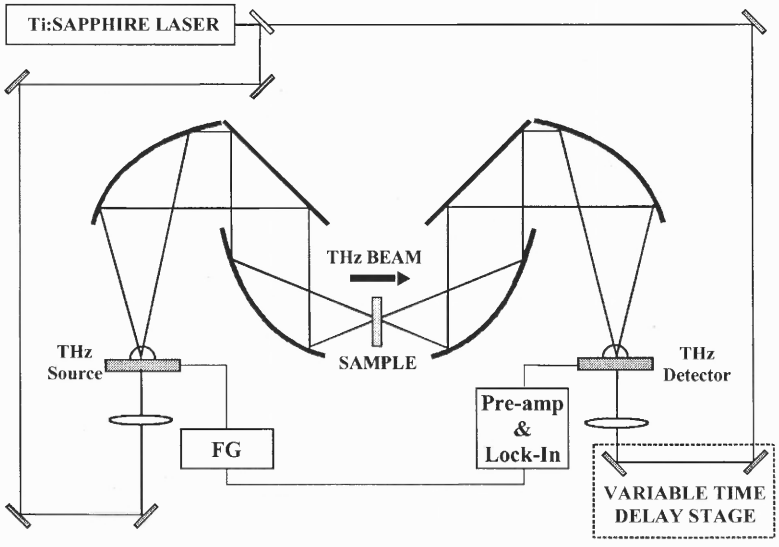


**Fig. 2.4.** The schematic diagram of THz-TDS system.

wavelength is near 800 nm and the repetition rate is 100 MHz. The beam is divided in two by means of a half-wave plate and a polarizing cube beamsplitter (not shown in the diagram). One part of the beam is focused onto the gap of the biased dipole antenna using a 20X microscope objective. The second part passing through the variable time delay stage is focused on the detecting antenna with a similar microscope objective. Generated THz radiation is collected using hyperhemispherical Si lens attached to the emitter and an off-axis parabolic mirror. The collimated beam is then focused on a sample using another parabolic mirror. After passing through the sample the THz pulses are focused on the detecting antenna using parabolic mirrors and a Si lens.

The THz photoconducting transmitter and detector require moderate laser power (<30 mW each). The transmitter bias is modulated using a square shape function generator (FG) at a frequency of 12 kHz, which results in the highest signal-to-noise ratio. The dc photocurrent in the detector at the modulation frequency is transferred into a voltage signal using the current pre-amplifier. This signal is eventually measured using the lock-in amplifier. When a ZnTe crystal used instead of the biased antenna for generation of the THz pulses, the optical beam in front of the crystal is mechanically chopped to modulate the signal. Due to a limit on maximum chopping frequency the signal is measured in this case at ~2 kHz.

### 2.4.2 Characteristics of THz Pulses.

A typical THz waveform measured in the described setup is shown in Figure 2.5(a). The source is a LT GaAs antenna with a 10 $\mu$m gap and a 60 $\mu$m long dipole biased at 0.5 V. The detector is a similar antenna with a 45 $\mu$m long dipole. Both structures are excited

with 4 mW (average power) optical pulses. The THz transient exhibits a little more than one cycle and its spectrum peaks at 0.7 THz.

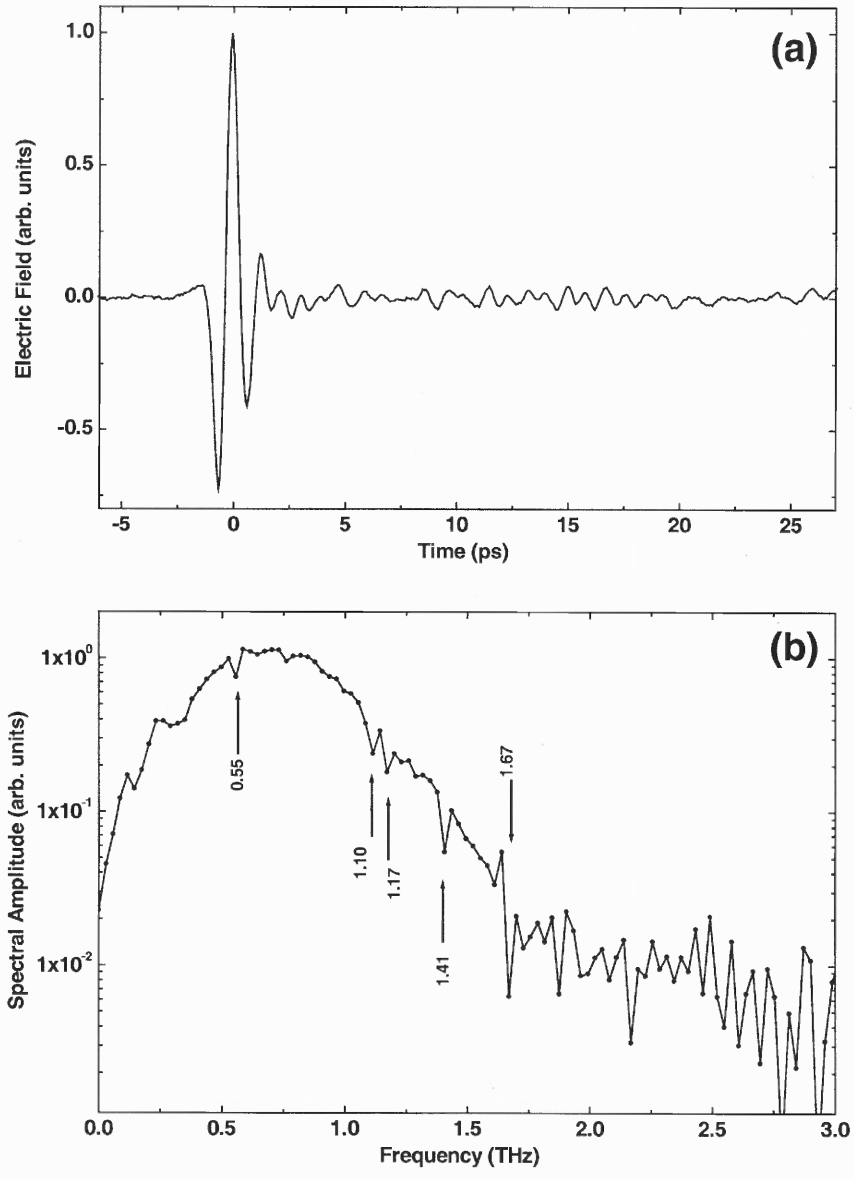


**Fig. 2.5.** The THz pulse waveform measured using THz-TDS system (a). The pulse is generated by a biased (0.5 V) photoconducting antenna based on LT GaAs. The antenna is excited with short optical pulses (average power 4 mW). The detecting antenna is gated with optical pulses of the same power. The Fourier spectrum of the pulse (b).

THz pulses generated by the frequency conversion process in a <110> oriented ZnTe crystal contain spectral components of considerably higher frequency. The

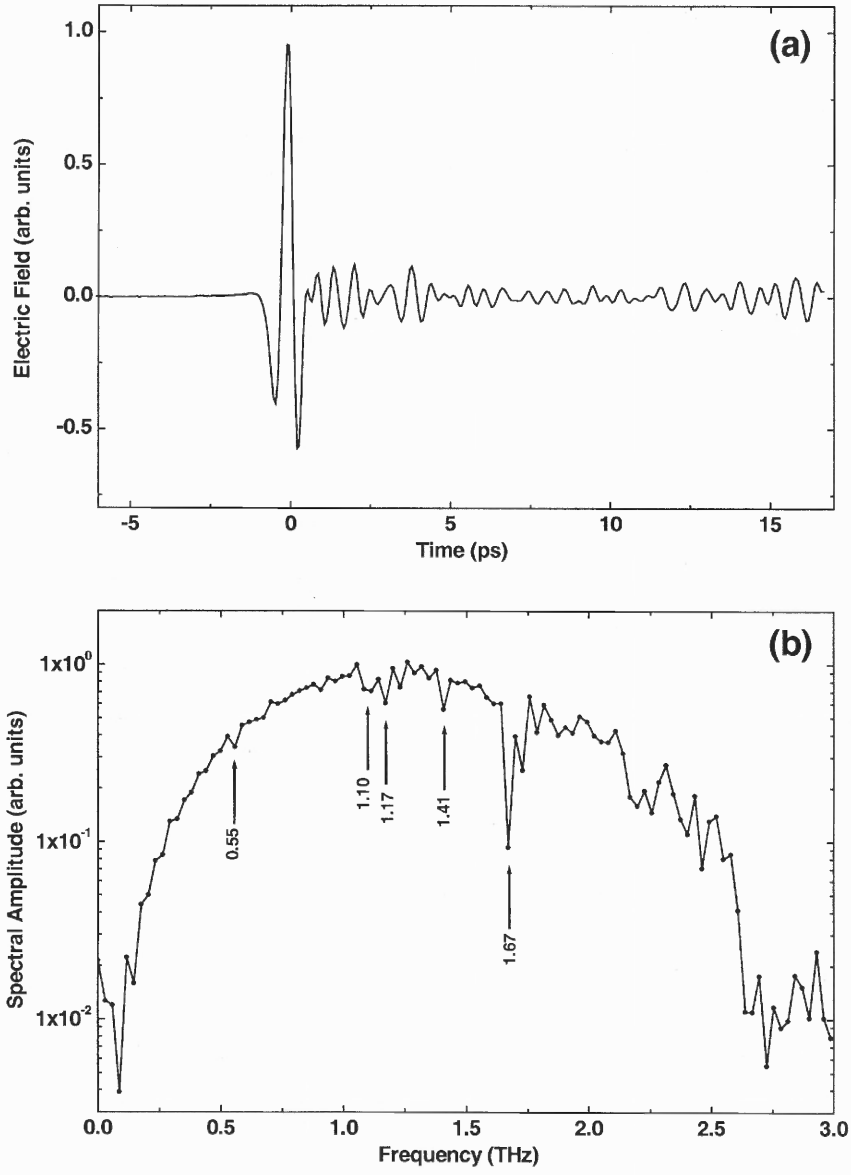


**Fig. 2.6.** The THz pulse waveform measured using THz-TDS system (a). The pulse is generated by the frequency conversion process in ZnTe crystal (<110>) illuminated by the short optical pulses (average power 50 mW). The detecting antenna is gated with 12 mW optical pulses. The Fourier spectrum of the pulse (b).

measured spectrum extends to ~2 THz.

The waveforms shown in Figure 2.5(a) and Figure 2.6(a) contain long lasting electric field oscillations after the pulse. This effect is related to absorption of particular spectral components by water molecules which are present in air. The THz pulse travels ~80 cm through the air. The spectra show distinctive absorption lines at 0.55, 1.10, 1.17, 1.41, 1.67 THz. Frequencies of the absorption lines coincide with the strongest absorption lines of the water vapor spectrum measured by Cheville & Grischkowsky 1999. At higher frequencies (1.7-3.0 THz), density of absorption lines of water increases and individual lines are not resolved.

The poor spectral resolution in Figure 2.5(b) and Figure 2.6(b) is due to a narrow time window. Since the waveform is truncated after ~30 ps, the spectral resolution is only 0.03 THz. The water absorption lines at normal pressure and temperature are significantly narrower and the induced oscillations last much longer than 30 ps. In order to increase the spectral resolution, a wider time window have to be used. Figure 2.7(a) demonstrates the spectrum obtained using a 150 ps long waveform, which provides the spectral resolution of 6.7 GHz. This window was also expanded by padding the interval from 150 ps to 300 ps with zeros. This operation corresponds to interpolation in the frequency domain. The absorption lines, barely distinguishable in Figure 2.5(b) and Figure 2.6(b), clearly appear in the spectrum of Figure 2.7(a) (the path in air is 55 cm).

Water absorption decreases if the system is purged with dry nitrogen gas. A part of the system, which includes the sample and the THz transducers, is enclosed into a vapor-tight box. Nitrogen flow reduces concentration of water molecules in air, making it less absorptive in the THz range. The waveforms measured in the purged system show

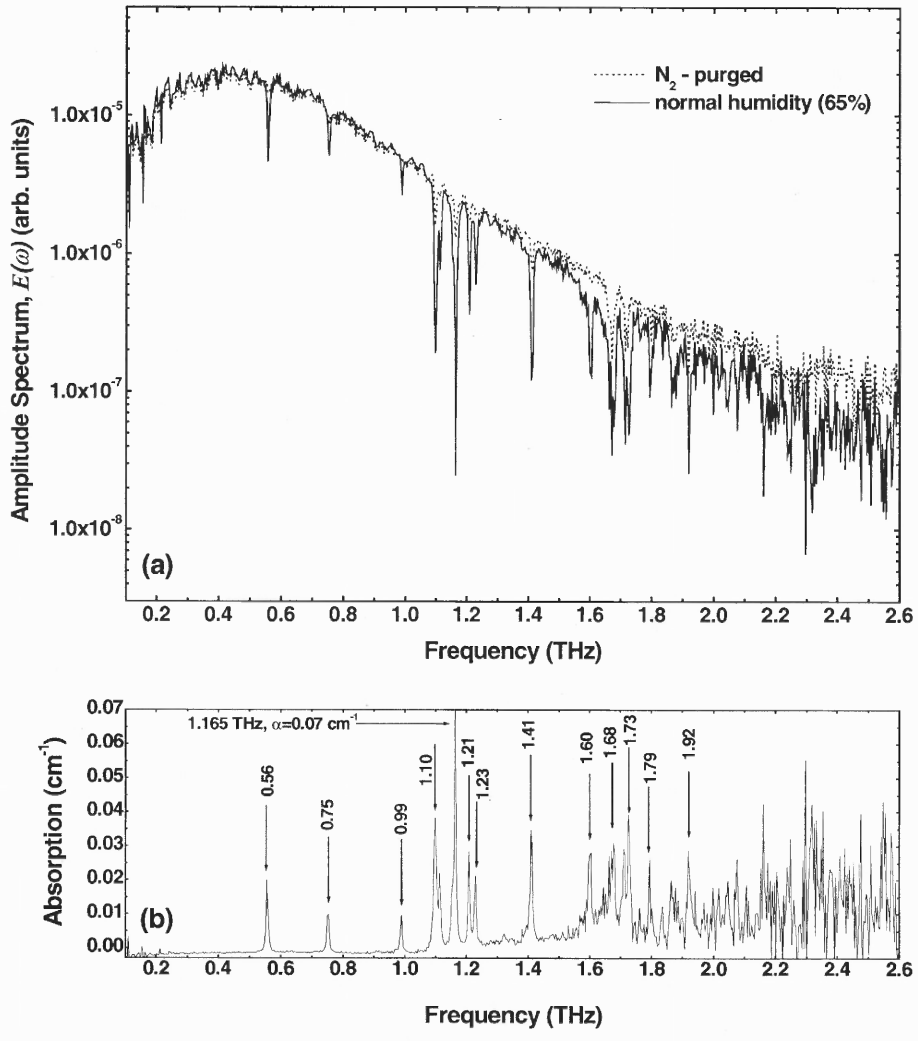


**Fig. 2.7.** The Fourier spectrum of the THz pulse waveform measured using THz-TDS system with (dotted curve) and without nitrogen purging (solid curve) (a). Estimation of the absorption coefficient of air $\alpha = -\frac{1}{L}\ln\left(\frac{E(\omega)}{E_0(\omega)}\right)$, where $L$=55 cm denotes the length of the pulse path in air (b).

significantly smaller oscillations after the pulse, and the absorption lines in the spectrum reduce. Using the measurements with and without purging, the absorption coefficient of air can be estimated by taking the logarithm of the spectral ratio $E(\omega)/E_0(\omega)$. The result is shown in Figure 2.7(b). Note that $N_2$-purging only reduces water absorption. Some lines

are still present in the spectrum [dotted curve in Fig. 2.7(b)], and the actual absorption of electromagnetic waves in air is larger.

The present work is focused on near-field imaging applications of THz-TDS. However, there are many other applications. In the high-speed device and wide-bandwidth communication field, THz-TDS is used as a characterization tool that allows studying propagation of picosecond and sub-picosecond pulses. A recent review paper by Grischkowsky 2000 discussed advances in that field. THz-TDS has been applied to studies of conformational changes in biomolecules, such as DNA and proteins, which are traditionally studied with Raman and FTIR. These large molecules have low-frequency collective vibrational modes, therefore changes in the absorption spectrum of the molecules reflect the conformational motion [Markelz *et al.* 2000]. Generation of THz pulses itself provides a unique possibility to study dynamics of carriers in semiconductors (Son *et al.* 1994). Imaging applications of THz-TDS, which will be mentioned in the next chapter, draw considerable attention of researchers as well.

# CHAPTER 3

# IMAGING WITH TERAHERTZ WAVES

## 3.1 Introduction

Imaging technology has progressed rapidly into the THz region of the electromagnetic spectrum during the last few years [Mittelman *et al.* 1999]. This advance is mostly due to development of the THz time-domain (or THz time-resolved) spectroscopy (THz-TDS) technique. This method covers a wide spectral window from 0.1 THz to 40 THz, which is rich in electromagnetic phenomena. The THz-TDS system has a small power in the THz beam, but exceptional sensitivity. This combination makes the THz-TDS technique a powerful tool for far-infrared imaging with a variety of potential applications.

Most chemical compounds show specific frequency dependent absorption and dispersion in the THz range. In principle, THz-TDS technique can be applied to determine the chemical content of an unknown object. Diffraction optics allows spatial resolution on the order of the wavelength. The first imaging system was demonstrated by Hu and Nuss (1995). THz pulses were focused to a diffraction-limited spot on the sample, and the transmitted THz waveforms are acquired at each point of the sample scanned in the focal plane. Figure 1 shows the first images in THz waves: a packaged semiconductor integrated circuit, and water concentration in a fresh tree leaf. Further development of the THz imaging went in two main directions: reduction of the acquisition time for each THz waveform and developing digital processing algorithms, and improvement of spatial resolution. A review of the recent advances could be found in the paper by Mittelman *et al.* (1999).

The major limitation of THz, or T-ray, imaging is poor spatial resolution (~1-2 mm) due to the long wavelength, which does not allow resolving small object features with conventional optical methods. The resolution can be significantly improved by implementing the concept of near-field scanning optical microscopy [Pohl 1991]. Subwavelength resolution is achieved if the source of radiation is spatially confined to a

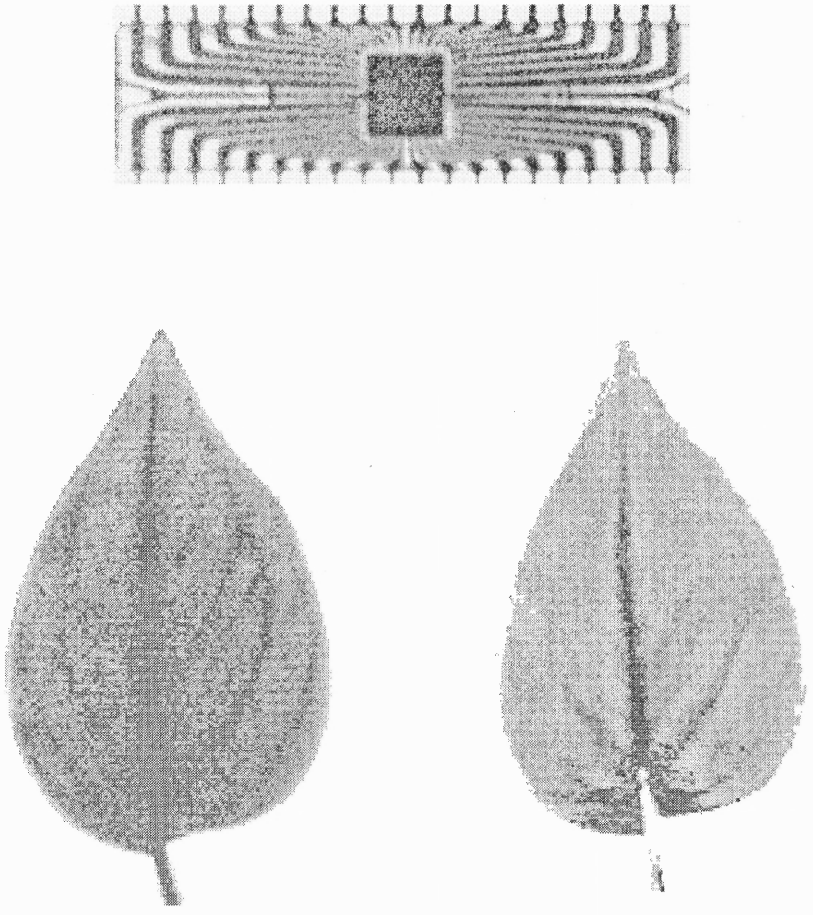

**Fig. 3.1.** THz image of a packaged semiconductor integrated circuit (plastic packaging) (a). THz image of a fresh tree leaf (b). Attenuation of THz radiation through the leaf is largely due to water within the leaf (left image). Another image shows the same leaf after 48 h. Water has evaporated from the leaf except from the stems, where transmission remains small. Reference: Hu and Nuss (1995)

size smaller than the wavelength and it is placed close to the object, so that it only locally illuminates the object. The transmitted waves carry information about the point of the object, where the source is placed. By scanning the object over the source one constructs a near-field image. Most of the near-field imaging setups use a small illuminated aperture as a subwavelength source. Spatial resolution in this case is defined by the aperture size and is not limited by diffraction [Pohl 1991]. Near-field scanning optical microscopy (NSOM) developed very quickly over the past two decades. Various modifications of the original system were proposed and demonstrated [Betzig *et al.* 1987, Reddick *et al.* 1989, Knoll & Keilmann 2000].

Several imaging systems based on the THz-TDS setup and near-field approach have been introduced, pushing the resolution limit to a few tens of microns. Hunsche *et al.* (1998) demonstrated $\lambda/4$ resolution by focusing the THz beam into a tapered metallic tip with a small (50-100 $\mu$m) exit aperture and scanning the sample in the near-zone of the aperture. Brener *et al.* (1998) showed similar improvement with the aperture placed close to the THz source for better radiation coupling. Another approach uses the fact that the THz emission point is itself much smaller than the THz wavelength. By placing the sample close to the point of THz generation, one can use spatial confinement of the generation process for subwavelength resolution imaging [Wynne & Jaroszynski 1999].

An alternative solution, developed by Q. Chen *et al.* (2000) and named as a dynamic aperture approach, potentially can improve resolution to a few microns. In this system, a focused optical beam creates a local electron-hole plasma in the sample, which absorbs the THz beam in a ~10-20 $\mu$m diameter region. By measuring THz transmission and scanning this optical beam, the response of the sample can be mapped. However,

application of this method is limited to semiconductor surfaces and images are related to the concentration of photogenerated carriers.

In this work, a THz imaging system based on the aperture-type near-field probe is described. The method provides a very high spatial resolution and has all the advantages of the THz-TDS. The technique can be used in two modes, illumination and collection, with spatial resolution of few microns independent of the wavelength of the radiation (120-1500 $\mu$m). The combination of the near field microscopy concept with the THz-TDS allows for studying the temporal evolution of the electromagnetic field in the near field of objects. The broadband coherent THz source potentially provides the possibility of spectroscopy on a micrometer scale. The principle of the THz near-field imaging system is discussed in this chapter.

## 3.2 NEAR-FIELD IMAGING

### 3.2.1 The Principle of Near-Field Imaging.

Subwavelength spatial resolution in the near-field zone can be realized in various configurations. The collection mode in transmission will be considered in this section primarily because most of the experiments discussed in the present work were performed in this arrangement.

Consider a flat object illuminated by a monochromatic wave [Fig. 3.2]. The electric field in the plane of the object can be expressed as a superposition of field with spatial frequencies $k_x$ and $k_y$

$$E(x,y,z)=\frac{1}{4\pi^2}\iint A(k_x,k_y,z)e^{i(k_x x+k_y y)}dk_x dk_y\,, \qquad (3.1)$$

where the spectral amplitudes are related to the field distribution in the plane by the Fourier integrals

$$A(k_x,k_y,z)=\iint E(x,y,z)e^{-i(k_x x+k_y y)}dxdy \ . \tag{3.2}$$

Given that the total wave vector is $k$, and the spectral amplitudes satisfy the propagation relation, the optical electric field in arbitrary point is described in terms of the field in the object plane $z$=0 and the exponent, which constitutes the $z$-dependence

$$E(x,y,z)=\frac{1}{4\pi^2}\iint A(k_x,k_y,z=0)e^{i(k^2-k_x{}^2-k_y{}^2)z}e^{i(k_x x+k_y y)}dk_x dk_y \ . \tag{3.3}$$

If the object field has spatial frequency components $k_x$ and $k_y$ such that

$$\sqrt{(k_x{}^2+k_y{}^2)}>\frac{2\pi}{\lambda} \ , \tag{3.4}$$

the corresponding spectral amplitudes $A(k_x, k_y, z)$ are evanescent decreasing exponentially with increasing $z$. These spatial frequencies can not propagate into the far-field rigeon ($z>>\lambda$) and, therefore, conventional imaging techniques are unable to reproduce subwavelength features in the image.

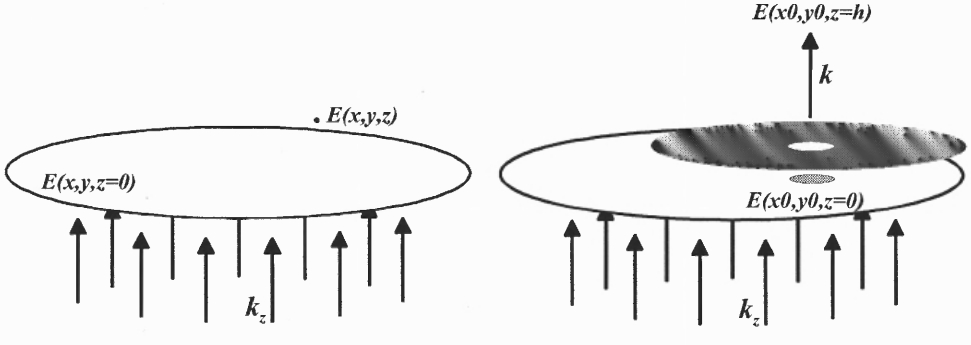


**Fig. 3.2.** The schematic diagram of the collection mode near-field imaging using a subwavelength aperture.

However, the high spatial frequency components can be sampled by a small aperture (or any small scattering object) introduced in the evanescent field zone as schematically shown in Figure 3.2. A fraction of the incident wave transmits through the aperture to a detector. Since the field that passes through the aperture is determined by the object field at the point of the aperture entrance, the object field can be sampled by the aperture. If the aperture is placed close enough to the object, so that the evanescent components of the object field are strong, the subwavelength resolution imaging can be realized. An image of the object can be constructed by scanning the aperture over the object and detecting the amplitude of the transmitted wave.

The amplitude of the wave that emerges from the aperture is related to the electric field *E(x,y,z)* averaged over the aperture area. In general, the field transmitted through the aperture can be expressed as some average of the field in the object plane multiplied by a transfer function of the aperture, which depends on the distance to the object *h*, the aperture size *d*, and the wavelength.

$$E_T(x,y) = T(h,d,\lambda)\cdot \overline{E}(x,y) \tag{3.5}$$

The near-field zone of the object can be defined as a region, where the amplitude of the high spatial frequency evanescent components of the object field is large. For a transverse vector $k_t$, which satisfies the condition in Eq. 3.4, the amplitude decreased exponentially in the z-direction with a characteristic length

$$\delta = \frac{1}{\sqrt{k_t^{\,2} - \left(\frac{2\pi}{\lambda}\right)^2}} \tag{3.6}$$

An aperture of size $d$ is capable of sampling spatial frequencies with a transverse vector $k_t$ smaller than $\pi/d$. The characteristic decay length of the field with $k_t = \pi/d$ in the limit that the aperture size is much smaller than the wavelength is $\delta=d/\pi$. The decay length is larger for the field with a smaller $k_t$. Therefore, by sampling spatial frequencies with the transverse wavevector $k_t$ up to $\pi/d$, the aperture-size resolution can be achieved. The separation between the aperture and the object has to satisfy inequality

$$h < \frac{d}{\pi}, \tag{3.7}$$

so that the spatial frequencies $k_t < \pi / d$ have non-vanishing amplitudes at the distance from the sample $h$, where the aperture is placed.

It is worth stressing two important properties of the near-field imaging: (1) spatial resolution does not depend on the wavelength, and (2) the technique is characterized by a very shallow depth of field. The first one is particularly important for imaging with THz pulses, which contain a broad band of wavelengths. Imaging can be implemented with the same spatial resolution for the whole spectrum of the THz pulse. This property also opens the possibility for the high spatial resolution spectroscopy with THz pulses. The second characteristic limits application of the technique only to thin samples.

It must be mentioned that any external object, introduced in the near-field zone of the object under investigation, perturbes the field distribution and results in artifacts. In a conventional NSOM setup, the aperture fabricated on the tip of a fiber. In our near-field probe, the aperture is realized in a plane metallic screen. The presence of the conducting plane in the vicinity of the object affects the field distribution. However, the plane is

uniform and its interaction with the object does not limits the resolution capability of the method.

### 3.2.2 Subwavelength Aperture Transmission

When an electromagnetic wave is incident of a metallic screen with a subwavelength aperture in it, most of the power is reflected back from the screen. Only a small fraction passes to the other side of the screen. Because of the weak coupling, the near-field technique suffers a substantial reduction of the signal amplitude, which in many cases limits the spatial resolution.

Power losses can be estimated in the transmission experiment when an aperture is placed in the focal point of a freely propagating THz beam. A schematic diagram of the

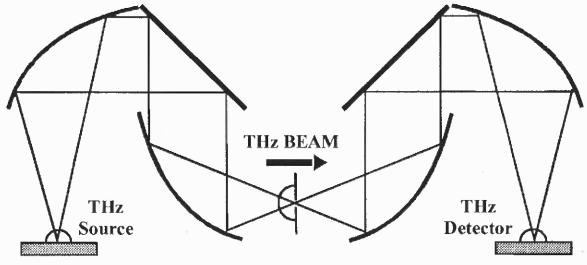


**Fig. 3.3.** The shematic diagram of the experimental setup for the aperture transmission studies.

experimental setup is shown in the Figure 3.3. Single-cycle electromagnetic pulses with the center frequency of 0.8 THz are generated using photoconducting dipole antenna. The radiation is focused on the aperture cut in a 25 $\mu$m thick stainless steel screen. A hyperhemispherical Si lens is attached to the aperture screen at the entrance side for efficient radiation coupling. The lens has a high value of numerical aperture and the beam

can be focused at the backside of the lens to a small size. Radiation, transmitted through the aperture radiation, is collected with a parabolic mirror (N.A.=0.4) and guided to the photoconducting antenna detector.

The THz beam transmitted through a 500 $\mu$m-diameter aperture suffers almost no attenuation. Absence of losses shows that the high refractive index hyperhemispherical lens ($n$=3.6) focuses the beam to the size smaller than 500 $\mu$m. The beam waist before the lens is estimated to be ~1.6 mm (full width half maximum of the electric field amplitude). Attenuation increases as the aperture diameter decreases. Figure 3.4 shows waveforms of the THz pulse transmitted through apertures with diameter $d$=50 - 500$\mu$m.

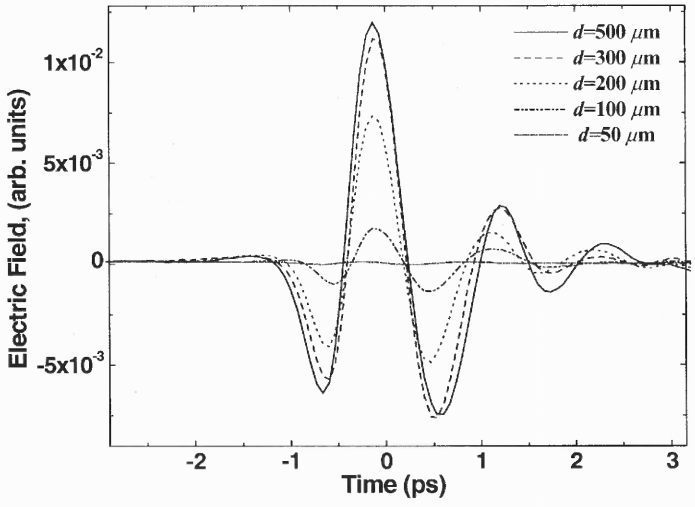


**Fig. 3.4.** THz pulse transmitted through apertures in a 25 $\mu$m thick stainless steel foil.

The peak amplitude of the pulse transmitted through the 50 $\mu$m aperture is ~150 times smaller than that of the pulse transmitted through the 500 $\mu$m aperture. Different spectral components transmit through the aperture with different efficiency. Fourier

transform of the waveforms shows that the longer wavelengths are suppressed more than the shorter ones. Figure 3.5 presents the spectra of the transmitted pulses.

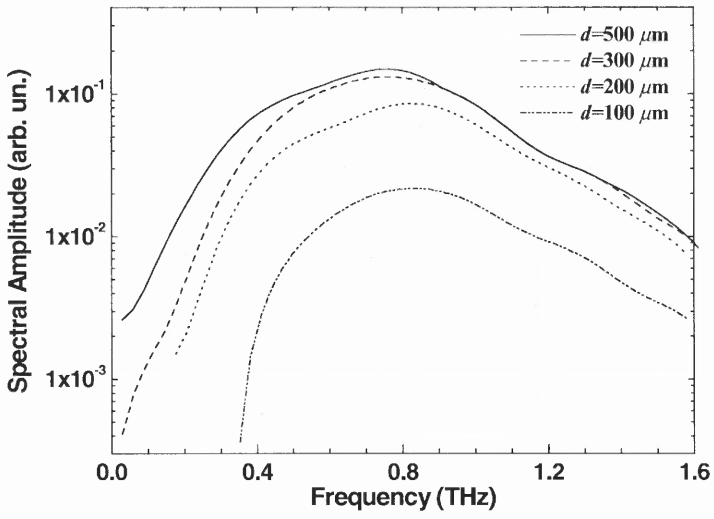


**Fig. 3.5.** The spectra of the THz pulses transmitted through apertures of different sizes.

Further reduction of the aperture size decreases the amplitude of the transmitted waves even more. In the limit that the aperture size $d$ is much smaller than the wavelength, the amplitude of the transmitted wave decreases as the $d^3$ law [Bethe 1944]. We can expect that the THz pulse would suffer ~$10^{-5}$–$10^{-6}$ attenuation in amplitude after transmission through a 5 $\mu$m aperture ($\lambda$/100). Note that the corresponding intensity of the pulse reduces by the factor of $10^{-10}$-$10^{-12}$.

### 3.2.3 Near-Field Detection of the Field Coupled through the Aperture

It is obvious that very small apertures are not practical in the approach described in the previous section. However, efficient detection of the field that couples through the aperture can be realized if the field is measured in the near-zone of the aperture. In this

case, the imaging setup has to be in the collection mode, when the object is uniformly illuminated and the aperture is located behind it.

Electromagnetic energy of the field behind an illuminated subwavelength aperture is mostly concentrated in the near-field zone and does not propagate away from the aperture [Leviatan 1986]. The field density decreases with the distance from the aperture at a close to an exponential rate. The non-radiating field, also regarded as the evanescent field, is not detected in the setup previously described. The contribution of the evanescent components to the total field in the near zone is substantially larger than that of the

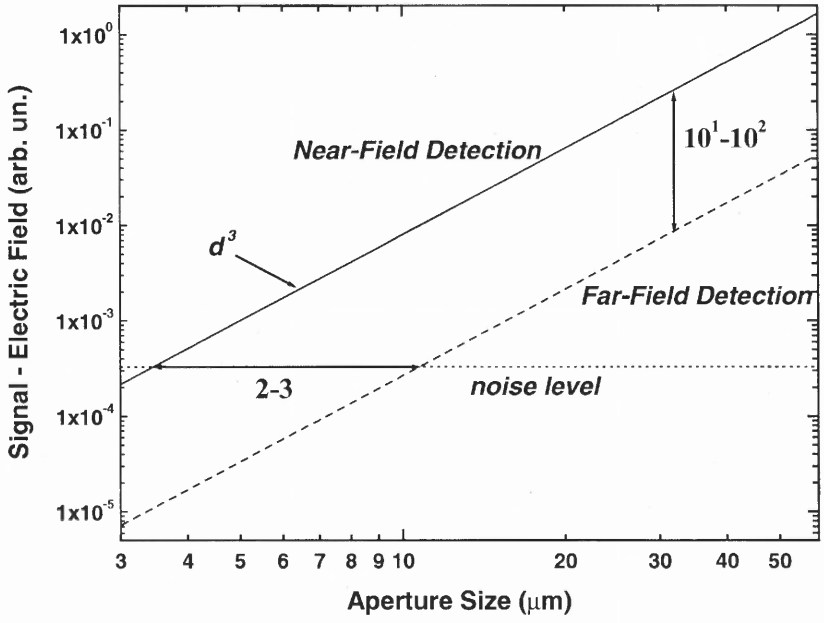


**Fig. 3.6.** The schematic illustration of the advantage of the near-zone detection of the coupled through the aperture field.

radiating component. Therefore, the imaging probe can benefit from moving the detecting element into the near zone of the aperture. Figure 3.6 schematically demonstrates the advantage of the near-field detection. For every order of the sensitivity improvement, the

aperture can be reduced by a factor of two without degradation of the signal-to-noise ratio.

## 3.3 High Spatial Resolution THz Imaging System

In order to realize the idea of detecting the coupled through the aperture field in the near-zone of the aperture, an integrated near-field probe that combines the subwavelength aperture and the detecting element was developed. Sensitivity of the technique improves by approximately two orders of magnitude compared to the far-field detection. Using the integrated near-field probe, THz pulses transmitted through apertures as small as $\lambda/300$ (for the spectral component with the largest wavelength) were detected. The probe with 5 $\mu$m aperture demonstrated spatial resolution of 7 $\mu$m with a practical signal-to-noise ratio (~30). In the following sections the integrated near-field probe and the setup of the imaging system is described.

### 3.3.1 Integrated Near-Field Probe

The probe is designed to measure locally the electric field of the THz pulse transmitted through an object. To improve the sensitivity, the probe detects the evanescent modes of the THz field that exist in the near zone behind the aperture of the probe. As the distance from the aperture increases, the evanescent field decay rapidly, but it is relatively high in the close proximity of the aperture. The probe integrates a subwavelength aperture and a photoconducting antenna so that the antenna dipole is located in the near-field zone of the aperture.

A schematic diagram of the near-field detector is presented in Figure 3.7. An entrance subwavelength aperture is lithographically defined on a surface of the probe in a gold film evaporated on a thin GaAs layer. A GaAs protrusion through the aperture enhances the field coupling into the probe. The photoconducting dipole antenna is

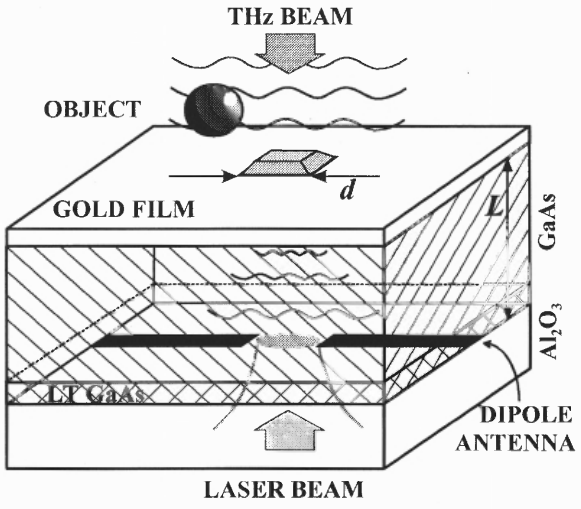


**Fig. 3.7.** The schematic diagram of the collection mode integrated near-field probe.

embedded between a thin layer of GaAs and a sapphire substrate. The antenna is fabricated on a 1 $\mu$m thick low temperature grown GaAs epilayer. The sapphire substrate supports the structure and allows the optical gating pulses access to the antenna from the substrate side. The GaAs layer is removed on the side of the probe for access to the antenna contacts.

### 3.3.2 Experimental Setup

The integrated near-field probe is placed in detector site of the THz-TDS setup. The electric field measurements are conducted in the same manner as in the regular THz-TDS

method, except for a location of the sample, which in the near-field measurements is placed a few microns away from the probe. An additional element of the setup is a translation stage, which scans the object in front of the probe. A schematic diagram of the collection mode imaging setup is shown in Figure 3.8(a).

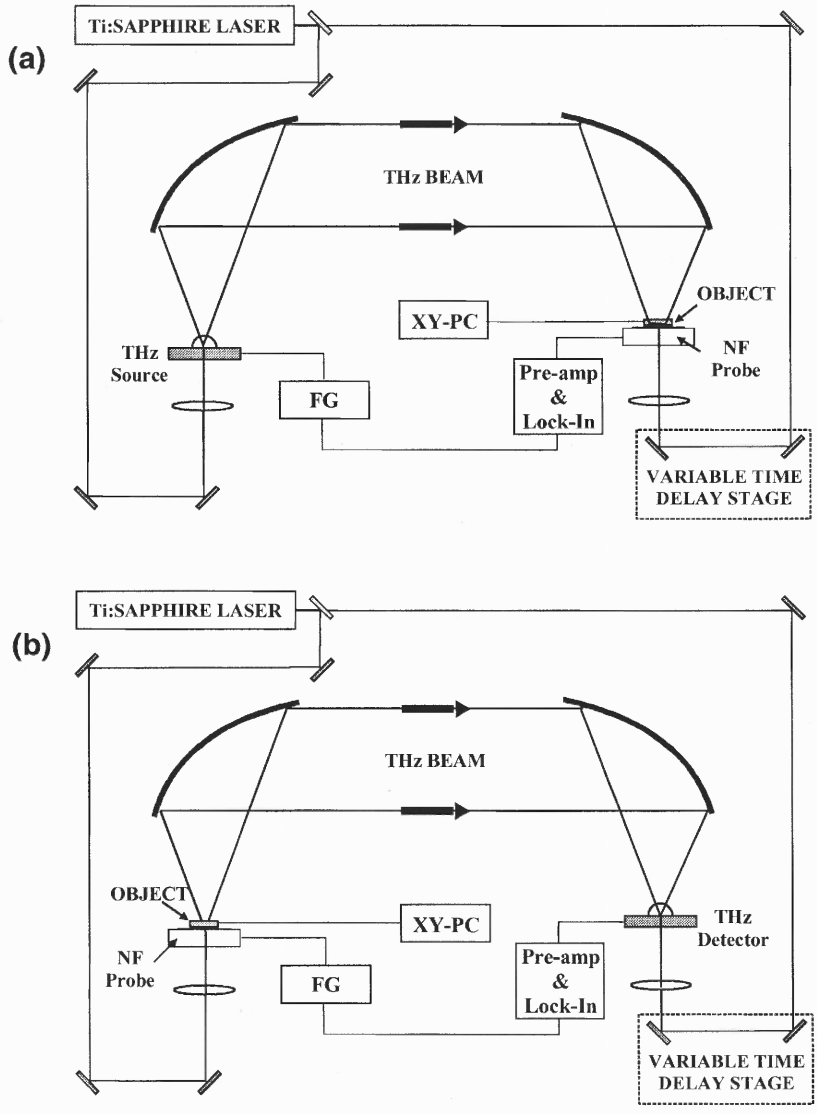


**Fig. 3.8.** The schematic diagrams of the near-field imaging system based on the integrated probe in the collection (a) and illumination modes (b).

The same design of the probe can be also used in illumination mode. In this case, the antenna of the probe is used as the THz emitter. When the emitter is located less than a wavelength way from the aperture, coupling of the radiation out the probe is more efficient than in the conventional setup [Fig. 3.3]. However, experimental estimation of losses shows that sensitivity of the collection mode setup is higher than that of the illumination mode setup by approximately a factor of two.

# CHAPTER 4

# NEAR-FIELD PROBE DESIGN AND FABRICATION

## 4.1 Introduction

High sensitivity of the collection mode near-field probe is achieved because the electric field is measured immediately behind the probe aperture before the transmitted radiation diverges and the electric field amplitude drops. Design is absolutely crucial, because the probe performance depends on its sensitivity, which is directly determined by geometrical parameters. Sensitivity of the probe strongly depends on the separation between the aperture and the detecting element. The coupling of radiation through the aperture depends on the geometry of the dielectric tip protruding through the aperture. Two issues are mainly discussed in the first part on this chapter: how the amplitude of the electromagnetic field decreases with distance form the aperture, and how the probe geometry affects field coupling into the aperture. Effects of the aperture size will be considered separately in Chapter 5.

Geometry effects are usually difficult to study experimentally. Numerical simulation techniques are of a great value if they predict the effects without time consuming fabrication and testing. Numerical modeling of the THz pulse coupling into the aperture of the probe is presented in this chapter. The modeling uses the finite-difference time-domain method and takes into account the probe geometry and the pulsed nature of the radiation.

The last part of the chapter describes the fabrication process, which includes the photoconducting antenna and the integrated probe fabrication.

## 4.2 THz Pulse Propagation inside the Near-Field Probe

### 4.2.1 Overview of the Wave Propagation through a Subwavelength aperture

The problem of diffraction of electromagnetic waves by a small aperture in a conducting screen directly applies to aperture-type near-field microscopy. The main practical aspect of the problem is the calculation of the amount and the spatial distribution of the transmitted radiation. For the collection mode near-field probe, which integrates a subwavelength aperture and a detecting element, this problem directly corresponds to the sensitivity issue.

The propagation of electromagnetic waves through a subwavelength aperture in a metallic screen has been studied by many authors [Bethe 1944; Bouwkamp 1950, Leviatan 1986; Novotny 1994; Roberts 1989]. The standard analytical Kirchhoff's method for solution of diffraction problems is inadequate for the treatment of the subwavelength apertures. This method does not satisfy the boundary conditions in the plane of the aperture. The formulation of the problem is more appropriate to the case of the aperture in a perfectly absorbing screen. As result, Kirchhoff's method leads to an incorrect solution.

The classical analytical solution for a circular aperture was derived by Bethe (1944). The solution is based on an analytical form of the electromagnetic fields in the plane of the illuminated aperture. This form was obtained only for the elliptical apertures, however, the result is quite general and the solution can be used to analyze transmission properties of a small hole of an arbitrary shape. The Bethe's expression for the fields behind the screen is correct only in the far-field zone of the aperture ($z>>\lambda$), as was

pointed out by Bouwkamp, who corrected the Bethe's solution for the near-field zone ($z<<\lambda$) [Bouwkamp 1950].

An analytical solution for electric field in the near-field zone in a general case is difficult, and numerical techniques are widely used [Leviatan 1987, Grober *et al.* 1996]. Various methods allow increasing the complexity of the problem, by specifying the geometry of the aperture and materials characteristics [Roberts 1989, Novotny 1994, Vasilyeva & Taflove 1998].

In the classical formulation of the problem, a small circular hole in an infinitely thin conducting screen is illuminated by a plane electromagnetic wave. Green's theorem can be used to describe electromagnetic fields on the other side of the screen. The electric field at any point $\vec{r}$ behind the screen is

$$\vec{E}(r) = \int_S \left[ -G(\vec{n}\cdot\nabla')\vec{E} + \vec{E}(\vec{n}\cdot\nabla' G) \right] d\sigma' \tag{4.1}$$

with the retarded Green's function

$$G(|\vec{r}-\vec{r}'|) = \frac{e^{ik|\vec{r}-\vec{r}'|}}{|\vec{r}-\vec{r}'|}. \tag{4.2}$$

The integral is taken over the surface, which encloses the whole space. A unitary vector $\vec{n}$ defines the surface of integration and points inside the volume. In order to find the field inside the volume, it is necessary to know the values of the field and its normal derivative on the surface *S*.

Note that Kirchhoff's diffraction theory is inadequate for this problem. The Kirchhoff's approximation consists of the assumptions that (1) the electric field and its derivative vanish everywhere except in the aperture; and (2) the values of the field and

derivative in the aperture are equal to the values of the incident wave in the absence of any screens. The approximation fails in the case of a small aperture in the metallic screen, because of significant perturbation of the field inside the aperture. This effect is particularly strong for the aperture of a size much smaller than the wavelength. Also, the boundary condition at a perfectly conducting surface does not require the normal to the surface component be zero, as it is assumed in the Kirchhoff's approximation. An absolutely different approach is necessary.

Green's theorem (4.1) can be rewritten in an alternative way [Jackson 1962]

$$\vec{E}(\vec{r}) = \int_S \left[(\vec{n}\times\vec{E})\times\nabla' G + (\vec{n}\cdot\vec{E})\nabla' G + ik(\vec{n}\times\vec{B})G\right] d\sigma' . \qquad (4.3)$$

This expression must be satisfied everywhere in the volume. However, for a point at the screen, the second and the third terms in the integral give rise to a tangential component of electric field and, therefore, violate the boundary condition at the conducting screen surface. Only the first term satisfies the boundary condition, giving electric field normal to the surface. Therefore, only the first term must remain in the expression [Bethe 1944].

The integral in Eq. 4.3 has a physical interpretation in terms of sources of charge and current. The wave transmitted through the aperture is considered as arising from equivalent currents in the aperture. The first term in the integral is equivalent to 'magnetic currents' in the plane of the aperture in a same way as the curl of the magnetic field is related to electric current.

Distribution of the surface magnetic currents $K$ inside the circular (or elliptic) aperture can be chosen to satisfy the boundary conditions everywhere in the plane of the

screen [Bethe 1944]. Then the integral over the entire surface can be reduced to the aperture area

$$\vec{E}(\vec{r}) = \int_{S_a} \vec{K}(\vec{r}') \times \nabla G(|\vec{r} - \vec{r}'|) d\sigma' \qquad (4.4)$$

This simple result implies that electric field of an illuminated aperture can be calculated everywhere as produced by magnetic currents inside the aperture. The

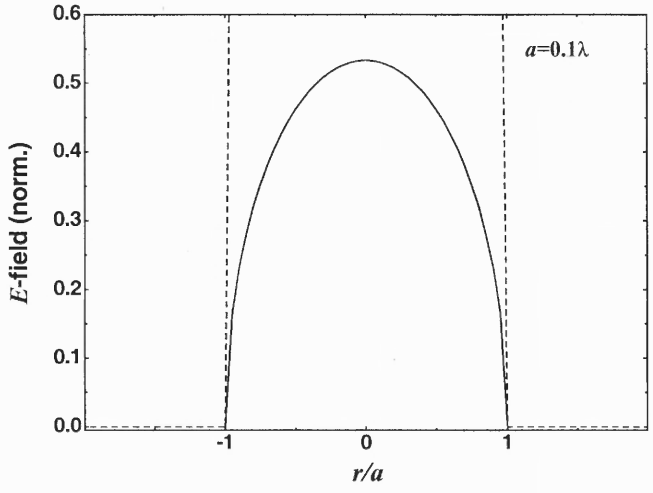


**Fig. 4.1.** Electric field in the cress-section of a subwavelength aperture of radius $a$=0.1$\lambda$ according to the Bethe's theory (solid curve). Polarization of the field is perpendicular to the line of cross-section. The amplitude is normalized to the amplitude of the incident wave. The dashed line shows the Kirchhoff's approximation, which assumes that the field is unity everywhere inside the aperture.

magnetic field determination is similar, although it involves introduction of 'magnetic charges' beside the currents. As an example of field calculation, Eq. 4.5 gives the Bethe's tangential components of electric field in the plane of the circular hole. The hole radius is $a$ and the incident electric and magnetic fields are $\vec{E}_0$ and $\vec{B}_0$ respectively.

$$\vec{E}_{\tan}(\vec{r}') = \vec{E}_{0,z} \times \vec{r}' \frac{1}{\pi\sqrt{a^2 - r^2}} + \frac{2ik}{\pi}(\vec{n} \times \vec{B}_0)\sqrt{a^2 - r^2} \qquad (4.5)$$

The first term is non-zero only if the plane wave is incident on the aperture at an angle. The last term is produced by the tangential incident field and, therefore, corresponds to a wave normally incident on the aperture screen. Figure 4.1 shows the electric field amplitude in the radial cross-section of the aperture, calculated using only the last term of Eq. 4.5. The aperture radius is 1/10 of the incident wavelength. The amplitude is normalized to the incident electric field. In the plane of the aperture, the field is clearly smaller than unity, as assumed in the Kirchhoff's approximation.

The field distribution depends also on the ratio of the aperture size to the wavelength. It implies that the transmission coefficient is not simply proportional to the aperture area. In fact, the total transmitted power of the normally incident plane wave can be found proportional to the sixth power of the aperture size and inversely proportional to the forth power of the wavelength

$$P = C\frac{a^6}{\lambda^4} \qquad (4.6)$$

where $C$ is a constant. The emission is in the normal direction and polarization is the same as of the incident wave. Note that the transmitted electric field scales as $a^3$ when the ratio of the aperture size to the wavelength decreases. If the electric field is measured, the signal attenuation is only a square root of the intensity attenuation.

Distribution of the fields behind the aperture is particularly interesting in the near-field zone. Bethe's theory, however, gives the correct analytical solution only for the distant fields. The near-field correction to the theory is discussed by Bouwkamp (1950).

The problem of finding the fields in the near-field zone can be also treated numerically. As discussed above, the radiation due to the aperture is equivalent to the field due to the surface magnetic currents. Using the current distribution obtained by Bethe, the magnetic field is obtained by numerical integration. Leviatan (1986) studied decay of the transmitted fields as a function of the distance from the aperture, as well as the issue of field confinement by the aperture.

The result shows that there are three spatial regions with various characteristic behaviors of the fields.

(1) Very close to the aperture the magnitude of the field remains constant as the distance $z$ increases from 0 to about $z=0.1a$.

(2) In the interval from about $z=0.1a$ to about $z=10a$, the field falls off with distance at an increasing rate, and approaches $z^{-2}$ dependence.

(3) The field amplitude decreases monotonically as $z^{-1}$ at longer distances.

The electromagnetic fields of the aperture can be interpreted as consisting of two parts: the radiating wave, which dominates at $z>\lambda/2$, and the evanescent wave, which contributes only at $z<10a$.

Spatial confinement of electromagnetic fields behind the aperture plays an important role in near-field microscopy. The radiation emanating from a small aperture is first collimated to the aperture size rather than the wavelength. The radiation remains confined within a distance of approximately one aperture radius. The pattern diverges rapidly beyond this confinement length.

### 4.2.2 Numerical Simulations based on FDTD Method

In all the methods discussed above, the incident field is assumed to be harmonic. The solution depends on the frequency of the field as $\omega^2$. In addition, it is valid only if the aperture size is much smaller than the wavelength. THz pulses contain a broad spectrum of frequencies, and some components have wavelengths on the order of the aperture size and smaller. Propagation of the THz pulses can be studied using the finite-difference time-domain (FDTD) numerical technique [Taflove & Hagness 2000]. The method is used to solve Maxwell's equations for electromagnetic fields in arbitrary space, and, therefore, the probe structure can be accounted in calculations. The time domain formulation allows the use of an experimentally measured waveform of the pulse as an incident field. Subsequently, the simulation results are compared with experimental findings directly. The FDTD method has been already applied to study THz pulse waveform transformation due to propagation through wide slits [Bromage *et al.* 1998]. A good agreement with experimental findings was shown in this work.

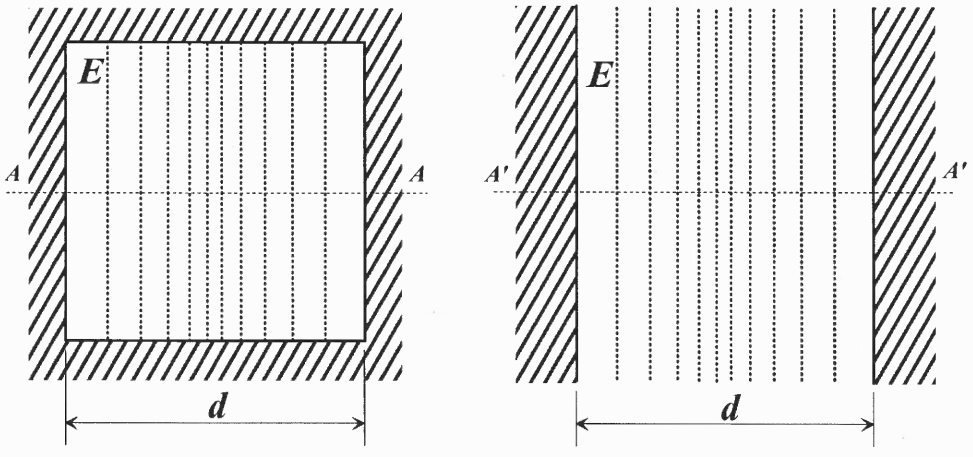


**Fig. 4.2** Analogy between an aperture and a slit oriented parallel to the electric field polarization. The electric field lines are shown by the vertical dashed lines. Electric field distributions along the cross-section *AA* through the aperture and along the cross-section *A`A`* through the slit are similar.

Complete calculations of the fields in a specified volume can be time consuming, because the algorithm considers every point of the space in every time step. However, the problem can be reduced to a two-dimensional case, which corresponds to an infinitely long slit. We can make this simplification because the electric field distribution in the cross-section of a square-shaped aperture is similar to that of a slit oriented parallel to the polarization direction [Fig. 4.2]. The two-dimensional model provides a good qualitative description of the pulse propagation, but reduces the computation time substantially. The model can be used to compare various designs of the near-field probe in order to optimize the probe performance.

Certain requirements must be satisfied in order to model THz pulse propagation inside the near-field probe.

(1) The incident field must be modeled as a plane wave with specified propagation direction, polarization, and time waveform.

(2) The incident field must have constant amplitude in any plane parallel to the wavefront, and the waveform profile and amplitude must remain constant as the pulse propagates in the modeling space, except when it diffracts at the aperture.

(3) The probe structure must be completely specified in the FDTD grid.

The scattered field formulation is used for calculation of the diffracted field. This approach is based on the linearity of Maxwell's equations. The physical total electric and magnetic fields can be decomposed in the following manner:

$$\vec{E}_{\text{total}} = \vec{E}_{\text{inc}} + \vec{E}_{\text{scat}} \tag{4.6a}$$

$$\vec{H}_{\text{total}} = \vec{H}_{\text{inc}} + \vec{H}_{\text{scat}} \tag{4.6b}$$

$\vec{E}_{inc}$ and $\vec{H}_{inc}$ are the values of the incident-wave fields. These are the fields that would exist in vacuum if there were no material in the modeling space. The algorithm requires that $\vec{E}_{inc}$ and $\vec{H}_{inc}$ are known at all points of the space lattice at all time steps. $\vec{E}_{scat}$ and $\vec{H}_{scat}$ are the values of the scattered-wave fields, which are initially unkown. These fields result from the interaction of the incident wave with the material in the space lattice.

The incident-field is calculated using the FDTD method. The incoming *x*-polarized THz pulse propagates in *z*-direction, therefore fields are invariant with respect to *y*-coordinate. This allows considering the propagation problem in one-dimensional space, instead of the whole modeling domain. The *E*-field is specified at the left boundary at every time step, and the incident field in every lattice point is subsequently found using equations

$$E_x\Big|_{k+1/2}^{n+1/2} = E_x\Big|_{k+1/2}^{n-1/2} - \frac{\Delta t}{\varepsilon_0 \Delta z}\left(H_y\Big|_{k+1}^{n} - H_y\Big|_{k}^{n}\right) \tag{4.7a}$$

$$H_y\Big|_{k}^{n+1} = H_y\Big|_{k}^{n} - \frac{\Delta t}{\mu_0 \Delta z}\left(E_x\Big|_{k+1/2}^{n+1/2} - E_x\Big|_{k-1/2}^{n+1/2}\right) \tag{4.7b}$$

The calculations simulate the *E*- and *H*-field of a plane wave propagating along the *z*-direction. The wave has a time waveform specified at the left boundary. The amplitude and the time dependence are maintained as the wave propagates through the space.

The boundary condition for the *E*-field is defined using the experimentally measured time waveform of the THz pulse. The electric field of the pulse is usually measured with a time step of ~30 fs. In the FDTD calculations, however, the time step has to be about 10 times smaller in order to obtain a stable and accurate solution. To generate the boundary condition with a required time increment, the measured waveform

must be interpolated and $E$-field values found for the refined time vector. The boundary condition, defined in this manner, models a pulse waveform very accurately, but it adapts the experiment-related noise. High-frequency noise can result in significant discrepancy of the solutions, because the probe structure exhibits high-pass properties. A small aperture preferentially transmits the high frequency components of the incident field, while it significantly attenuates the slower varying fields. Therefore, the transmitted field contains noise at a much higher level, compared to that in the incident field. In order to reduce the error, the boundary condition is generated applying Fourier frequency filter before interpolation. Figure 4.3 shows the experimentally measured $E$-field of the pulse ($\Delta t$=33 fs) and the waveform for the boundary condition ($\Delta t$=4.7 fs), generated using Fourier filter and interpolation.

Given that the incident field is specified at every point of space and time, the algorithm separately calculates the scattered field. The total $E$- and $H$-field time waveform are obtained by adding the computed incident-field time dependence and the scattered-field time dependence at each point.

The scattered field is calculated as a result of interaction of the incident field with the probe structure. At the surface of the metallic screen, there must be zero total tangential $E$-field (in the perfect electric conductor (PEC) approximation)

$$\vec{E}_{\tan}\Big|_{\text{total}} = 0 \tag{4.8}$$

Therefore, by Eq. 4.6(a):

$$\vec{E}_{\tan}\Big|_{\text{scat}} = -\vec{E}_{\tan}\Big|_{\text{inc}} \tag{4.8}$$

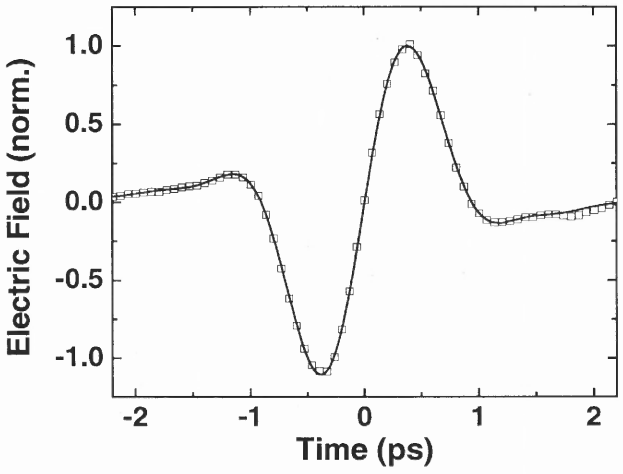


**Fig. 4.3.** Measured electric field of the THz pulse (squares), and the waveform used in FDTD simulation.

must hold at the structure surface at all time steps. The scattered wave has surface tangential components equal and opposite to those of the incident wave. Therefore, the surface of PEC acts as a source of scattered field.

The incident field induces also polarization and currents in dielectric structures. The scattered-field equations, therefore, contain terms, corresponding to these contributions. Losses in the dielectric are not included in the model ($\sigma_D$=0), which is a good approximation for semi-insulating GaAs ($\rho$=$10^7$ Ohm·cm). Starting with Maxwell's curl equations for the total field, the scattered-field equation can be derived by subtracting the equation for the incident field. The curl equation for magnetic field, for example,

$$\varepsilon \frac{\partial \vec{E}_{\text{total}}}{\partial t} = \nabla \times \vec{H}_{\text{total}} . \tag{4.9}$$

The incident field is defined as propagating in a vacuum

$$\varepsilon_0 \frac{\partial \vec{E}_{\text{inc}}}{\partial t} = \nabla \times \vec{H}_{\text{inc}} . \tag{4.10}$$

Therefore, the scattered field equation can be written as follows

$$\varepsilon \frac{\partial \vec{E}_{\text{scat}}}{\partial t} = \nabla \times \vec{H}_{\text{scat}} - (\varepsilon - \varepsilon_0) \frac{\partial \vec{E}_{\text{inc}}}{\partial t}. \tag{4.11}$$

The last term in Eq. 4.11 describes response of the dielectric media to the incident wave. The equation can be realized numerically substituting the space and time derivatives by the central differences

$$E_{\text{sct}x}\Big|_{j+1/2,k+1/2}^{n+1/2} = E_{\text{sct}x}\Big|_{j+1/2,k+1/2}^{n-1/2} + \frac{\Delta t}{\varepsilon}\left( \frac{H_{\text{sct}z}\Big|_{j+1,k}^{n} - H_{\text{sct}z}\Big|_{j,k}^{n}}{\Delta y} - \frac{H_{\text{sct}y}\Big|_{j,k+1}^{n} - H_{\text{sct}y}\Big|_{j,k}^{n}}{\Delta z} \right) - \frac{(\varepsilon - \varepsilon_0)}{2\varepsilon}\left( E_{\text{inc}x}\Big|_{j+1/2,k+1/2}^{n+3/2} - E_{\text{inc}x}\Big|_{j+1/2,k+1/2}^{n-1/2} \right) \tag{4.12a}$$

Magnetic field components are calculated similarly

$$H_{\text{sct}y}\Big|_{j,k+1}^{n+1} = H_{\text{sct}y}\Big|_{j,k+1}^{n} - \frac{\Delta t}{\mu \Delta z}\left( E_{\text{sct}x}\Big|_{j,k+3/2}^{n+1/2} - E_{\text{sct}x}\Big|_{j,k+1/2}^{n+1/2} \right) \tag{4.12b}$$

$$H_{\text{sct}z}\Big|_{j+1,k}^{n+1} = H_{\text{sct}z}\Big|_{j+1,k}^{n} + \frac{\Delta t}{\mu \Delta y}\left( E_{\text{sct}x}\Big|_{j+3/2,k}^{n+1/2} - E_{\text{sct}x}\Big|_{j+1/2,k}^{n+1/2} \right) \tag{4.12c}$$

Equations 4.7, 4.8, 4.10, and 4.12 completely describe THz pulse propagation in the modeling space. The near-field probe geometry is specified by defining dielectric permitivity in every cell of the space lattice. The PEC condition [Eq. 4.10] is applied to the cells that correspond to the metallic screen. The model reproduces the probe geometry (in the two dimensional space) and simulates the THz pulse coupling into the probe.

An example of the probe geometry, modeled in two-dimensional space, is shown in the Figure 4.4. The perfectly conducting screen divides space into two media with dielectric constants of $\varepsilon$=1 (air) and $\varepsilon$=13 (GaAs; shown gray on the diagram). The discontinuity of the screen models a 30 μm 2-D aperture (slit). The dielectric extends into

the air half-space for a precise modeling of the probe geometry. A uniform Cartesian two-dimensional space lattice with a 1 $\mu m^2$ cell and a 4.7 fs time step is used for calcuations. The computational domain size is 460×350 $\mu m^2$, and the modeled time interval is 7 ps.

The calculated field distribution map is shown by contour lines of equal intensity. The simulations demonstrate that the electric energy density of the THz pulse (time integrated $E^2$) is confined immediately after the aperture. The field of the pulse diverges rapidly as the pulse propagates inside the probe.

The scattered field formulation works well for propagation of 0.5 THz pulses inside the near-field probes with apertures as small as 30 $\mu m$. Application of the described method to smaller apertures can create a computational error, also known as subtraction noise. Inside the probe, the incident and the scattered fields are nearly equal and opposite. The normal computational uncertainties in the scattered and the incident

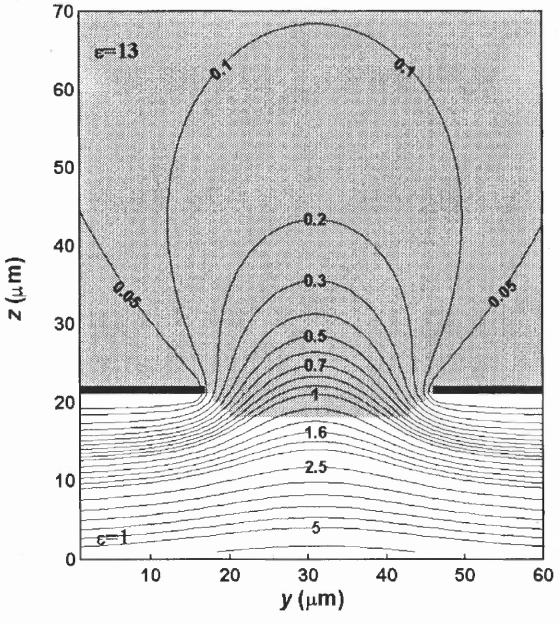


**Fig. 4.4.** Two-dimensional map of the pulse intensity ($\int E^2 dt$) inside the near-field probe integrated over time. The intensity is normalized to its value at the aperture center.

field can be magnified in the process of adding the two fields in order to obtain the total field.

This effect is strongly pronounced if the incident field is defined analytically, rather then by applying the FDTD algorithm in free space. In this case, the incident-field component does not suffer phase errors due to numerical dispersion. The scattered field, on the other hand, is forced to propagate through the FDTD space lattice and, therefore, gain the phase errors. If the incident field is found using the same numerical algorithm as for the scattered field, the phase errors in the incident and scattered field tend to compensate. The complete cancellation, nevertheless, is not possible, because the incident and scattered field are not identical. For accurate computation of fields transmitted through smaller apertures, another algorithm, known as the total field formulation, is required [Taflove & Hagness 2000].

### 4.2.4 Experimental Study of the Pulse Propagation inside the Probe

Propagation of the THz pulse inside the probe can be studied experimentally as well. One of the main questions is how the amplitude of the transmitted field decreases as a function of the distance from the probe aperture. To observe the electric field decay close to the aperture experimentally, near-field probes are fabricated with various separations between the probe aperture and the photoconducting receiving antenna. A schematic cross-section of the probe is given in Figure 4.5. The probe is based on a LT GaAs photoconducting switch (with a 10 μm gap and a 60 μm long dipole antenna), which is mounted on a transparent sapphire substrate. A 600 nm thick gold film is deposited on the surface of the GaAs layer except for a 30x30 $\mu m^2$ square-shaped aperture below the dipole. The GaAs layer thickness can be adjusted by mechanical polishing before depositing metal. Probes

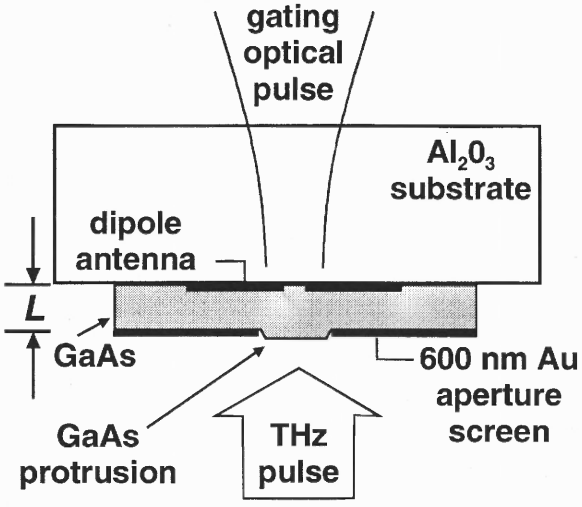


**Fig. 4.5.** The schematic cross-section of the near-field collection mode probe. *L*, thickness of the GaAs layer, sets the distance from the aperture to the dipole antenna.

with five aperture-to-dipole separations: $L$=7, 16, 21, 47, and 110 $\mu$m were studied. The separation is measured by a profilometer with an accuracy of 1-2 $\mu$m. A GaAs protrusion extends through the aperture by ~3.5 $\mu$m to achieve more efficient coupling of the THz radiation into the aperture. An optical pulse from a Ti:Sapphire laser gates the photoconducting antenna through the sapphire substrate. The 0.5 THz single-cycle pulse beam generated by a separate photoconducting switch is focused to a ~2 mm diameter spot, and is normally incident on the probe. This arrangement is similar to a near-field microscope in collection mode, where a uniformly illuminated sample is scanned in front of the probe [Betzig *et al.* 1987].

The black circles in Figure 4.6 indicate the measured electric field peak amplitude of the THz pulse. Clearly, the amplitude decreases rapidly as the aperture-to-dipole separation increases. The probe with the shortest aperture-to-dipole separation ($L$=7 $\mu$m) senses the electric field at the peak of the pulse, which is ~12 times stronger, compared to

the probe with $L$=110 $\mu$m. It can be seen that the electric field amplitude drops approximately as $L^{-1}$ (dash-dotted curve). The solid curve in Figure 4.6 shows the calculated electric field peak amplitude as a function of the distance from the aperture along the $z$-axis passing through the center of the aperture. As the pulse propagates inside the dielectric, the field amplitude drops rapidly and approaches a decay rate of $L^{-1/2}$ for distances greater than ~80 $\mu$m. The decay rate is slower compared to the experimental findings, because the model does not take into account the field divergence in the direction perpendicular to the $yz$-plane. However, the field divergence is small immediately behind the aperture, and both the experiment and the simulations give comparable results for the electric field strength.

Accuracy of the experimental measurement relies on the precise fabrication of the samples and the setup alignment. In order to decrease the error, electric field peak

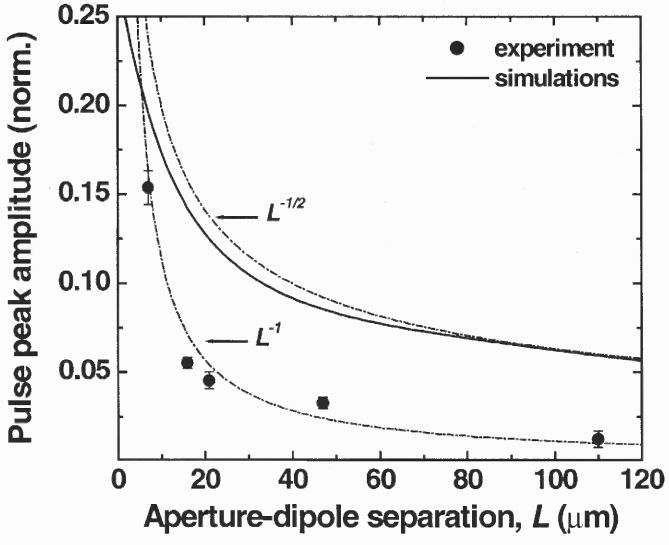


**Fig. 4.6.** Measured (circles) and calculated (solid line) electric field amplitude of the pulse as a function of the distance from the aperture. The dash-dotted curves represent $L^{-1}$ and $L^{-1/2}$ behavior for comparison.

intensity is averaged over few measurements, each taken after the system realignment. The error bars indicate the standard deviation from the mean value.

An important property of a subwavelength aperture is a frequency dependent transmission coefficient. An incident pulse, scattered by the aperture, changes its time-domain waveform and the spectrum. This effect is observed experimentally and the waveform agrees with the numerical simulations. Figure 4.7(a) shows the calculated field 7 $\mu$m away from the plane of the aperture (solid line) as well as the waveform, experimentally measured using the probe with $L$=7 $\mu$m (dots). The normalized incident pulse waveform is shifted upward for clarity and is shown in dash curve as a reference. The single-cycle waveform of the incident pulse transforms into the faster oscillating waveform. The spectral content of the detected field shifts to higher frequencies compared to the spectrum of the incident pulse.

It should be mentioned that the measured THz pulse exhibits longer oscillations compared to the simulated waveform, though the initial temporal transformation of the pulse is in good agreement with the simulations. The blue shift of the spectrum is well modeled by the simulations, as can be seen in the Figure 4.7(b). The central frequency of the calculated spectrum matches the experimental findings, although the spectral width of the measured pulse is smaller. The frequency dependence of the transmission coefficient of the subwavelength aperture will be discussed in detail in Chapter 5.

The results demonstrate that the sensitivity of the collection mode probe based on a photoconducting antenna can be significantly improved if the THz electric field is detected in the immediate vicinity of the collection aperture. As verified experimentally, the spatial resolution of the probe is not affected by the changes in the distance between

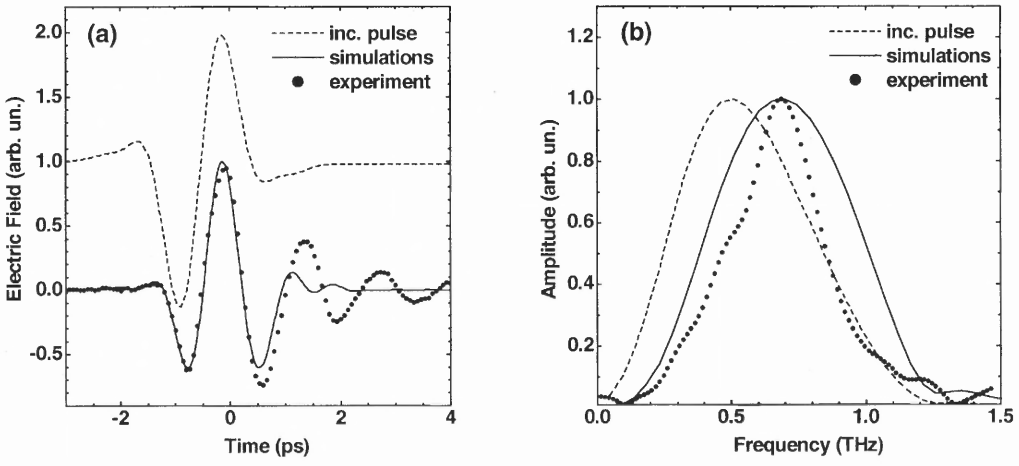


**Fig. 4.7.** Transformation of the single-cycle 0.5 THz pulse after transmission through the aperture. (a) normalized measured (dots) and calculated (solid line) time domain waveforms for the $L$=7 μm probe. The dashed line represents the normalized waveform of the incoming pulse shifted upward for clarity. The corresponding spectra are shown in (b).

the aperture and the photoconducting antenna, since resolution is determined solely by the aperture size. The proposed computational method models the pulse propagation inside the near-field probe. The waveform deformation and the spectral shift are in good agreement with experiment, while the electric field decay can only by treated qualitatively.

### 4.2.4 Modal Analysis

The field in the near-field zone of the subwavelength aperture can be divided into modes with real and imaginary longitudinal $k$-vectors [Grober *et al.* 1996]. The latter are usually referred to as evanescent modes. Electric field amplitude of the evanescent modes is significantly larger than that of the propagating modes at the distances from the aperture $z<d/2$. As the distance $z$ increases the amplitude of both types of modes decreases, but decay is more rapid in the case of the evanescent modes. At a distance approximately equal to the aperture size their contribution is comparable. Further out ($z>d$) the

evanescent modes are practically negligible. Only modes characterized by real wavenumbers can transfer energy into the far-field zone ($z>>\lambda$). However, if the detecting element is moved sufficiently close to the aperture, the evanescent modes contribute to the measured field and, therefore, increase the probe sensitivity.

The mode contribution to the signal at different $z$ can be estimated using the modal analysis. Electric field distribution in the plane of the aperture (from the Bethe's theory) is expressed as the Fourier integral of the spatial frequencies similar to Eq. 3.1. Amplitudes of the spatial frequencies are found by the inverse Fourier transform [Grober

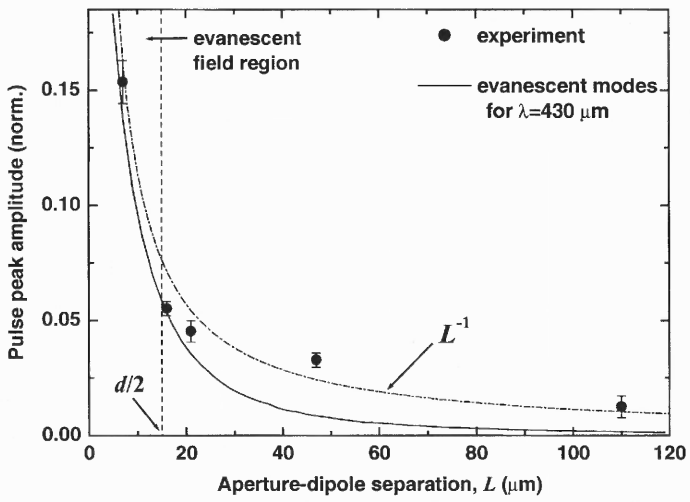


**Fig. 4.8.** Measured (circles) pulse amplitude as a function of the distance from the aperture. The solid line shows amplitude of the evanescent components only calculated for $\lambda$=430 $\mu$m, and the dashed line shows $L^{-1}$ behavior for comparison.

*et al.* 1996]. Components with the transverse vector $k_t$ exceeding the value of the incident field wavevector $2\pi/\lambda$ are evanescent. The electric field of the evanescent waves decays with the distance from the aperture. The solid curve in Figure 4.8 shows the field amplitude due to the evanescent components of a $\lambda$=430 $\mu$m wave incident on a 30 $\mu$m-

diameter aperture. The wavelength corresponds to the spectral maximum of the THz field experimentally detected by the probe. The space behind the aperture is filled with a high refractive index material that reduces the effective wavelength.

In spite of the single wavelength approximation, the calculated evanescent wave amplitude agrees well with the experimental data at $z<d/2$, where contribution of the evanescent modes is dominant. Starting at the distance $z\sim15$ $\mu$m, corresponding to $\sim d/2$ in normalized units, the calculated amplitude of the evanescent modes becomes smaller than the measured amplitude. This fact confirms the diminishing contribution of the waves with imaginary $k$-vector at large $z$.

## 4.3 Radiation Coupling through the Probe Aperture

It was mentioned earlier that the radiation coupling through a subwavelength aperture is very weak. The small signal restricts near-field microscopy to a certain spatial resolution, defined by the aperture size. Improvement in radiation coupling into the probe, therefore, yields the better image clarity. In the developed near-field probe a high refractive index cone, protruding through the aperture, helps to transmit more energy of the THz pulse through the probe aperture.

The transmission coefficient of a subwavelength aperture is a function of both the aperture size and the wavelength. According to the Bethe's solution [Bethe 1944], the electric field amplitude of the transmitted wave decreases as the third power of the aperture size and the second power of the inverse wavelength. This wavelength dependence can be effectively used to improve the near-field probe performance. The wavelength of an electromagnetic wave becomes smaller inside a dielectric medium,

therefore the aperture, embedded inside the dielectric, passes more radiation. The factors that can increase the transmission coefficient of a subwavelength aperture and improve the near-field probe performance are considered in this chapter.

### 4.3.1 Subwavelength aperture on dielectric interface.

An electromagnetic wave in dielectric medium is characterized by its wavelength $\frac{\lambda_0}{n}$, where $\lambda_0$ is the vacuum wavelength. From the theory of metallic waveguides, the cutoff frequency decreases if a dielectric material fills the volume of the waveguide. Therefore, a higher transmission is expected if the aperture is filled with the dielectric material.

To demonstrate the effect of the dielectric media on the exit side of a subwavelength aperture, we model an aperture in free space and an aperture at a vacuum-dielectric interface. Transmission is compared for the two cases using the 2-D FDTD numerical method (Sec. 4.2). A single-cycle THz pulse is normally incident on the

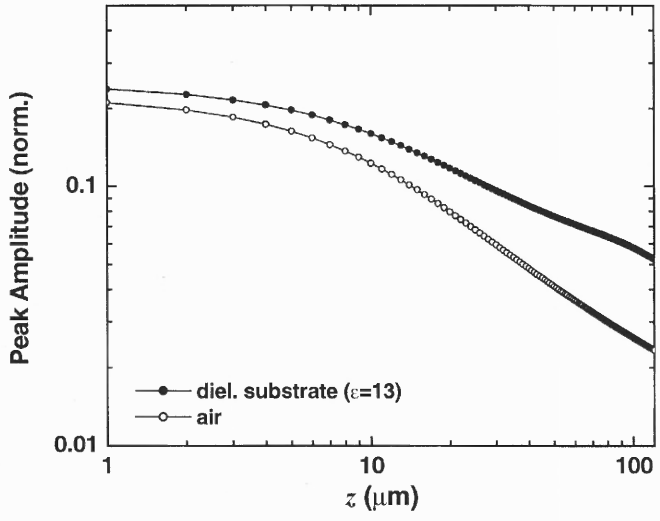


**Fig. 4.9.** Electric field amplitude of the pulse transmitted through the 30 $\mu$m aperture.

aperture. The size of the aperture is chosen to be 30 $\mu$m, which is $\sim\frac{\lambda_0}{17}$ for the central wavelength of the incident pulse. The electric field amplitude of the pulse along $z$-axis is shown in Figure 4.9. In the case of the aperture on the dielectric, the pulse peak intensity is higher by ~15% at $z<3$ μm. The difference becomes more evident further out. The radiating part is the dominant contribution to the electric field of the transmitted pulse at the large distances $z$. A shorter effective wavelength inside the dielectric allows a larger part of the pulse spectrum to propagate through the aperture with less attenuation. Therefore, the far-field transmission coefficient is higher for the aperture on dielectric.

### 4.3.2 Improvement of Radiation Coupling by means of a GaAs Cone.

Placing the aperture on the high dielectric constant interface has a drawback of inducing additional reflection from the dielectric surface. The reflection can be reduced by means of a dielectric cone. Protruding through the aperture, a tapered dielectric tip decreases reflection and, therefore, the radiation coupling through the aperture improves.

The tapered dielectric cone is known to decrease reflections from the interface [Zucker 1961]. The taper gradually changes its effective refractive index from the tip to the base. The effect can be demonstrated using 2-D FDTD simulations. The near-field probe geometry is modeled as a perfectly conducting screen, which has a 30 $\mu$m wide opening. The computational space is divided using a uniform Cartesian two-dimensional lattice with a $1\mu m^2$ cell. The GaAs protrusion is modeled by assigning the dielectric constant $\varepsilon$=13 to selected cells. Three cases include a GaAs cone of 45° half-angle, a 3 $\mu$m dielectric protrusion with a flat surface, and a plane aperture at the flat air-GaAs interface. An incident plane wave is simulated using a single-cycle temporal profile of the

0.5 THz pulse measured experimentally with a regular photoconducting antenna. The electric field is polarized parallel to the slit edge ($x$-direction).

Fig. 4.10 shows the field intensity of the transmitted through the aperture THz pulses for these three cases, compared to an aperture in free-space (air). The intensity of the pulse is calculated by integration of the $E^2$ over the duration of the pulse, and is normalized to the value in the middle of the aperture without the protrusion. Results demonstrate that the full cone probe is more efficient than the other two. The peak

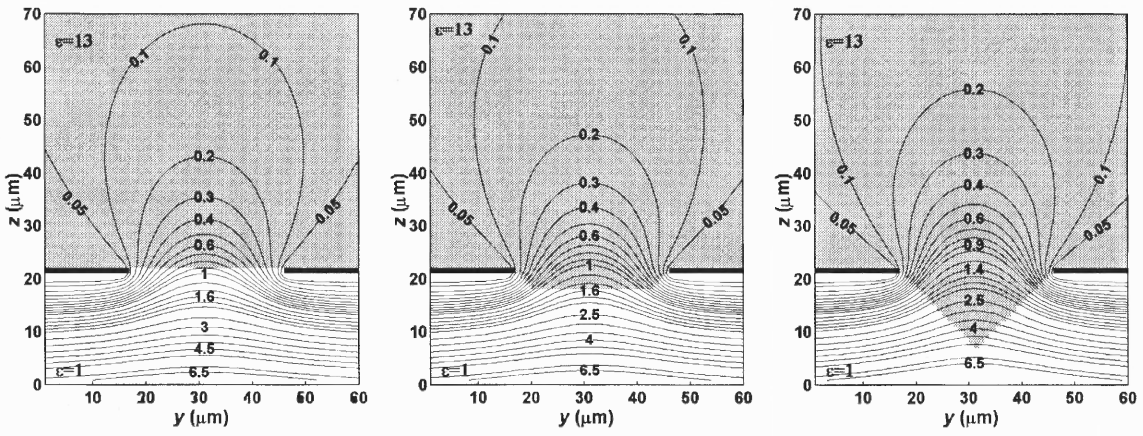


**Fig. 4.10.** Maps of intensity distribution of the transmitted THz pulse for various probe designs.

amplitude of the electric field of the transmitted pulse as a function of distance from the aperture is shown in Figure 4.11. The peak amplitude in the case of the full cone is ~25% higher compared to the plain aperture probe and ~15% higher compared to the probe with the small (3 $\mu$m) GaAs protrusion. Waveforms calculated at a distance of 7 $\mu$m from the aperture plane, and the corresponding spectra are presented in Figure 4.12. The full cone enhances coupling of the high frequency components more than the low frequency components. Consequently, the spectrum shifts.

Experimental estimation of the effect of the probe geometry for a small aperture probe is difficult. The far-field transmission coefficient is very small, thus the measurements are not very accurate or even impossible. The error is even higher for the near-field zone measurements, because a small variation in the aperture-dipole separation brings a significant change in measured electric field.

The amount of radiation transmitted to the other side of the aperture, depends also on the thickness of the metallic screen. In general, the aperture can be considered as a metallic waveguide, where the length is very small. Propagation inside the waveguide is described by the classical equations for various modes [Jackson 1962]. All the TM and TE modes are characterized by the imaginary $k$-vector, if the cross-section of the waveguide is smaller than $\sim\lambda/2$. In this case, the wave amplitude decays exponentially along the waveguide, and the waveguide length defines the total attenuation. It must be mentioned that the metallic screen can not be made infinitely thin, because it becomes

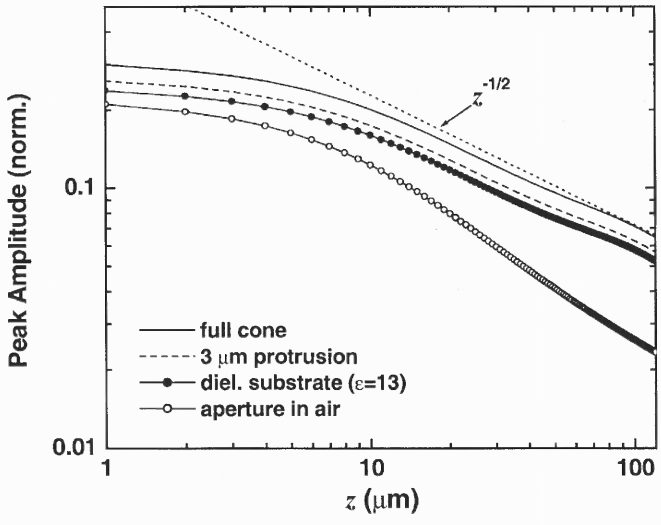


**Fig. 4.11.** Electric filed of the transmitted pulse as a function of distance from the aperture.

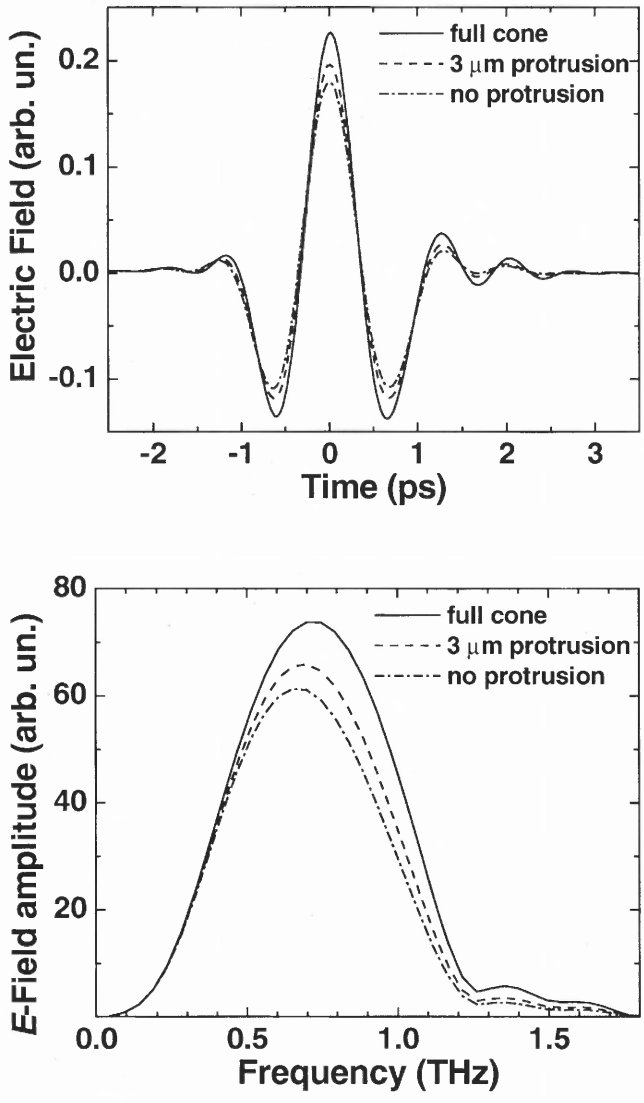


**Fig. 4.12.** Calculated pulse shapes and corresponding spectra at a distance of 7 $\mu$m from the aperture plane.

transparent for THz pulses. The penetration depth of gold, for example, at $f$=1 THz is ~50 nm. The screen thickness has to be large enough to block the THz pulse to the level of the noise signal. The issue of the screen thickness will be considered in the next chapter. It must be mentioned, however, that a 600 nm gold screen can be considered infinitely thin for the 30 $\mu$m aperture.

## 4.4 Fabrication of the Integrated Near-Field Probe

In this section, fabrication of the near-field probes is described. The process includes three main stages: preparation of low-temperature grown GaAs epilayer, lithographic printing of the dipole antenna, and fabrication of the integrated near-field probe. The quality of the photoconductor is very important and the related issues are discussed here as well.

### 4.4.1 Low Temperature Grown GaAs

Fast optical response of the material is a crucial quality for the THz detectors. The response time is mainly determined by the dynamics of nonequilibrium charge carriers. Various classes of semiconductors, e.g. radiation-damaged, impurity-dominated, polycrystalline, and amorphous [Ganikhanov *et al.* 1995, Chin *et al.* 1996], have been investigated for the fast carrier lifetime and detection of THz radiation. In the past two decades, low-temperature grown (LT) III-V semiconductors with subpicosecond carrier lifetime were developed. The fast optical response in LT semiconductors is due to the incorporation of excess group-V atoms during LT growth [Leitenstorfer 2000]. Annealed GaAs films grown by molecular beam epitaxy at temperatures 180-300°C, far below the temperature of crystallization, have the properties of high resistivity, high carrier mobility, and short carrier lifetime. These crucial qualities make LT GaAs an excellent material for THz detectors. The carrier lifetime defines the bandwidth and mobility determines the sensitivity of a detector. Low dark current provides a large dynamic range.

The excess arsenic atoms form As anticites and Ga vacancies during the growth [Warren 1990, Look 1990]. In as-grown materials photoexcited electrons are rapidly

trapped in the point defects. This process is followed by a slow recombination. The anticites ($As_{Ga}$) have energies close to the center of the band gap and can be in the neutral charge $As^0$ state or in the positive charge $As^+$ state. Since the $As^+$ donor centers are compensated by the Ga-vacancies acting as acceptors, the $As^+$ equilibrium concentration is determined by the density of the Ga-vacancies and is usually less then the tenth of the $As^0$ concentration [Liu *et al.* 1994]. The energy levels of the Ga-vacancies are located in the lower half of the band gap.

An optical pulse with energy exceeding the band gap creates carriers mainly through interband and $As^0$-conduction band (CB) transitions. After the fast intraband carrier thermolization, the carriers are trapped in the $As^+$ centers with a subpicosecond characteristic time [Seigner *et al.* 1996]. The fast removal of electrons from the CB is not due to electron-hole recombination, which occurs at a longer time scale [Lochtefeld *et al.* 1996]. The density of the $As^+$ traps is a combined density of the $As^+$ centers in equilibrium and the centers created by the optical $As^0$-CB transition. As a result, an effective depopulation of the CB is limited by the availability of the charged $As^+$ trapping centers.

The carrier lifetime in LT GaAs depends on growth temperature and post-growth annealing conditions. At lower growth temperatures, the recombination of the trapped carriers becomes slower, whereas the carrier trapping becomes faster [Siegner *et al.* 1996]. This correlates to the fact that the growth temperature varies the amount of excess arsenic incorporated into the epilayers. The lower growth temperature results in the higher content of the excess arsenic, evaluated using the TEM cross-sectional analysis of the LT GaAs epilayers [Liliental-Weber *et al.* 1993, Harmon *et al.* 1993].

As-grown LT GaAs is highly conductive, however, after annealing to temperatures of 600°C and higher, the GaAs becomes insulating. On the other hand, the carrier lifetime increases with the annealing temperature. The annealed samples form precipitates of the excess arsenic [Melloch *et al.* 1990, Warren *et al.* 1990]. The size and the spacing between the precipitates depend on the annealing temperature, varying between 2-20 nm and 10-100 nm respectively. The higher the annealing temperature the larger the precipitates and the spacing between them tend to be. The material is characterized by a subpicosecond relaxation time if the precipitate spacing is smaller than ~20 nm (Harmon *et al.* 1993).

The carrier lifetime can be determined from the measurements of the transient reflectivity or absorption induced by an ultrashort pump laser pulse through carrier excitation. By measuring the intensity of a weak probe pulse, either reflected or transmitted, as a function of the delay between pump and probe pulses, the free carrier

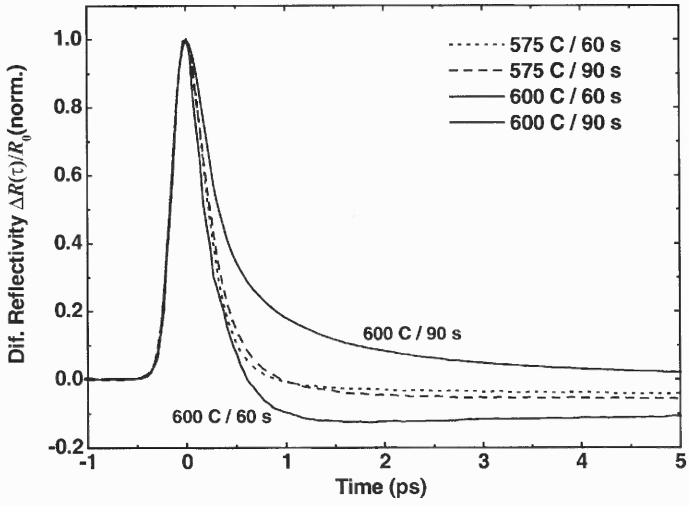


**Fig. 4.13** Normalized transient differential reflectivity of typical LT GaAs (T=300°C). Variation of the annealing condition results in changes of the dynamics of the carriers.

concentration dynamics after the pump pulse can be extracted. Figure 4.13 shows transient differential reflectivity traces for typical annealed LT GaAs samples. The transient reflectivity experiments and carrier dynamics in LT GaAs are discussed in detail in Appendix A.

### 4.4.2 Photoconducting Antennas

A 1-$\mu$m thick layer of GaAs is grown at a below crystallization temperature of 280-300°C by molecular beam epitaxy on <100> oriented semi-insulating GaAs. The material is subsequently annealed at 600°C for 1 min in forming gas.

The dipole antenna is fabricated on LT GaAs surface by using conventional lithography and the photoresist lift off technique. The structure consists of two 1 mm long parallel metallic striplines separated by a distance of 30-100 $\mu$m ($S$), and a dipole antenna located between the striplines [Fig. 4.14(a)]. A 5-10 $\mu$m photoconducting gap in the center of the dipole antenna is used for optical excitation. Performance of various antenna designs is discussed by Cai in his in dissertation (1998). To form a good contact with the semiconductor surface a metallic layer containing Ge/Au/Ni/Au – 165/335/200/3000 A is deposited on the surface. Alternative recipes may be used as well (e.g., Ge/Ni/Ge/Au/Ag/Au–50/50/132/268/1100/3000A, or Ni/AuGe/Ni/Au–100/800/200/3000A). Antennas fabricated according this recipe can be used for conventional generation and detection of THz radiation.

### 4.4.3 Integrated Near-Field Probe

Design of the integrated near-field detector requires a thin GaAs layer. This can be achieved by transferring the antenna on a transparent substrate. Optical gating of this

antenna type is realized through the transparent substrate. The antenna is glued to the transparent substrate, such as sapphire, with a high temperature optical epoxy (Epotek 353ND), with metal electrodes facing the sapphire. The epoxy is cured according to a three-step schedule (80°C – 1 h., 120°C – 1 h., 150°C – 1 h.) for higher strength in order to withstand chemical etching. The GaAs substrate is thinned by means of mechanical polishing to a desired thickness, which can be made as small as a few microns.

For the near-field probe, an aperture with a protruding GaAs taper is formed above the gap of the photoconducting antenna. First, the taper is etched on the surface of GaAs when the surface is masked with a circular or square photoresist pattern. An isotropic etching solution of hydrobromic and nitric acid ($HBr : HNO_3 : H_2O$ - 2 : 2 : 17) provides a relatively fast etching rate (~0.5-1.0 $\mu$m/min depending on temperature and freshness on the solution). The etching process results in a taper with a cylindrical symmetry and a smooth surface. The etching solution undercuts the photoresist sharpening the taper. The process is continued until a required thickness of GaAs is etched (usually ~1-5 $\mu$m). The photoresist remains on top of the taper and, covering the etched structure, serves as a mask to form the metallic aperture. The photoresist is removed after deposition of a 600 nm thick gold film (10 nm of Ti is deposited before Au as a gluing layer). The final structure contains the metallic film with the aperture defined by the shape of the photoresist mask, and the GaAs taper, protruding through the aperture. The aperture is separated from the dipole antenna by the GaAs layer.

In order to reach the contacts of the photoconducting antenna buried between the sapphire substrate and GaAs, the GaAs layer is etched away on the side of the structure. First, the metal screen is removed in this area and the remaining part of the structure is

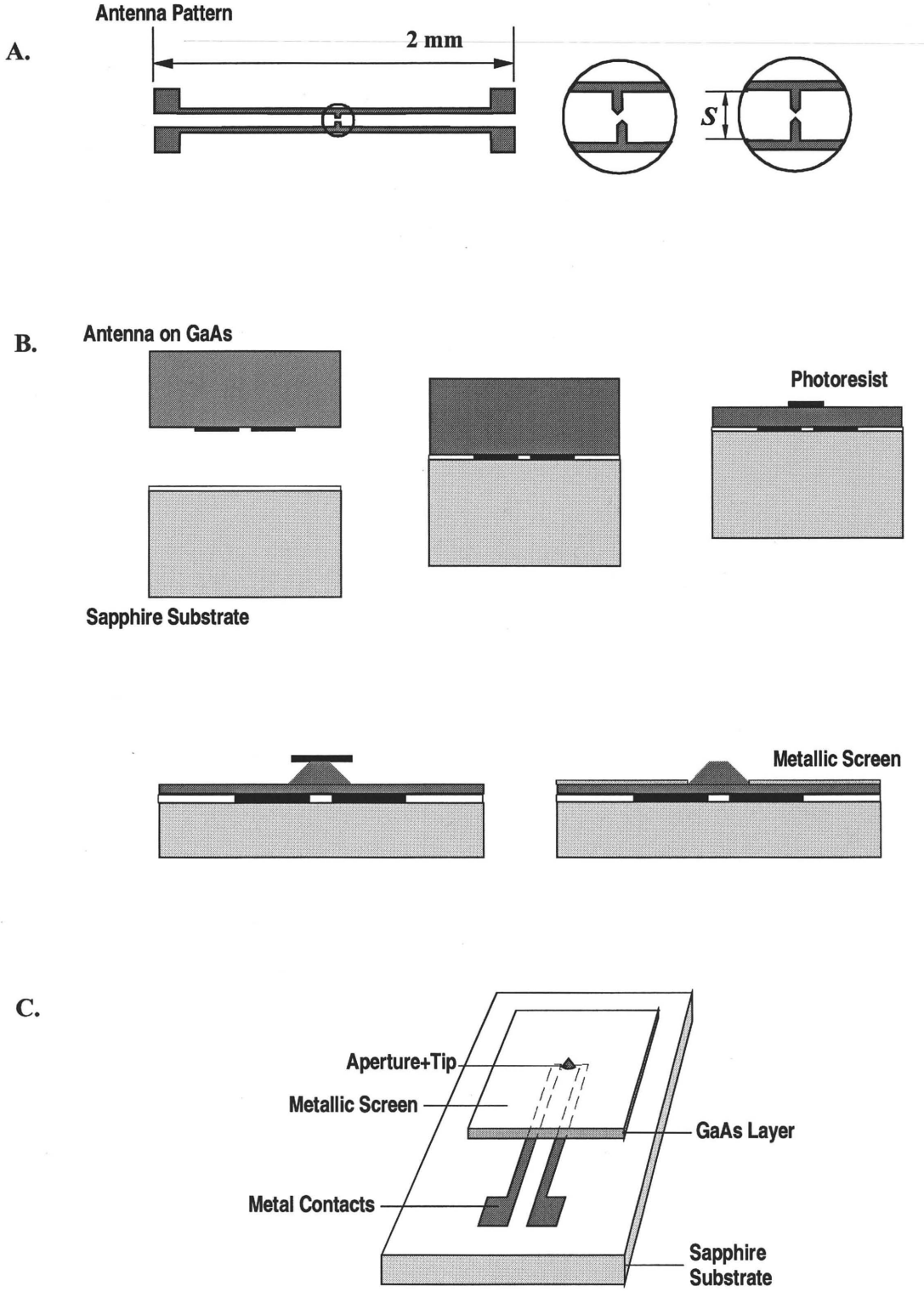


**Fig. 4.14.** Stages of fabrication of the integrated near-field probe. (A) A pattern used for the photoconducting antenna on LT GaAs. (B) Lithography: bonding of the antenna and a sapphire substrate, polishing of GaAs, aperture masking, tip etching, and metal evaporation. (C) The schematic diagram of the probe. The contacts are opend at a side of the device by etching.

covered by the photoresist. GaAs is etched in a citric acid-based solution (50% citric acid:$H_2O_2$ - 5:2) [Moon *et al.*1998]. The etching rate is about 0.4 $\mu$m per minute at room temperature. After etching, only the metal contacts remain on the sapphire surface, bonded by the epoxy, since gold and epoxy are inactive to the citric acid–based solution. Finally, the probe is mounted on a chip carrier. Figure 4.15 shows an example of the packaged antenna. In the case of the near-field probe, the top surface is covered with the gold screen and the aperture is formed in the place of the lens.

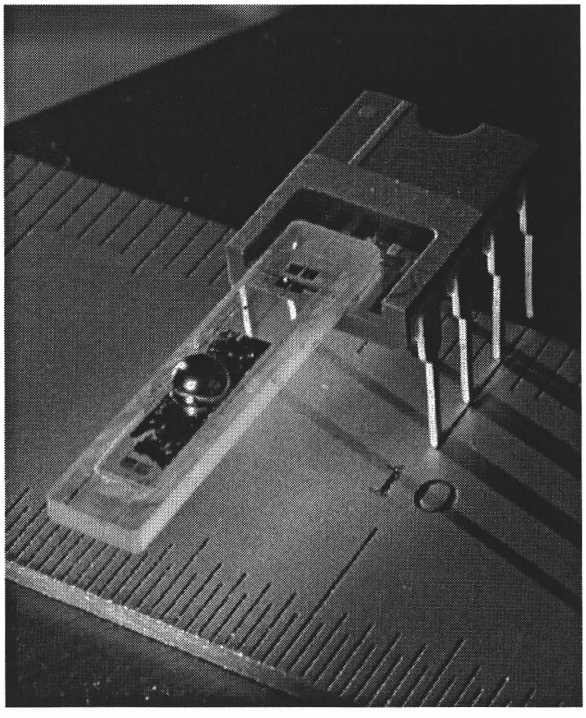

**Fig. 4. 15.** The packaged antenna on the sapphire substrate with a hyperhemispherical Si lens.

It is worth mentioning that the fabrication process is reproducible. The geometrical parameters – the aperture shape and size, the protruding tip, and the position of the antenna with respect to the aperture – are easily controlled. The process uses the conventional lithography techniques and requires standard clean-room facilities.

# CHAPTER 5

# TRANSMISSION OF TERAHERTZ PULSES THROUGH SUBWAVELENGTH APERTURES

## 5.1 Introduction

Transmission of single-cycle THz pulses through a subwavelength aperture is a central problem in THz near-field imaging. The electric field amplitude decay in the near zone of the aperture has already been discussed in Chapter 4. It was demonstrated that the sensitivity of the near-field probe significantly improves if a detecting element is placed in the near-field zone of the probe aperture. Another issue, which leads to a practical limit of spatial resolution with the aperture-type probe, is the throughput of a small aperture ($d<\lambda/100$). It is also important to know how the aperture alters the spectral content and temporal characteristics of the pulse. Diffraction of the broad band pulses on small objects results in significant changes in the pulse waveforms [Nahata & Heinz 1996, Bromage *et al.* 1998]. Understanding of the transmission process and the related effects helps to interpret images constructed using a subwavelength aperture.

The effects of the aperture size on transmission of THz pulse are discussed in this chapter. These effects are studied experimentally using the THz-TDS and a collection of subwavelength apertures of different sizes. The THz-TDS system allows characterization of the singe-cycle THz pulse deformation as a result of transmission process. Fourier analysis allows extracting the frequency dependent transmission coefficient and the phase information. Measuring the transmitted pulse in the near-zone of the aperture improves sensitivity and, therefore, apertures as small as $\lambda/300$ can be experimentally studied.

The transmission process alters the pulse temporal waveform and spectrum, resulting in pulse broadening and compression, time advancing, and spectrum blue-shift.

The Bethe's theory of transmission through small apertures [Bethe 1944] is combined with the classical waveguide theory for the analysis of the THz pulse propagation through the probe aperture. The waveguide model takes into account the physical thickness of the aperture screen.

## 5.2. Method

Transmission of the THz pulses through subwavelength apertures can be studied in a setup similar to the near-field imaging setup, described in previous chapters. A schematic diagram is shown in Figure 5.1. The electric field of pulses transmitted through subwavelength apertures is measured in the near-field zone of the aperture by a photoconducting antenna placed in point *O*, at a short distance from the aperture. Attenuation of the signal amplitude in this case is not as severe as in the case of the far-

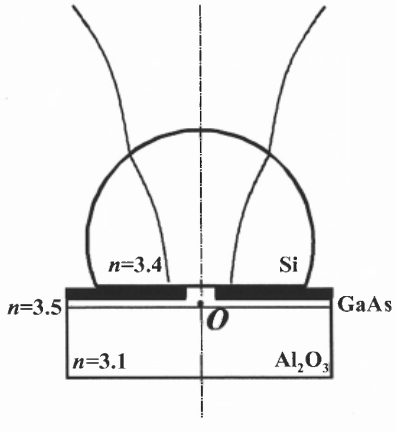


**Fig. 5.1.** A schematic diagram of the experimetal setup for measurements of THz pulses transmitted through small apertures. The detecting antenna is located at point *O* at a distance of 4 $\mu$m from the aperture plane.

field detection. In addition, the aperture is surrounded by high refractive index materials, which reduce the wavelength of the incident radiation. For example, transmission coefficient is ~$10^{-4}$ for the effective aperture size nd=$\lambda$/300.

In the experimental setup, the THz pulses are generated by a transient current in a photoconducting antenna. THz radiation is collected and focused on a square-shape aperture by a system of parabolic mirrors and Si lenses. The aperture is lithographically formed in a 600 nm thick gold screen on GaAs surface. A small cone on the surface fills the volume inside the aperture with GaAs. A 4 $\mu$m layer of GaAs separates the aperture from a detecting photoconducting antenna. Apertures with different sizes ranging from $d$=5 $\mu$m to $d$=50 $\mu$m ($d$ is the square side) were investigated.

The cutoff frequency of a square aperture ($TE_{01}$) surrounded by a dielectric with refractive index $n$ is related to the aperture size $d$ [Jackson 1962]:

$$\nu_c = \frac{c}{2dn}. \qquad (5.1)$$

Spectral components above the cutoff frequency propagate through the aperture, while the components below the cutoff suffer extensive attenuation. Table 5.1 summarizes the cutoff frequencies for the tested apertures.

| Aperture size, $d$ ($\mu$m) | Cutoff frequency, $\nu_c$ (THz) |
|---|---|
| 50 | 0.86 |
| 30 | 1.43 |
| 20 | 2.14 |
| 10 | 4.29 |
| 5 | 8.57 |

**Table 5.1.** Cutoff frequencies for the square apertures with side $d$ calculated using Eq. 5.1. Refractive index of the medium $n$=3.6.

The central frequency of the incident THz pulses (0.5 THz) is below the cutoff frequency for all the apertures. However, the high frequency tail of the pulse spectrum extends above $\nu_c$ and, therefore, suffers little attenuation. The amplitude of the spectral components above $\nu_c$ can become larger than amplitude of the suppressed central frequency. In this case, a large deformation of the temporal and spectral characteristics is expected. Figure 5.2 shows the waveform and the spectrum of the incident pulse. The cutoff frequency of the largest aperture ($d$=50 $\mu$m) lies within the measured spectrum of

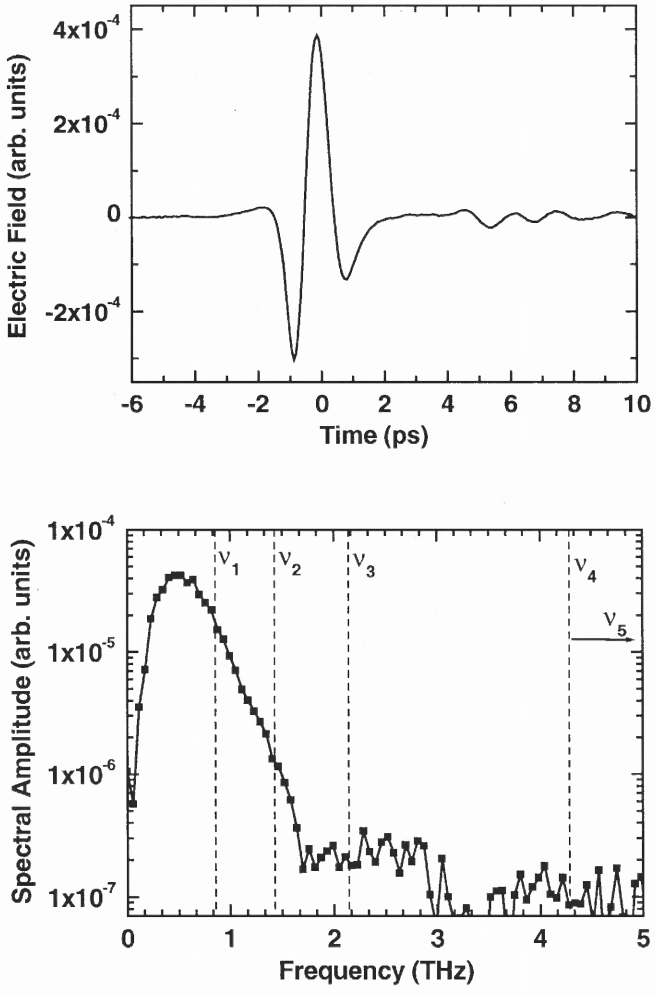


**Fig. 5.2.** The waveform and the spectrum of the incident THz pulses. The vertical dashed lines in (b) indicate the cutoff frequency for different aperture sizes.

the incident pulse. The cutoff of the apertures $d$<20 $\mu$m is significantly above the spectrum. Note, that in principle the high-frequency end of the incident pulse spectrum extends to infinity with decreasing amplitude. In Figure 5.2, the spectral components above 2 THz are not resolvable due to instrument noise.

The time domain waveform of the transmitted THz pulse was measured for every aperture. The incident THz pulse is measured using a similar setup without the gold screen in front of the detecting antenna. Applying Fourier analysis we can extract transmission coefficient and phase shift at all the measured frequencies.

The frequency dependent transmission coefficient and the phase shift for an aperture of size $d$ is defined as follows

$$T(\omega,d)=\frac{E(\omega,d)}{E_0(\omega)}, \tag{5.2}$$

$$\Delta\varphi(\omega,d)=\varphi(\omega,d)-\varphi_0(\omega), \tag{5.3}$$

where $E_0(\omega)$ and $\varphi_0(\omega)$ is the spectral amplitude and the phase of the measured incident pulse. Attenuation of the THz pulses, the transmission coefficient and the phase shift, as well as deformation of the pulse waveform and spectrum are discussed in the following sections.

## 5.3 Transmission of THz Pulses

### 5.3.1 Attenuation of THz Pulses

An essential question of the aperture-type near-field probes is the reduction of power coupled into the aperture as $d$ decreases. The theory of transmission through small apertures in the infinitely thin screen predicts the $d^3$-law for the electric field amplitude

in the limit of $\lambda >> d$ [Bethe 1944, Bouwkamp 1950]. However, thickness of the screen has to be taken into account for a physical aperture.

The aperture is approximated with an undersized waveguide model. The eigenvalue equation for the lowest $TE_{10}$ mode of a rectangular waveguide with cross section $d \times d$ filled with dielectric material $n$

$$k^2 = \left(\frac{2\pi n}{\lambda}\right)^2 - \left(\frac{\pi}{d}\right)^2 = \frac{4\pi^2 n^2 (\nu^2 - \nu_c^{\,2})}{c^2}, \tag{5.4}$$

where the cutoff frequency is defined in Eq. 5.1. If the condition $\lambda < 2dn$ holds for the vacuum wavelength, the wavevector is imaginary and there is no propagating solution inside the waveguide. The wave amplitude exponentially decreases with the waveguide length

$$E(l) = E(0)\exp(ikl) = E(0)\exp\left(-\frac{\pi l}{\lambda d}\sqrt{\lambda^2 - 4n^2 d^2}\right). \tag{5.5}$$

The exponent is almost unity for relatively large apertures ($d >> l$), for which the metallic screen can be assumed infinitely thin. The effect becomes significant when $d$ becomes comparable to $l$. In this limit ($nd << \lambda$), the exponential term conveniently reduces to $\exp\left(-\frac{\pi l}{d}\right)$, where $l$ is the screen thickness. A simple wavelength independent expression for the transmission through a small physical aperture is therefore

$$E(d,l) = T \cdot E_0 d^3 \exp\left(-\frac{\pi l}{d}\right). \tag{5.6}$$

The transmission coefficient calculated using this model is shown in Figure 5.3. The wavelength dependence is implicitly included in a scaling factor $T$, which is found comparing the curve to the measured RMS value of electric field of the transmitted THz

pulses. The model partly explains the sub $d^3$-law at small $d$. In addition, for the 5 $\mu$m aperture the distance between the aperture and antenna becomes larger than the characteristic length of the near-field zone $d/2$. Outside of this zone, the amplitude of the electric field is smaller [Chapter 4]. The RMS value of the electric field of the pulse is used in order to exclude the effects of the pulse distortion, which usually affects the peak to peak value shown in the figure in open squares for comparison.

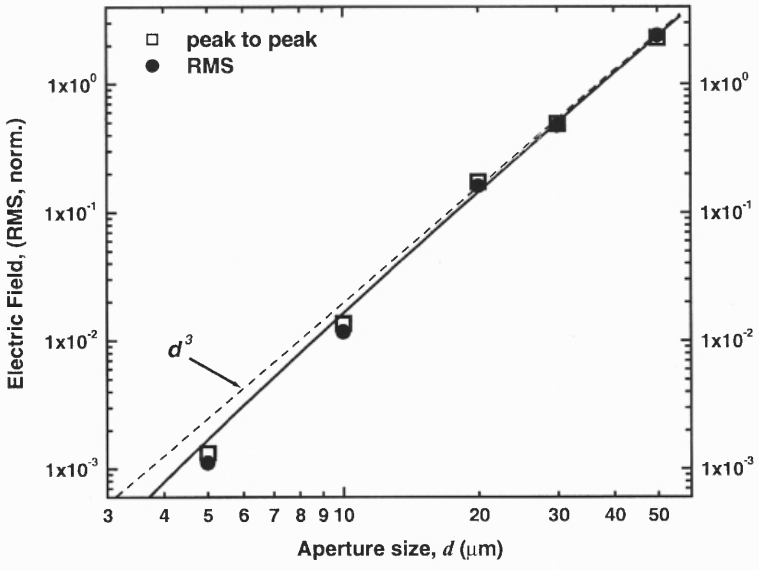


**Fig. 5.3.** Reduction of the peak-to-peak amplitude (open squares) and the RMS value $\left[\sqrt{\int E^2(t)dt}\right]$ (circles) of the THz pulse field with the aperture size. The solid curve shows the $d^3$-law with the finite screen thickness correction.

Note that Eq. 5.6 does not contain the refractive index of the medium inside the aperture. In this limiting case, the exponential attenuation factor depends only on the ratio of geometrical parameters $l$ and $\lambda$. However, the refractive index as well as the wavelength implicitly enters factor $T$, and coupling through the aperture is better for smaller effective wavelength $\lambda/n$.

### 5.3.2 Temporal and Spectral Deformation

Temporal deformation of THz pulses is directly measured in theTHz-TDS setup. The time domain waveforms of the THz pulse transmitted through apertures of different sizes are shown in Figure 5.4. The temporal characteristic of the incident pulse changes as result of diffraction on a small aperture. The deformation is related to the high-pass properties of subwavelength apertures.

Spectral components above the cutoff propagate through the aperture without significant change in amplitude, while the rest of the spectrum experiences the frequency dependent attenuation. For the 50 $\mu$m aperture, this process results in a severe pulse deformation: the duration extends to ~5 ps, and the spectrum becomes narrow and shifted to higher frequencies [Fig. 5.4(b)]. As the aperture size decreases and the cutoff frequency moves further from the pulse spectrum, the variation of the transmission coefficient with frequency reduces. Suppression of the red end of the spectrum reveals amplitudes above 1.5 THz, which are not resolved in the incident spectrum due to the instrument noise [Fig. 5.4(a)]. This effectively increase the bandwidth of the pulse transmitted through the 5 $\mu$m aperture. The pulse maintains its single-cycle characteristic and shows faster electric field oscillation than the incident pulse [Fig. 5.4(f)].

Besides the frequency dependent attenuation, the aperture also imposes a phase delay on the transmitted wave. The phase shift that the wave experiences as it passes through the aperture, in general, consists of two parts: the phase shift associated with the wave coupling in and out of the aperture $\Delta\varphi_C$, and the phase delay due to the waveguide $\Delta\varphi_{WG}$.

$$E(\omega) = T(\omega)E_0(\omega)\exp(-i\omega t - \Delta\varphi),$$
$$\Delta\varphi = \Delta\varphi_C + \Delta\varphi_{WG}. \tag{5.7}$$

The corresponding time shift due to the waveguide is negligible since the screen thickness is small (0.6 $\mu$m) and the accumulated time delay is ~10 fs for propagating waves. The evanescent waves tunnel through the waveguide and do not experience any delay inside the waveguide.

$$\Delta\tau_{WG}(\omega) = \begin{cases} \dfrac{n_{eff}(\omega)-1}{c} l << \dfrac{1}{\omega}, & \omega > \omega_c \\ 0, & \omega < \omega_c \end{cases} \tag{5.8}$$

Therefore, the experimentally measured phase shift is attributed to the aperture coupling. Figure 5.5(b) shows the time shift as a function of frequency measured for all apertures. Experimental data shows clearly that spectral components with frequency larger than the cutoff frequency propagate through the aperture without any delay. Below the cutoff, however, there is a negative time delay, which corresponds to time advancing of waves through a subwavelength aperture. The THz pulse incident on the 5 $\mu$m aperture appears on the other side ~0.7 ps earlier [Fig. 5.4(f)].

A possible explanation to this phenomenon is the 'chirp' of the incident pulse (asymmetric waveform). The electric field in the front of the THz pulse varies faster in time than at the pulse end. Given that higher frequencies suffer lower attenuation, the leading part of the pulse is preferentially transmitted through the aperture while the slower varying tail of the pulse is suppressed. Note, that the amplitude of the transmitted pulse is ~$10^{-4}$ of the incident pulse amplitude.

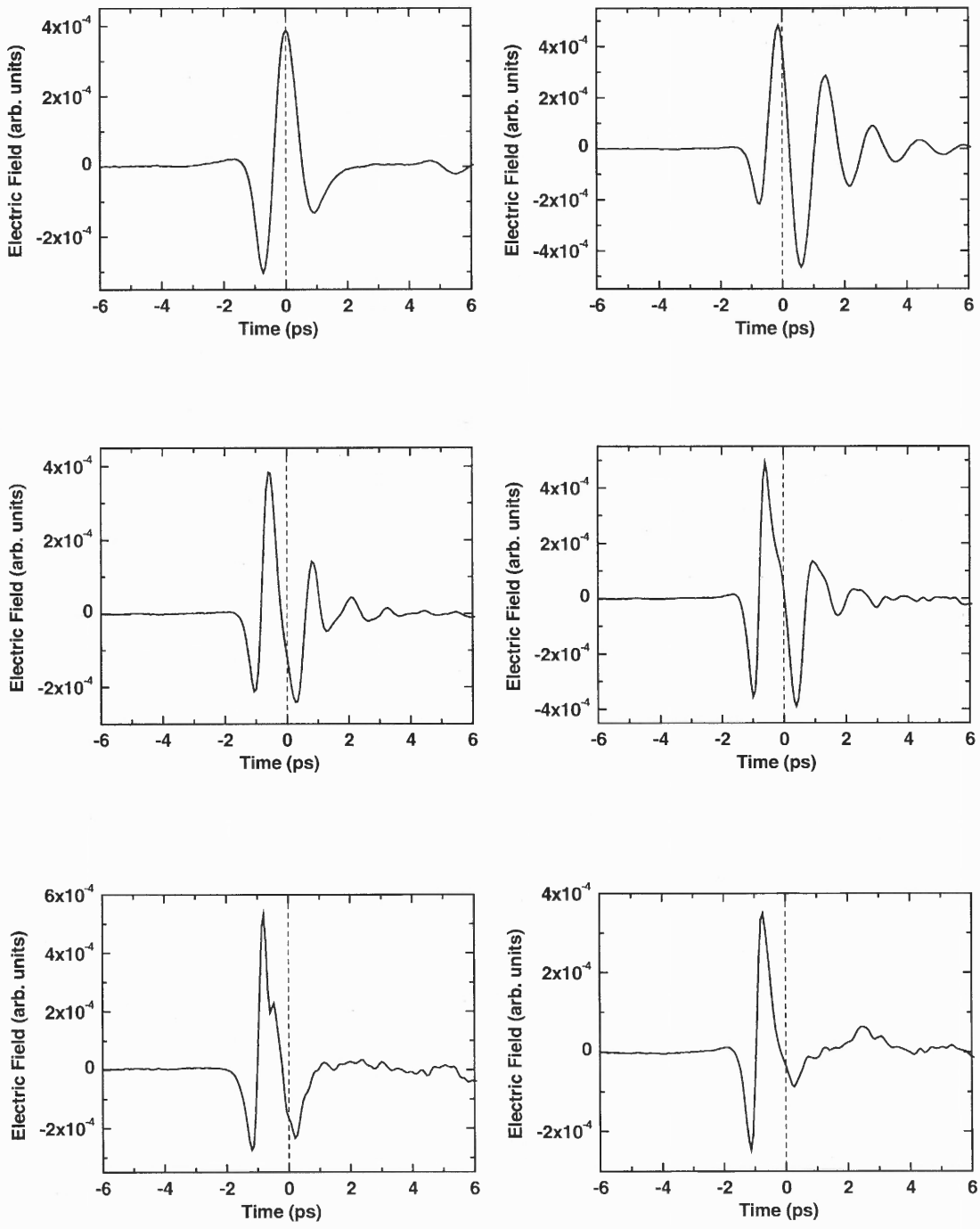


**Fig. 5.4.** Waveforms of the incident pulse (a) and the pulses transmitted through the apertures: $d$=50$\mu$m (b), 30$\mu$m (c), 20$\mu$m (d), 10$\mu$m (e), 5$\mu$m (f).

Temporal advance of the peak of the THz pulse transmitted through a subwavelength aperture has been reported before [Wynne *et al.* 2000]. However, this effect was observed on strongly deformed pulses, and the center of gravity of the pulse,

$$t_c = \frac{\int tE^2(t)dt}{\int E^2(t)dt}, \tag{5.9}$$

had positive delay in these experiments. Our observation with 5 $\mu$m and 10 $\mu$m apertures demonstrates that the center of gravity of the THz pulse can also experience the temporal advance in the transmission process. The conditions required to observe this effect are summarized below:

(1) the pulse waveform is asymmetric with faster varying temporal characteristic in front of the pulse;

(2) the transmission coefficient increases with frequency.

(3) the spectral amplitudes of the pulse above the cutoff is vanishing;

The first two are the conditions of the preferential transmission of the front of the pulse. The third one ensures that all the spectral components are in the evanescent modes and the pulse does not experience significant dispersion, which is particularly strong near the cutoff frequency. Consequently, the pulse waveform stays compressed.

The third condition is not satisfied, for example, in the case of the THz pulses generated by a ZnTe crystal and transmitted through the 10 $\mu$m aperture. Substantial amplitude of the components at the cutoff frequency results in deformation of the pulse waveform similar to the case presented in Figure 5.4(b). The spectrum of the incident pulse contains above the cutoff components, for which the time delay is positive. Since the amplitude of these components almost does not decrease in the transmission process,

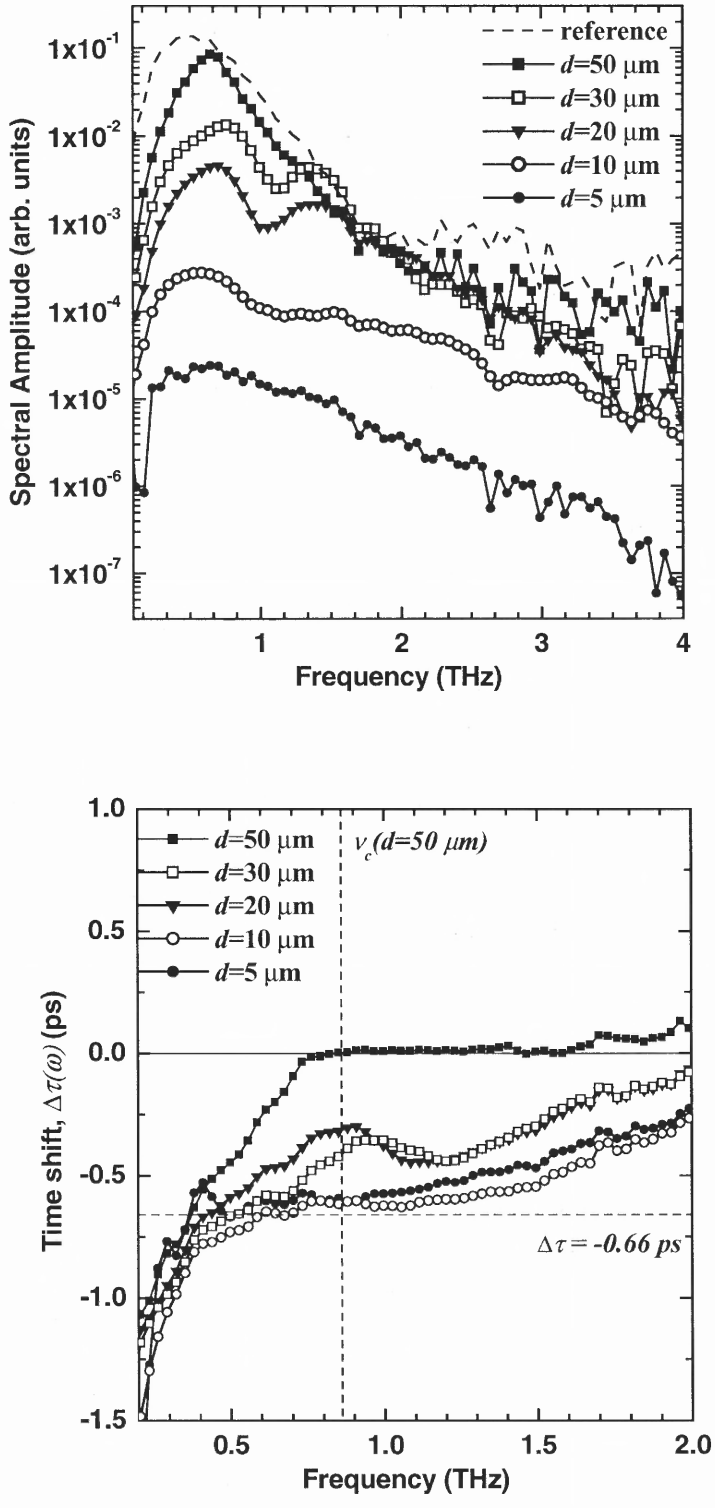


**Fig. 5.5.** Spectral content of the radiation transmitted through the small apertures (a), and the frequency dependent time shift (b). The dashed horizontal line shows the time shift of –0.66 ps, found for the center of gravity of the pulse transmitted through the 5 $\mu$m aperture.

the measured electric field mostly consists of the high frequency part of the incident spectrum, and the time advance of the pulse is not observed.

## 5.4 Spatial Resolution Limit

The metallic film on the surface of the probe screens the antenna from the incident field and allows electromagnetic wave to propagate only through the aperture. The film thickness has to be sufficient to attenuate the undiffracted wave to a level below the noise. However, the thicker the screen, the stronger the attenuation of the wave, which tunnels through the aperture. The wave attenuation inside the metallic film and attenuation in the aperture need to be balanced in order to optimize signal to noise ratio and achieve the best probe performance. In the previous section, dependence of the transmitted wave amplitude on thickness of the screen and the aperture size was discussed. Here, the analysis of the THz pulses attenuation by a metallic film is given.

### 5.4.1 Theoretical Consideration of Attenuation of THz Pulses by a Metallic Film.

A wave incident on the metallic film suffers reflections from the film interfaces and a progressive attenuation as it propagates through the film. In the assumption that frequency of the incident field is smaller than the plasma frequency of the metal, the electric field $E$ satisfies the wave equation inside the metal

$$\nabla^2 E = \frac{\mu\varepsilon}{c^2}\frac{\partial^2 E}{\partial t^2} + \frac{4\pi\mu\sigma}{c^2}\frac{\partial E}{dt}, \tag{5.10}$$

where $\sigma$ is the electrical conductivity of the metal. The last term implies that the wave is damped. In the monochromatic approximation, this equation can be written as

$$\nabla^2 E + k^2 E = 0, \tag{5.11}$$

where

$$k^2 = \frac{\omega^2 \mu}{c^2}\left(\varepsilon + i\frac{4\pi\sigma}{\omega}\right) = \left(\frac{\omega}{c}\cdot n(1+i\kappa)\right)^2. \tag{5.12}$$

$n$ and $\kappa$ are real and imaginary parts of the refractive index of the metal $\hat{n} = n(1+i\kappa)$.

The formal solution to the equation is a plane time-harmonic wave with a complex wave number $k$

$$E = E_0 \exp(ikz - i\omega t) = E_0 \exp(i\frac{\omega}{c}nz - i\omega t)\cdot \exp(-\frac{\omega}{c}n\kappa z). \tag{5.13}$$

Attenuation is given by the exponential term with imaginary part of the refractive index. The quantities $n$ and $\kappa$ can be expressed in terms of the material constants

$$n^2(1-\kappa^2) = \mu\varepsilon, \tag{5.14}$$

$$n^2\kappa = \frac{2\pi\mu\sigma}{\omega}. \tag{5.15}$$

The dielectric constant and the conductivity of gold, in general, depend on the frequency of the external field. However, these parameters can be approximated by their static value at THz frequencies. The plasma frequency of gold is approximately 2-3 orders higher than frequency of the THz field. Therefore, the product $\omega\tau$, where $\tau$ is relaxation time, is much smaller than unity, and the conductivity reduces to

$$\sigma = \frac{Ne^2\tau}{m(1-i\omega\tau)} \cong \frac{Ne^2\tau}{m}. \tag{5.16}$$

The dielectric constant in Eq. 5.10 represents the contribution from the bound electrons, which is small, compared to the contribution from the free electrons. As the mechanism of electric polarization in metals is not fundamentally different from that of a

dielectric, it may be assumed that $\varepsilon$ is of the same order of magnitude. Hence, provided $n\kappa$ is large, one can deduce from Eq. 5.12 and Eq. 5.13

$$n \sim n\kappa = \sqrt{\frac{2\pi\mu\sigma}{\omega}}. \tag{5.17}$$

Under these assumptions the attenuation term in Eq. 5.4 becomes

$$\exp(-\frac{\omega}{c} n\kappa z) = \exp\left(-\frac{\omega}{c}\sqrt{\frac{2\pi\mu\sigma}{\omega}} z\right). \tag{5.18}$$

The decay of the electric field amplitude inside the metal can be expressed in terms of the absorption coefficient $\alpha$, or the penetration depth $\delta=\alpha^{-1}$

$$E(z) = E_0 \exp(-\alpha z) = E_0 \exp(-\frac{z}{\delta}), \tag{5.19}$$

where

$$\alpha = \frac{\sqrt{2\pi\mu\sigma\omega}}{c}, \tag{5.20}$$

and

$$\delta = \frac{c}{\sqrt{2\pi\mu\sigma\omega}} \quad \text{(esu)} \qquad \delta = \sqrt{\frac{2}{\mu\omega\sigma}} \quad \text{(SI)} \tag{5.21}$$

Figure 5.6 shows the calculated refractive index and penetration depth for gold ($\sigma_{Au}$=5.8 $\cdot 10^5$ $cm^{-1}Ohm^{-1}$). Note that the penetration depth varies as the square root of the incident wavelength.

Losses due to reflections from the metallic film interfaces need to be included in order to calculate the total attenuation. The transmission coefficient of the metallic film can be calculated according to the formula of transmission through thin films [Born & Wolf 1999].

$$t = \tau e^{i\chi} = \frac{t_{12}t_{23}e^{i\beta}}{1 + r_{12}r_{23}e^{2i\beta}}, \tag{5.22}$$

where for the case of normal incidence

$$\beta = \frac{2\pi}{\lambda_0}\hat{n}_2 l, \tag{5.23}$$

$t_{ij}$ and $r_{ij}$ are the transmission and reflection coefficients for the interfaces *i-j*

$$t_{ij} = \frac{2n_i}{n_i + n_j}, \qquad r_{ij} = \frac{n_i - n_j}{n_i + n_j}. \tag{5.24}$$

For transmission and reflection at the surface of the metallic film we have

$$t_{12} = \tau_{12}e^{i\chi_{12}} = \frac{2n_1 e^{i\chi_{12}}}{\sqrt{(n_1 + n_2)^2 + (n_2\kappa)^2}}, \tag{5.25.a}$$

$$\tan\chi_{12} = -\frac{n_2\kappa}{n_1 + n_2}, \tag{5.25.b}$$

$$r_{12} = \rho_{12}e^{i\phi_{12}} = \frac{\sqrt{(n_1 - n_2)^2 + (n_2\kappa)^2}\,e^{i\phi_{12}}}{\sqrt{(n_1 + n_2)^2 + (n_2\kappa)^2}}, \tag{5.26.a}$$

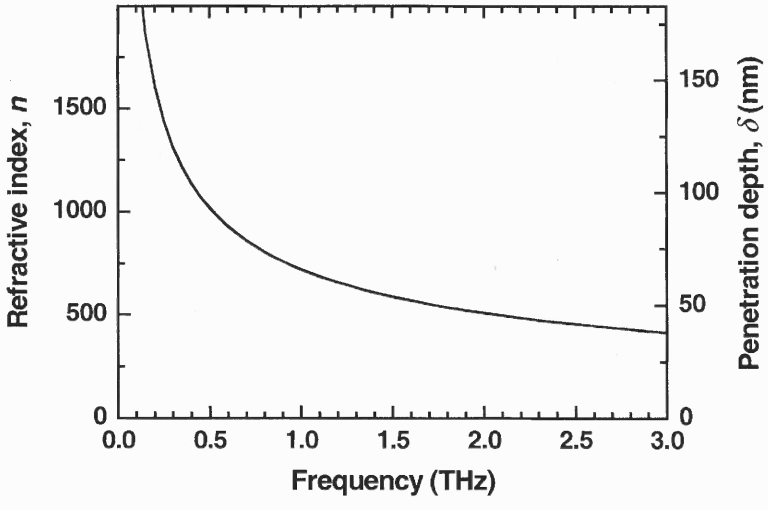


**Fig. 5.6.** Calculated refractive index and penetration depth for gold. The conductivity of gold is assumed to be equal to its dc value.

$$\tan\phi_{12} = \frac{2n_1 n_2 \kappa}{n_2^{\,2} + n_2^{\,2}\kappa^2 - n_1^{\,2}}. \qquad (5.26.b)$$

The reflection and transmission coefficients at the second interface (metal-dielectric) are found in analogous way:

$$t_{23} = \tau_{23} e^{i\chi_{23}} = \frac{2\sqrt{n_2^{\,2} + (n_2\kappa)^2}\, e^{i\chi_{23}}}{\sqrt{(n_3 + n_2)^2 + (n_2\kappa)^2}}, \qquad (5.27.a)$$

$$\tan\chi_{23} = \frac{n_2\kappa n_3}{n_2^{\,2} + (n_2\kappa)^2 + n_2 n_3}, \qquad (5.27.b)$$

$$r_{23} = \rho_{23} e^{i\phi_{23}} = \frac{\sqrt{(n_3 - n_2)^2 + (n_2\kappa)^2}\, e^{i\phi_{23}}}{\sqrt{(n_3 + n_2)^2 + (n_2\kappa)^2}}, \qquad (5.28.a)$$

$$\tan\phi_{23} = \frac{2n_3 n_2 \kappa}{n_2^{\,2} + (n_2\kappa)^2 - n_3^{\,2}}. \qquad (5.28.b)$$

Substituting expressions for the transmission and reflection coefficients [Eq. 5.25-5.28] into Eq. 5.22, the total transmission is obtained

$$\tau = \sqrt{\frac{\tau_{12}^{\,2}\tau_{23}^{\,2} e^{-2\,\mathrm{Im}(\beta)}}{1 + \rho_{12}^{\,2}\rho_{23}^{\,2} e^{-4\,\mathrm{Im}(\beta)} + 2\rho_{12}\rho_{23} e^{-2\,\mathrm{Im}(\beta)} \cos(\phi_{12} + \phi_{23} + 2\,\mathrm{Re}(\beta))}}. \qquad (5.29)$$

Figure 5.7 shows the calculated attenuation of a wave of frequency 0.5 THz for a gold film on surface of GaAs ($n$=3.6). If thickness of the gold film exceeds a value of 150 nm, the attenuation inside the film is so strong that the effect of multiple beam interference is negligible. The expression for the amplitude of the transmission coefficient then reduces to a simple form

$$\tau = \tau_{12}\tau_{23} \exp(-\frac{\omega}{c} n_2 \kappa l) = \tau_{12}\tau_{23} \exp(-\frac{l}{\delta}). \qquad (5.30)$$

[The corresponding formula in Born & Wolf 1999 carries a wrong factor of two in the exponent].

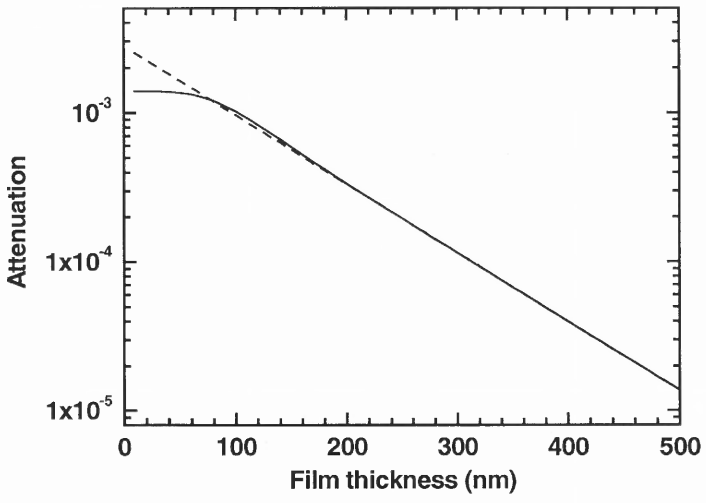


**Fig. 5.7.** Attenuation of a monochromatic wave $\nu$=0.5 THz by the gold film on surface of GaAs ($n$=3.6). Solid curve includes the multiple beam interference effect. The thick film approximation is shown by the dashed line.

The transmission coefficient found using Eq. 5.30 asymptotically approaches the exact curve at $l$>150 nm. For sufficiently thick metallic films, the effect of multiple interference vanishes, since the amplitude of the reflections is negligibly small due to damping in the metal. THz pulses contain a broad band of frequencies, for which the parameters in Eq.5.30 change. Given the fact that variation of the refractive index of GaAs $\left(\frac{\Delta n}{n}\right)$ is only 0.25% in the interval between 0.25 THz and 1.5 THz [Grischkowsky *et al.* 1990], transmission coefficients $\tau_{12}$ and $\tau_{23}$ are essentially constants in this frequency range. The penetration depth is expected to vary as a square root of the frequency from ~120 nm at 0.25 THz to ~50 nm at 1.5 THz. However, as discussed in the next section, the

experimentally measured penetration depth remained ~50 nm throughout this interval of frequencies.

### 5.4.2 Experimental Results on Attenuation by a Metallic Film.

The measured transmission coefficient is slightly different from the theoretical estimations. As discussed, the total attenuation includes losses at the interfaces and damping inside the metallic film. Their respective contribution can be distinguished in a set of transmission measurements involving metallic films with different thickness.

In a general case of a thick ($l>>\delta$) gold film on a dielectric substrate, the transmitted amplitude can be expressed as follows

$$E_t(\omega) = E_0(\omega)\tau_{12}\tau_{23}e^{-\frac{l}{\delta(\omega)}}A_{Stub}(\omega), \qquad (5.31)$$

where $A_{sub}$ is an attenuation factor that includes absorption of the wave in the substrate and losses at the substrate-air interface. The metallic film interface contribution is eliminated by comparing transmission coefficients for samples with different film thickness $l$. The damping inside the film due to additional thickness $\Delta l$ equals to the ratio of the measured amplitudes for the films with lengths $l$ and $l+\Delta l$. Furthermore, the penetration depth $\delta(\omega)$ is directly obtained by taking the logarithm of the ratio of the transmitted fields

$$\delta(\omega) = \frac{l_2 - l_1}{\ln\left(\frac{E_t(\omega, l_1)}{E_t(\omega, l_2)}\right)}. \qquad (5.32)$$

Transmission through Au films with thickness of 100 nm, 150 nm, and 180 nm was measured in order to characterize the penetration depth of Au. The films were

deposited on a GaAs substrate. The pulse amplitude exponentially decreases with the film thickness as expected, however, the rate is more rapid than predicted by the theory.

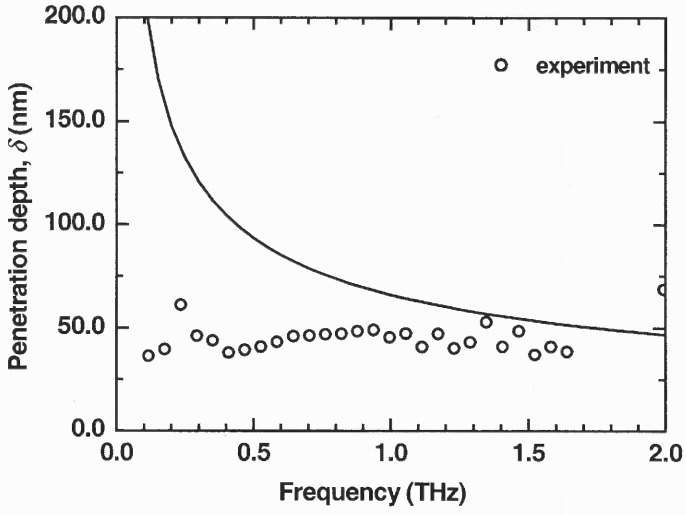


**Fig. 5.8.** The experimentally measured and calculated penetration depths of gold at THz frequencies.

Figure 5.8 shows the penetration depth of Au found experimentally using expression Eq. 5.32. Note that $\delta$ does not follow the theoretical square root frequency dependence, but rather maintains a constant value of $\delta$= ~45-50 nm over the range of 0.2-1.5 THz. In this respect, it is important to mention that at sufficiently high frequencies the theoretical penetration depth becomes comparable to the mean free path, which is ~30 nm for Au. In this case, the homogeneous field approximation ($j=\sigma E$) breaks, leading to the anomalous skin effect.

The transmission coefficients at the interfaces can also be measured by comparing transmission through the film with transmission of the plane substrate. The ratio of the amplitudes in this case is

$$\frac{E_M(\omega)}{E_{Sub}(\omega)} = \tau_{12}\tau_{23}e^{\frac{l}{\delta(\omega)}}\frac{(1+n_{Sub})}{2}. \tag{5.33}$$

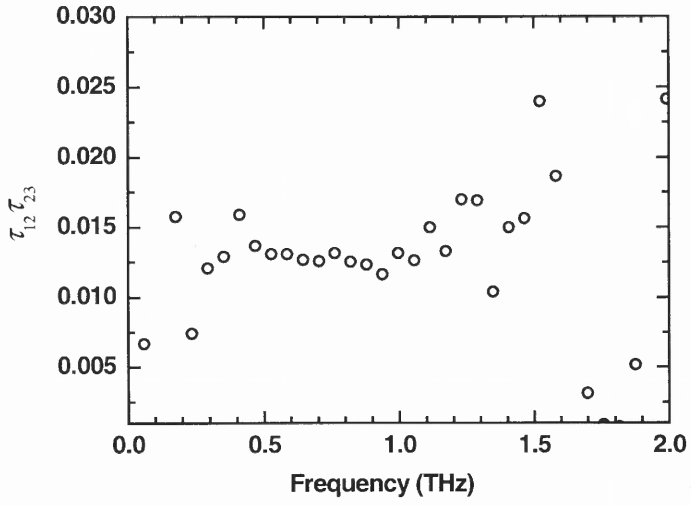


**Fig. 5.9.** The experimentally measured interface transmission coefficients of the gold film.

Using the experimentally found penetration depth function, the product of the interface transmission coefficients $\tau_{12}\tau_{23}$ can be found. The result is presented in Figure 5.9. The measured transmission coefficients and the penetration depth of gold can be used to estimate attenuation of the THz pulses for a larger film thickness.

### 5.4.3 Spatial Resolution Limit

As the size of the aperture in the near-field probe decreases, the amplitude of the detected field decreases as well. In order to maintain the signal at a higher level than the background field, which is due to the wave penetration through the aperture screen, the thickness of the screen needs to be increased. On the other hand, an additional thickness results in higher attenuation of the aperture field. The amplitudes of the signal and the

background can be related through the geometrical parameters of the aperture. Consequently, the spatial resolution of the near-field probe, which is equal to the aperture size, can be related to the required metal screen thickness and the expected attenuation.

Amplitudes of the signal and the background can be expressed as

$$E_S = E_0 t_S d^3 e^{-\frac{\pi l}{d}}, \tag{5.34}$$

$$E_B = E_0 t_B e^{-\frac{l}{\delta}}, \tag{5.35}$$

where $t_S$ and $t_B$ are the experimentally determined constants. Both expressions contain terms that exponentially decrease with $l$. In principle, for any $d$, such that $d>\pi\delta$, there is $l$, for which $E_S>E_B$. Solving equation $E_S=E_B$ for $l$ with $d$ as a parameter, the minimal thickness of the screen required to attenuate the incident THz pulse to the level of the amplitude of the pulse transmitted through the aperture, can be found. The dashed curve in Figure 5.10(a) shows the solution. The required thickness exponentially increases as the aperture size decreases. The solid curve shows a practical thickness when the signal

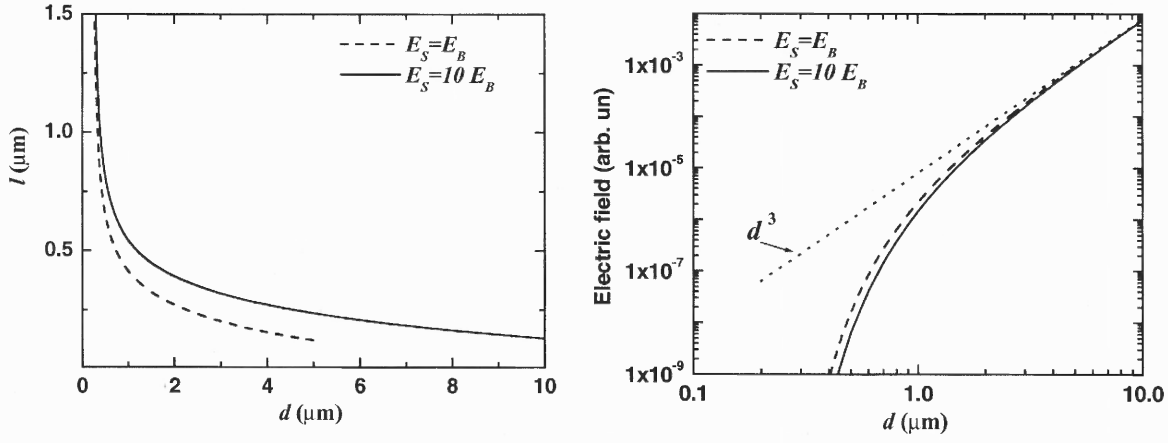


**Fig. 5.10.** Condition for the thickness of the aperture screen (a), and attenuation of electric field corresponding to the aperture size $d$ (b).

amplitude is 10 times larger than the background. The corresponding attenuation curves are shown in Figure 5.10(b).

The practical limit of spatial resolution is determined by the available intensity of the source. The near-field probe with the aperture size $d$~1 $\mu$m is expected to suffer ~$10^{-6}$ attenuation in electric field. As $d$ approaches the value of a few penetration depths, which is ~50 nm at THz regime, the aperture fails to confine the electromagnetic fields due to penetration into walls and our considerations become invalid.

The smallest aperture realized in the THz near-field probe was a 5 $\mu$m square aperture. The signal to noise ratio in this case was ~30 for the peak of the pulse. In principle, a probe with 2-3 $\mu$m can be realized with the same experimental conditions and the signal to noise ratio of ~3. Further improvement of resolution requires a larger power in the THz source, which the photoconducting antenna is unable to generate. Figure 5.10 (b) suggests that spatial resolution of ~1 $\mu$m can be achieved.

# CHAPTER 6

# NEAR-FIELD PROBE PERFORMANCE

## 6.1 Introduction

Any optical system has to be characterized in order to interpret images meaningfully. It is especially important for complicated imaging systems such as the THz near-field scanning microscope. The question of THz pulse propagation through small apertures was discussed in Chapters 4 and 5. A general conclusion states that the pulse waveform and the spectrum experience transformations due to the aperture. Characterization of the probe performance involves a more complicated problem of the THz pulse coupling through the aperture in the presence of objects. In addition, the object itself perturbs electric field of the pulse. In collection mode arrangement, when the object is illuminated uniformly, electric field distribution in the image plane is determined not only by the local optical constants, but by the whole object. The image rather represents the electric field in the object plane.

The problem of near-field image formation is being discussed in the literature. Due to the complexity of the near-field interaction and a variety of near-field microscope schemes, the problem is very broad and many numerical modes were proposed [Novotny *et al.* 1994, Barchiesi *et al.* 1996, Vasilyeva & Taflove 1998, Hochman *et al.* 2000]. The image of an object in the near-field depends greatly on illumination conditions [Girard 1998, Valle *et al.* 1999], polarization of the incident field [Bozhevolnyi *et al.* 1999], probe-sample arrangement and the separation between them [Pohl 1991], the object size,

shape and optical index [Martin et al. 1995]. In addition, in THz imaging, the instrument measures instantaneous electric field of the wave, which varies in time.

The image formation in near-field setups that use pulsed THz radiation is a relatively unexplored problem. Furthermore, the technique has not been applied extensively and there is not much of available experimental data. This chapter is devoted to discussion of the basic properties of near-field images, including spatial resolution, depth of field, and polarization sensitivity.

## 6.2 Image Quality – Spatial Resolution

Image quality is evaluated by the size of the smallest resolvable object feature. In the near-field imaging, the probe aperture selects the local electromagnetic fields in front of the probe, therefore the spatial resolution is defined by the aperture size. Due to diffraction of waves at the object, an image reproduces the object features only if the probe to object distance is very small. Unless this requirement is satisfied, diffraction effects smear the image and spatial resolution is determined by the distance to the object, rather than by the aperture size.

Various criteria are commonly used for evaluation of the image quality. The most common is the measure of how well the system can resolve a two-point object. However, an edge object is more practical and convenient to use for the THz microscope, and a thin metallic film edge is scanned in the resolution test. The choice of the edge object over the two-point object is justified by a relative simplicity of the amplitude function. The metallic film edge is of high contrast: when the film blocks the aperture, no light couples into the probe and the measured signal is zero (assuming that transmission through

metallic film is negligible), when the film clears the aperture, the probe measures the full pulse amplitude, if there were no film at all.

Resolution is experimentally determined by scanning the edge of a 600 nm thick gold film deposited on a transparent substrate (GaAs). The clear and opaque regions of the sample represent the two limits of detected signal: the full strength signal and complete absence of the signal (or background). The transition region with boundaries defined at a level of 10% and 90% of the full strength signal determines the spatial resolution. Levels of 20% and 80% are also used, especially if substantial noise prevents from an accurate measurement of resolution.

The imaging THz-TDS setup allows measurements of the pulse amplitude, as well as the amplitude and the phase of the spectral components as functions of spatial coordinates. Consider the pulse amplitude distribution. In this case, the variable time delay of the setup is fixed on the peak of the pulse [Fig. 6.1]. The amplitude of the signal

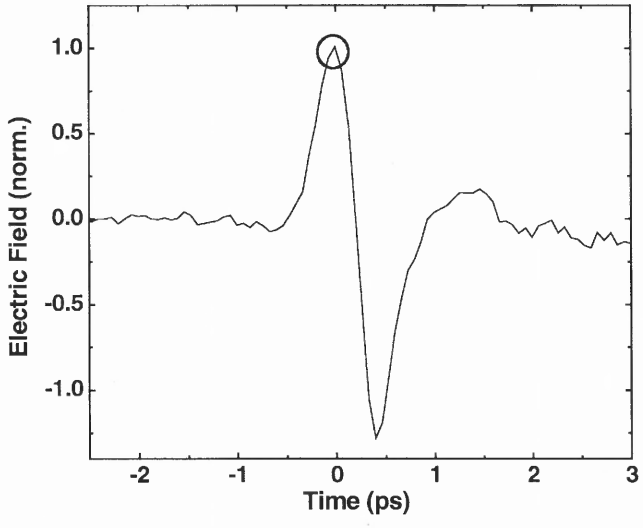


**Fig. 6.1**. The waveform of the pulse measured with the 5 $\mu$m aperture probe. The circle shows the time delay at which the resolution curve is measured.

reflects the amplitude of the THz pulse, provided that the waveform does not change. Figure 6.2 shows the amplitude distribution as a function of the spatial coordinate across the edge position measured using a probe with 5 $\mu$m aperture. The sample is scanned at a distance of 1-2 $\mu$m. The signal contrast is developed over a sample translation of 7 $\mu$m (10%-90%). The positive position corresponds to the metallic film in front of the aperture.

The fact that the spatial resolution is defined by the aperture size rather than the wavelength can be demonstrated by measuring the whole pulse waveform and performing Fourier transform for every position of the metallic edge. By doing this, the amplitude distributions are obtained for all the spectral components of the THz pulse. Fig. 6.3(a) shows selected edge profiles at different frequencies, measured using the 10 $\mu$m aperture probe. Identical resolution curves are obtained for a wide spectral window (0.2-2.5 THz), limited only be the noise level. Resolution tests performed on the near-field probes with

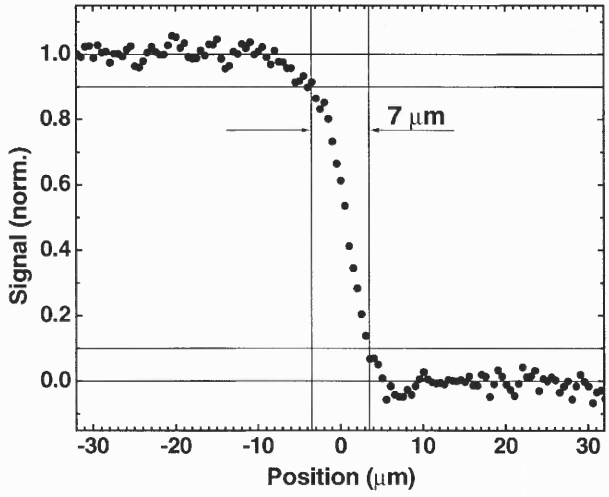


**Fig. 6.2.** Resolution edge test for the probe with $d$=5 $\mu$m and $L$=4 $\mu$m. The edge is oriented prallel to the polarization of the incident THz field.

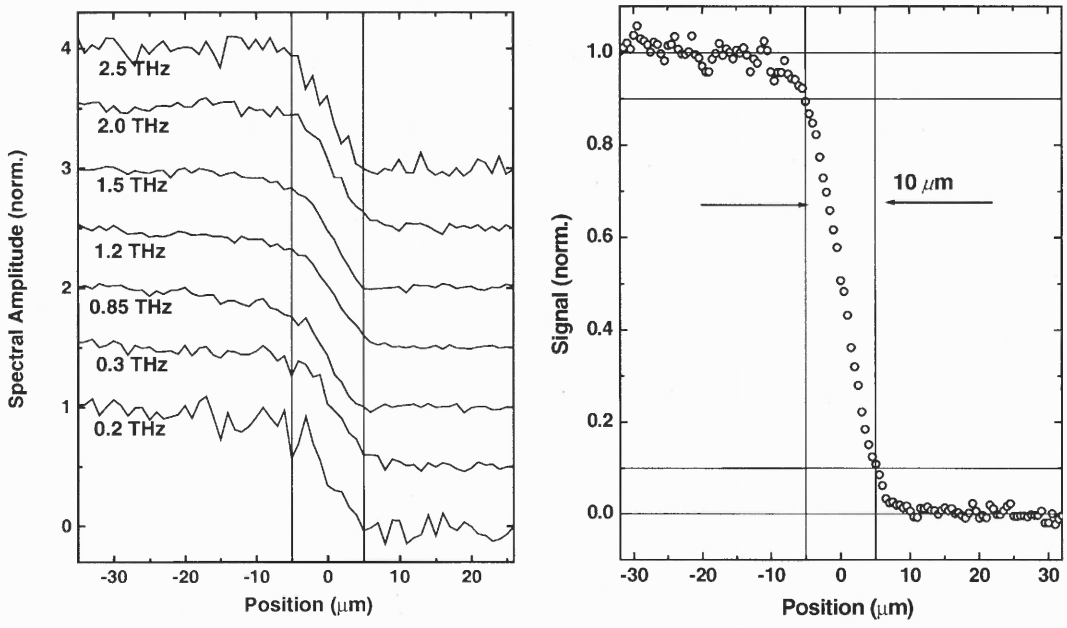


**Fig.6.3.** Resolution at different frequencies, measured by the 10 $\mu$m probe with L=7 $\mu$m (a). The edge is oriented parallel to the polarization of the incident THz field. (b) A similar resolution curve is measured for the peak pulse amplitude.

larger apertures (up to $d$=50 $\mu$m) showed that resolution always equals approximately to the aperture size. It must be mentioned that features smaller than the aperture size can create significant perturbation of the field and, hence, can be visible. Nevertheless, their shape does not reproduce correctly in the image.

## 6.3 Probe-Sample Separation

Near-field imaging provides high resolution only if the sample is placed close to the aperture, at a distance smaller than $d/3$. Samples are not necessarily flat and often the probe-sample separation varies during the scan. It is essential to have an understanding of the signal variation due to the changing probe-sample gap.

### 6.3.1 Approach Curve

In a typical transmission microscope setup the probe and the sample are separated by a small air-gap as shown in Fig. 6.4. The THz pulse passes through the air gap interfaces, reflections from which induce changes in the detected field. The problem of pulse

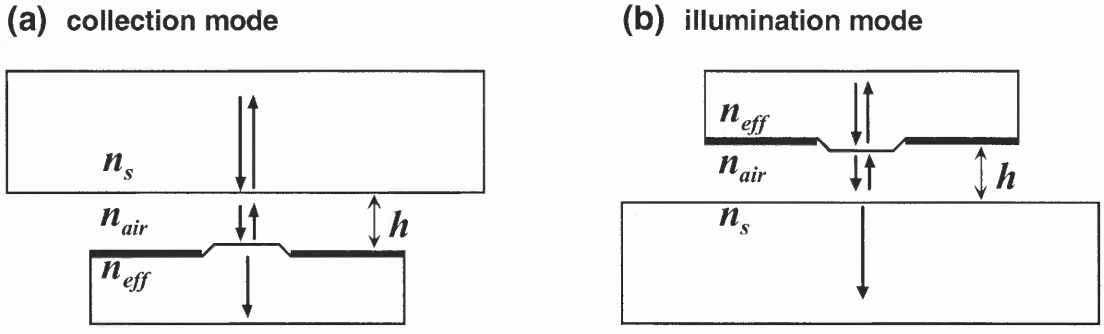


**Fig. 6.4.** Schematic diagrams of the THz beam transmission through the air gap between the sample and the probe in collection (a) and illumination (b) modes.

transmission through the air gap between the sample and the probe is similar to the problem of transmission through the air gap between two dielectric media. The air-probe interface, of course, is more complicated, because the transmission coefficient is frequency dependent and its value is much smaller, compared to the simple air-dielectric interface. Nevertheless, the problem is quite general and the solution is helpful in understanding the field coupling into the probe in the presence of a sample.

Consider the pulse transmission through the air-gap between two dielectric media. An electromagnetic wave incident on an interface between two dielectric media with different indices of refraction is partially transmitted into the second media. The relative amplitudes of the reflected ($E_R$) and transmitted ($E_T$) fields are given by the Fresnel formulas, and for the case of normal incidence are

$$\frac{E_T}{E_0} = \frac{2n_1}{n_1 + n_2} \tag{6.1}$$

$$\frac{E_R}{E_0} = -\frac{n_1 - n_2}{n_1 + n_2}. \tag{6.2}$$

When the two interfaces are present, the incident wave experiences multiple reflections between interfaces. A part of the wave bounces off the interfaces gaining an additional time delay. The total transmitted and reflected waves are the results of the reflections interference, and for a monochromatic light the total transmission coefficient is an oscillatory function of the air-gap width and the wavelength.

If the incident field is a short pulse, the transmitted field becomes a train of pulses with decreasing amplitude. Figure 6.5 demonstrates calculated transmission and reflection of a THz pulse from the air-gap between two dielectric materials with $n_A$=3.1 (sapphire) and $n_C$=3.5 (GaAs). The result is obtained using FDTD method for the one-dimensional wave equation (Appendix B). The incident pulse has a unitary amplitude in the first media and propagates to the right. The pulse impinges on the dielectric-air interface, where it experiences partial reflection. The transmitted part propagates through 300 $\mu$m wide air-gap (indicated by the dashed lines in Figure 6.5(a)) and transmits partially through the second interface. Therefore, loosing a portion of its energy in reflections, the pulse passes into the second media.

A part of the pulse that reflects from the second dielectric continues bouncing inside the air-gap. Each time this 'trapped' pulse impinges the air-dielectric interface, a portion of the energy transmits into one of the dielectrics, resulting in the trains of pulses with decreasing amplitudes, which propagate away from the air-gap. At the moment of

the snapshot of Figure 6.5(a), the incident pulse has already experienced multiple reflections. The main pulse in the region C is followed by the weaker pulses at a distance corresponding to an additional double-pass through air-gap. Note that there is a phase reversal when a wave reflects from the interface with $n_1<n_2$. An even number of such reflections brings the phase back, therefore the forward propagating pulses have the original phase. In contrast, the backward propagating pulses experience an odd number of reflections. All of them, except the first one, have the reversed phase. The first back-propagating pulse is a result of the reflection from the dielectric-air ($n_1>n_2$) interface, and therefore, it preserves its phase.

As the air-gap width decreases, the interval between the pulses reduces, and eventually their waveforms overlap. It becomes no longer possible to resolve temporally each reflection when the air-gap width, $h<100$ $\mu$m. In the limit of $h=0$ all the forward propagating pulses constructively interfere and the total transmitted field has the same time domain waveform as the incident. Contrary the backward propagating pulses interfere destructively as shown in Figure 6.5(b).

Variation of the transmitted field as a function of the air-gap width can be shown by sampling electric field at a fixed time, corresponding to the amplitude peak of the pulse [Fig. 6.6]. At large distances, the signal is at a level of the maximum amplitude of the first transmitted pulse. All the other subsequent pulses do not contribute to the signal because they arrive at the detection point latter in time. The function minimum at $h=55$ $\mu$m corresponds to the overlapping of the first pulse with the second that is delayed by approximately the half-cycle period. In this case, the minimum of the second pulse arrives at the detection point at the same moment as the maximum of the first pulse.

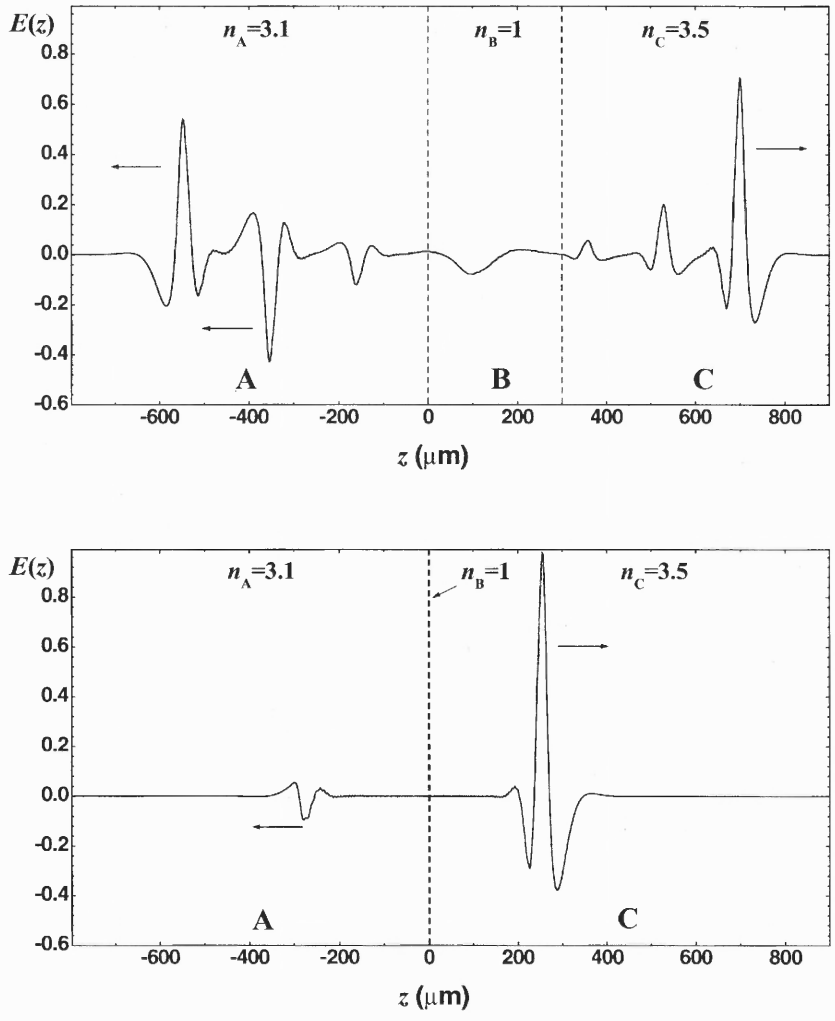


**Fig. 6.5.** Calculated reflection and transmission of the THz pulse at the air-gap (region B) interfaces with dielectrics A and B. The air-gap width is (a) 300 $\mu$m and (b) 2 $\mu$m. Interfaces are indicated by the dashed lines, and the arrows show directions of propagation.

For smaller $h$, the amplitude of the detected signal increases and approaches a level that corresponds to the no air-gap case. This level, as well as the large $h$ limit, is directly found using the Fresnel formulas.

The signal dependence on the distance between the sample and the probe is usually referred to as an approach curve. The signal is an instantaneous measured or calculated electric field at a fixed time (usually peak of the pulse). Two general properties

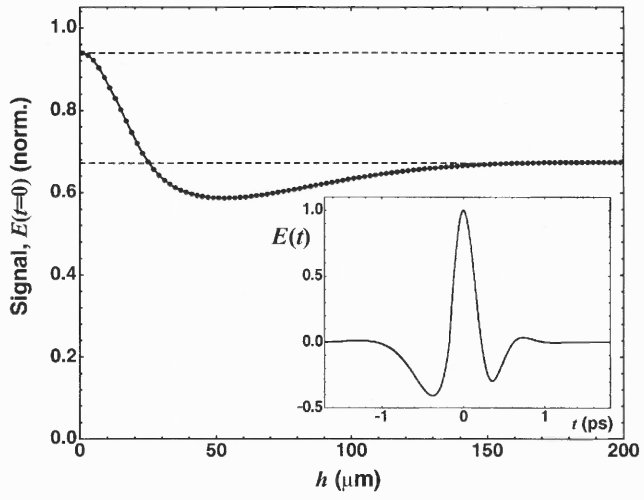


**Fig. 6.6.** Calculated variation of the electric field measured at a fixed time delay. The inset shows the waveform of the incident pulse. The dashed lines indicate the limiting cases of the large $h$ and $h$=0, directly calculated using Fresnel formulas.

of the 'approach curve' can be deduced for the case of the air-gap between two plain dielectrics.

(1) The signal stays constant at $h>\tau c/2$, where $\tau$ is the pulse duration, and reaches a definite value in the limit of $h$=0. The limits are determined by the refractive indices of the two dielectric media.

(2) The approach curve shape is defined by the pulse waveform at the intermediate distance $h$.

Figure 6.7 shows an experimentally measured approach curve. The first dielectric in experiment, a sapphire plate, is placed in front of the detecting antenna on GaAs that serves as the second dielectric. The approach curve is measured by sampling the electric field at a time delay that corresponds to the peak of the first transmitted pulse. Using its peak amplitude, one finds the limiting cases of the approach curve (shown as the horizontal lines in Figure 6.7). The minimum of the approach curve at $h$=105 $\mu$m exactly

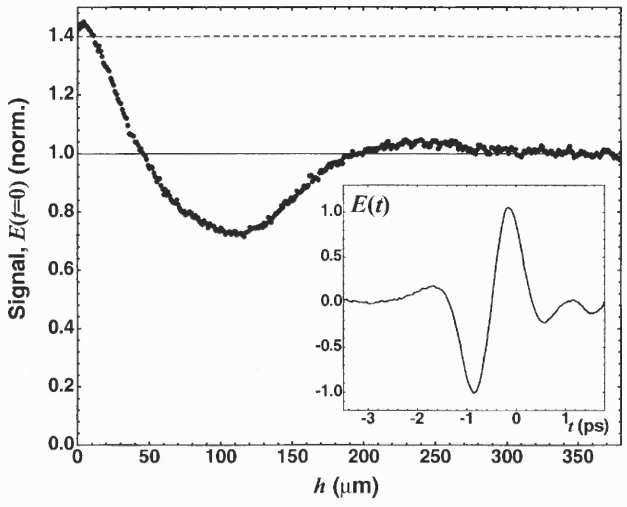


**Fig. 6.7.** Measured approach curve for the case of two dielectrics, sapphire ($n$=3.1) and GaAs ($n$=3.5). The inset shows the waveform of the incident pulse. The dashed line denotes the $h$=0 limit estimated using the Fresnel formula.

matches a half-distance between spatial locations of the maximum ($t$=0 ps) and the minimum ($t$=-0.7 ps) of the unperturbed waveform [inset of Fig. 6.7]. Clearly, the experimental observations demonstrate the multiple reflections between the two closely spaced dielectrics.

Now consider the pulse propagation through the air-gap between the probe and a dielectric sample. The major difference from the two-dielectrics case is that reflection from the probe surface is almost unity. In fact, the probe can be considered as a mirror. Only a negligible portion of the incident pulse is transmitted through the aperture and detected. Since the problem of pulse propagation can be simply reduced to the problem of the reflections interference, the detected electric field is expressed as a summation of pulses with diminishing amplitude

$$E(t,h) = \bar{T}\sum(R_{as}\cdot\bar{R})^m E(t-\frac{2hm}{c}), \qquad m=0,1.. \qquad (6.3)$$

$R_{as}$ is the reflection coefficient for the air-sample interface. Transmission and reflection operators $\overline{T}$ and $\overline{R}$ are the frequency dependent characteristics of the probe aperture. Using the fact that almost all the radiation is reflected from the subwavelength aperture, the reflection operator is assumed to be unity. Action of the transmission operator $\overline{T}$ on the incident electric field waveform is directly measured in experiment

$$\overline{T}E_{inc}(t) = E_{meas}(t). \tag{6.4}$$

In this approximation, electric field is

$$E(t,h) = \sum \left( \frac{n_s - 1}{n_s + 1} \right)^m E_{meas}(t - \frac{2hm}{c}), \tag{6.5}$$

where $n_s$ is the refractive index of the sample.

Equation 6.5 is a simple expression for the electric field dependence on the probe-sample separation. It allows estimation of the approach curve in collection mode using only the measured waveform and the refractive index of the sample. The formula uses the plane wave approximation and neglects the frequency dependent transmission function of the probe aperture. Nevertheless, the approach curves calculated using Eq. 6.5 are in a good agreement with experimental measurements for apertures smaller than 30 $\mu$m. As the size of the aperture decreases, the reflection from the probe becomes closer to unity, and our approximation becomes closer to reality. Figure 6.8 shows the approach curve measured for the 10 $\mu$m aperture probe (b) and the whole waveforms for the two limiting cases $h$=0 and large $h$ (a). A uniform flat sapphire sample, index of refraction of which $n_s$=3.1, is used in this experiment. Figure 6.9 demonstrates the reflection contribution to

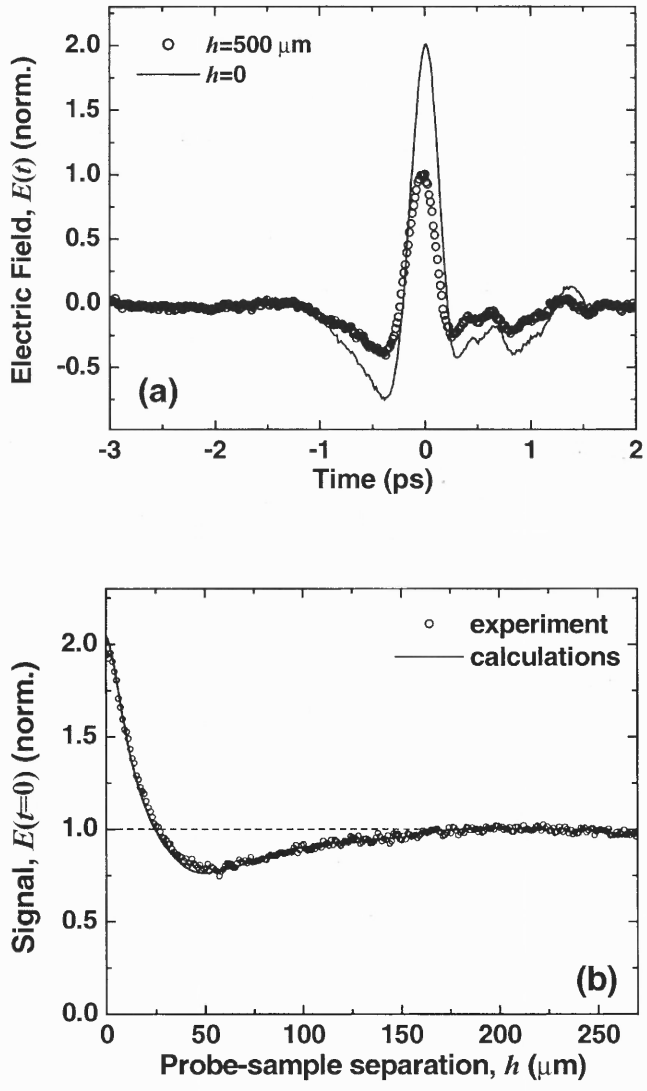


**Fig. 6.8.** Variation of the electric field detected using the 10 $\mu$m probe with the probe-sample separation, $h$. Sample is a sapphire plate (n=3.1). (a) The waveforms of the limiting cases $h$=0 and $h$=500 $\mu$m. (b) The approach curve, measured (circles) and calculated (solid line).

the signal at various probe-sample distances. The individual reflections are shown with arrows in the time domain waveform.

The illumination mode setup [Fig. 6.4(b)] exhibits a similar signal dependence of the probe-sample separation. Calculation of the approach curve is more involving, since

the probe radiates into a wide solid angle. Therefore, the general Fresnel formula applies instead of Eq. 6.1, and the additional pass for the reflected pulse includes the direction of propagation.

It must be mentioned that the high-resolution near-field imaging always requires the probe and the sample being almost in contact. Within this limit, the waveform of the detected THz pulse does not depend on the probe-sample separation, and only the pulse amplitude varies. In the near-field image, this variation of the signal can be caused by

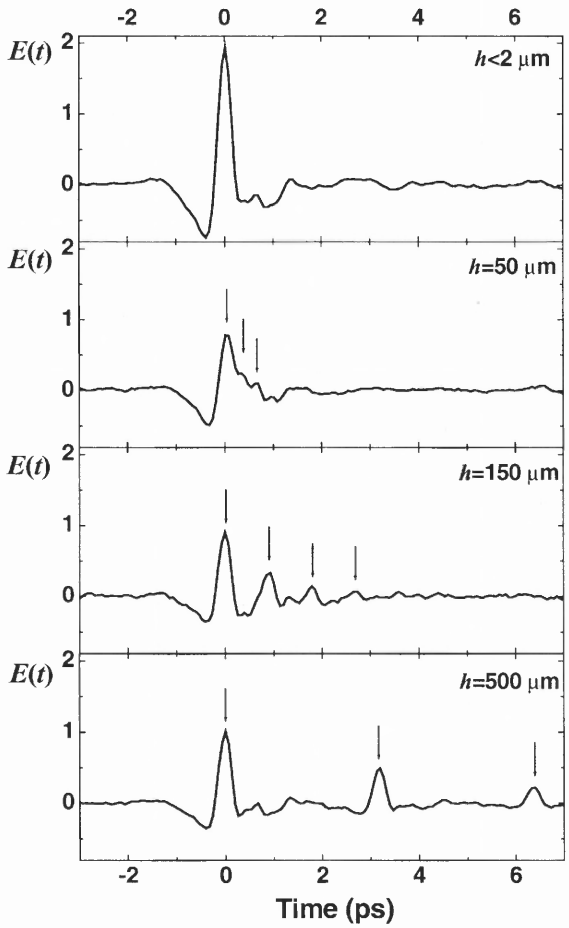


**Fig. 6.9.** Time domain waveforms measured at various probe-sample separations, $h$. Arrows show individual reflections. The aperture size is 10 $\mu$m.

either the non-constant distance between the probe and the sample, or by a non-uniform optical density on the sample surface.

### 6.3.2 Depth of Field

It was mentioned in Sec. 3.2.1 that the high spatial resolution near-field imaging requires the probe-sample separation to be smaller than ~1/3 of the aperture size. This shallow depth of field limits the range of samples that can be studied with the near-field method [Novotny *et al.* 1994]. Since the system operates in transmission, the thickness of the sample structure needs to be smaller than the depth of field. Separation between the probe and the sample must be kept small and constant throughout the scan. As the sample-probe separation, $h$, increases, the image sharpness decreases. Shallow depth of field can be demonstrated experimentally by performing the resolution test at various $h$.

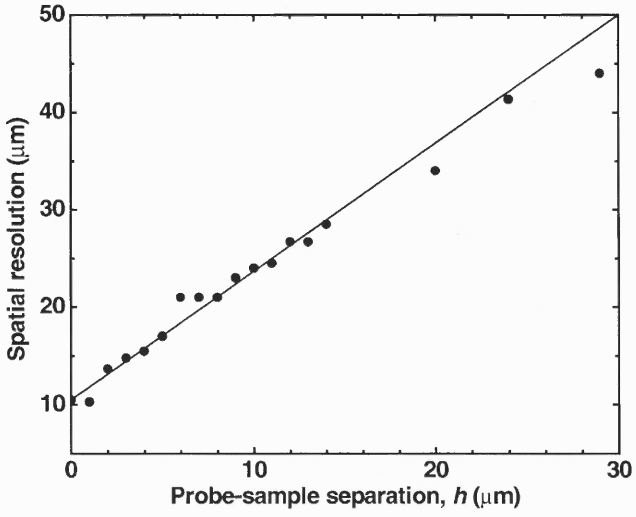


**Fig. 6.10.** Results of the spatial resolution edge tests (10%-90%) on the near-field probe with $d$=10 $\mu$m and $L$=4 $\mu$m in collection mode at various probe-sample separations.

Figure 6.10 shows results of the edge tests (10%-90%) for a probe with $d$=10 $\mu$m. Resolution degrades with increasing distance $h$ approximately linearly for small values of the probe-sample separation. This behavior is a general property and similar results are obtained using probes with different aperture sizes, $d$, and aperture-antenna separations, $L$. The experiments are performed in collection mode, however, the results are similar in illumination mode.

The shallow depth of field of the instrument implies the following important conclusion for imaging of dielectrics with near field probes $d<<\lambda$. The dielectric function contrast decreases with the probe aperture size. When imaging spatial distribution of the refractive index (or the dielectric function), the measured signal variations arise from the index-dependent coupling into the probe, the phase shift $\Delta\phi$ and absorption (if the dielectric is lossy) due to the pulse propagation through the sample. The later contributions are directly proportional to the thickness of the sample. For the phase shift we have

$$\Delta\phi = 2\pi\frac{\Delta ns}{\lambda}, \qquad (6.6)$$

where s is the thickness of the sample, which is smaller than or equal to the depth of field. In the high resolution imaging the phase shift becomes very small and, therefore, difficult to image, since the signal-to-noise ratio also decreases.

Similarly, absorption in the sample decreases with the thickness. For example, decay length for THz pulses (0.6 THz) in water is ~250 $\mu$m. Biological samples, which mostly consist of water molecules, are not expected to produce a strong contrast on 5-10 $\mu$m resolution level.

## 6.4 Polarization Dependence

When the incident electromagnetic wave interacts with a small (compared to the wavelength) object, the field distribution around the object is extremely sensitive both to the physical properties of the object (shape, size, and optical index) and properties of the incident wave [Martin *et al.* 1995]. A detailed understanding of this optical interaction between the sample and the optical field is one of the most serious challenges in near-field microscopy.

Polarization of the incident THz field is particular important when a sample contains metallic features, e.g. a pattern of an integrated circuit. Boundary conditions at the metallic edges require the tangential component of electric field to disappear. The normal field components contrary are singular at the metallic edges, because the field induces charges at the boundary. As a result, metallic edges appear differently in near-field images depending on orientation of the incident pulse with respect to the polarization.

For instance, consider a plane wave incident on an edge of a thin metallic screen. Electric field energy distribution of a wave propagating past the edge is schematically

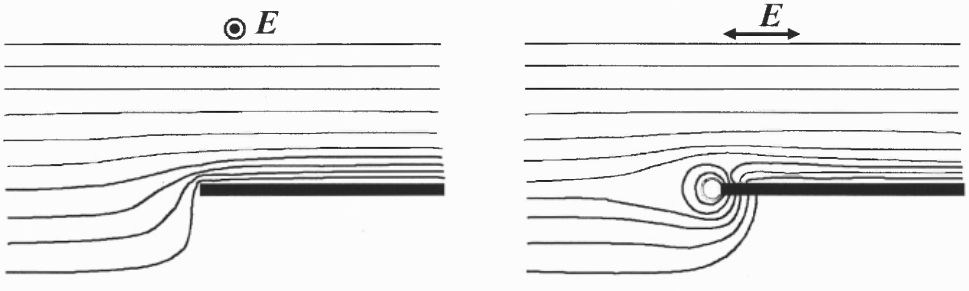


**Fig. 6.11.** A schematic diagram of electromagnetic wave diffraction on a metallic edge in the cases of polarization parallel to the edge (left) and perpendicular to the edge (right). Solid contour lines show $|E|^2$.

shown in Figure 6.11 for two principle polarization directions. The wave is normally incident on the screen from the top. If electric field vector oscillates parallel to the screen edge (left figure), the field vanishes everywhere on the metallic surface. The screen creates a well-defined shadow zone as the wave passes it. Continuing its propagation, the wave diffracts and bends slightly over the edge.

In the second case, when electric field vector is perpendicular to the edge (right figure), the incident wave induces charge on the screen. The charge density is maximal at the edge, decreasing as a square root of distance from the edge [Jackson 1962]. The electric field vector, perturbed by the induced charge, points to the edge, where it abruptly vanishes. The wave continues propagation after passing over the screen, however, in the second case the wave is strongly deflected from the initial direction. In principle, the

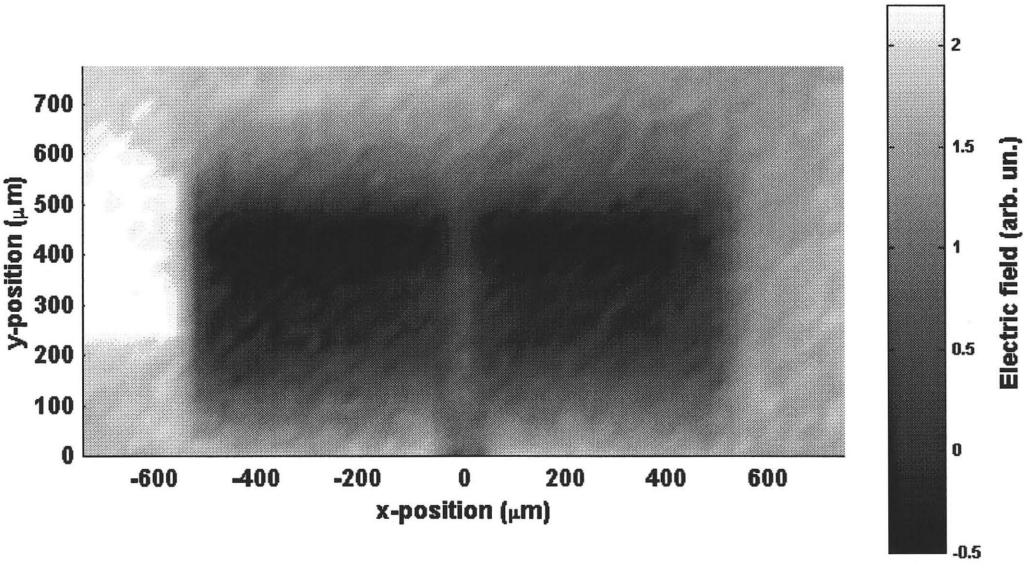


**Fig. 6.12.** A near-field image of square-shaped gold antenna pads lithographically printed on a semiconductor surface. Gray level corresponds to electric field amplitude measured at the THz pulse peak (at a fixed time delay). The image is constructed using a probe with a 30 $\mu$m aperture.

wave can propagate along the metallic screen, perpendicular to its original direction.

This diffraction process produces polarization related artifacts in the near-field images of the metallic patterns. Edges parallel to polarization appear sharper in the image than ones perpendicular to polarization. Figure 6.12 shows a near-field image of large (500×500 $\mu$m) square-shaped metallic pads deposited on GaAs surface. A probe with a 30 $\mu$m aperture is used in this experiment and polarization of the incident beam is along $y$-direction. The square-shaped pads appear elongated in $x$-direction because the horizontal borders are not as sharp as the vertical ones.

The polarization sensitivity has its effect on the resolution measurements discussed in Sec 6.2. In the resolution test, the edge object is used to produce a sharp field contrast between two halves of the sample. Only incident polarization parallel to the edge serves this purpose.

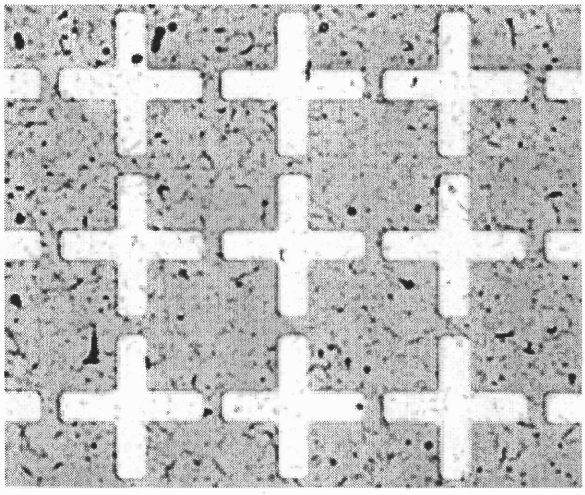

**Fig. 6.13.** An optical microscope image of the periodic cross pattern lithographically printed on dielectric surface (GaAs, $n$=3.6). The lattice period is 26.4 $\mu$m, width of the cross-bars is 4.8 $\mu$m, and a gap between crosses is 3.2 $\mu$m.

Another polarization related effect occurs when the metallic object parts are on the order of the aperture size or smaller. As an example we consider a periodic structure that consists of metallic crosses on surface of a dielectric substrate. The crosses are arranged in a simple square lattice with a period of 26.4 $\mu$m as shown on an optical microscope image in Figure 6. 13. Width of the cross-bars is 4.8 $\mu$m and the substrate index is 3.6 (GaAs). The periodic cross-shaped structure has a narrow absorption resonance at ~115 $\mu$m (2.6 THz) [Moller 1999]. At larger wavelengths the structure is relatively transparent. A vertically polarized ($y$-direction) THz beam uniformly illuminates the sample and near-field images are constructed in collection mode with 5 $\mu$m and 10 $\mu$m aperture probes. Spatial resolution of the probes is ~7 $\mu$m and ~10 $\mu$m respectively. Figure 6.14 shows an image obtained at a fixed time delay, when the 5 $\mu$m

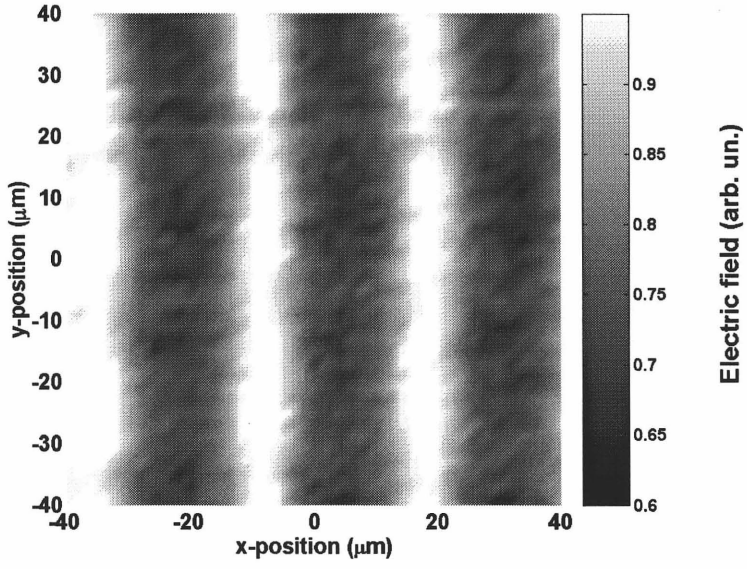


**Fig. 6.14.** A near-field image of the metallic crosses shown in Fig. 6.13. Gray level corresponds to electric field amplitude measured at the THz pulse peak (at a fixed time delay). The image is constructed using a probe with a 5 $\mu$m aperture.

probe measures the peak of the THz pulse. The vertical bars of the crosses (parallel to polarization) are clearly developed in the image, while the horizontal bars are almost invisible.

Note that the brighter areas in the image correspond to the vertical metallic bars. The electric field amplitude of the pulse coupled into the aperture is larger when the probe is located behind the bars. This effect is present even if the aperture size is larger than the bar width. Figure 6.15 shows an image fragment of the same sample constructed using 10 $\mu$m aperture probe. The vertical bars, which are only 5.8 $\mu$m wide, produce an image similar to Figure 6.14. The horizontal bars, contrary, do not produce noticeable traces in the images. The field 'wraps' around the small metallic structures and passes without significant perturbation. It is worth mentioning the principle of wire grid polarizers, which strongly absorb waves with electric field oscillating along the direction

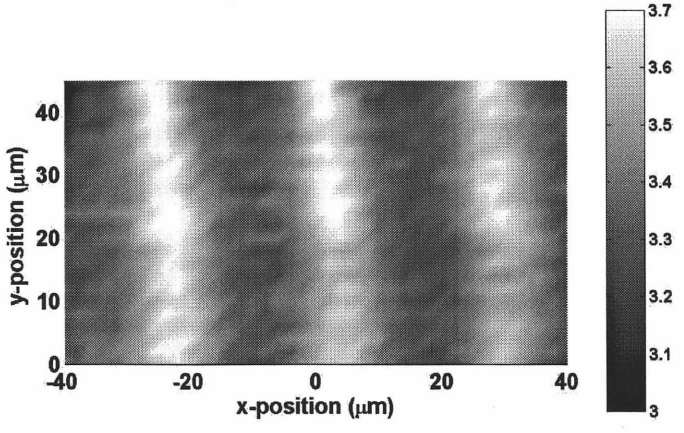


**Fig. 6.15.** A near-field image of the metallic crosses shown in Fig. 6.13. Gray level corresponds to electric field amplitude measured at the THz pulse peak (at a fixed time delay). The image is constructed using a probe with a 10 $\mu$m aperture.

of the wires. The orthogonal polarization passes the grid of wires almost without changes, if the wire diameter and the separation between wires are smaller than the wavelength.

Polarization effects exist for dielectric objects as well. Webber *et al.* 1996 experimentally showed that the same dielectric subwavelength object produced inverse contrast for two polarizations, TE and TM.

## 6.4 Analysis of THz Near-Field Images

### 6.4.1 Introduction

A near-field image corresponds to the electric field distribution in the vicinity of an object, which in general differs from the object physical structure. The purpose of image analysis is to link the near-field measurements to the object's properties. This task is very difficult, especially when various artifacts are present. Object reconstruction is an inverse scattering problem, and there is more than one configuration that results in the same near-field image. It is usually helpful to have some preliminary information about the object, such as composition, surface quality, etc, in order to obtain accurate information.

Scanning microscopy with time domain measurements generates a large amount of data. There is an array of electric field values for every point in the object plane. Using the data, various types of images can be constructed: the monochromatic images throughout the spectrum of the THz pulses or the time series of instant field images. The acquisition time substantially decreases if only a time slice of the full data is measured. This approach, however, looses some of the available information. The image evolves in time and the object features may appear differently at various instants of time. This raises a practical question: can a single time slice of data provide sufficient information about

an object? This section discusses the correspondence between an object and its instant images. The analysis is carried out on example of a metallic dipole antenna pattern prepared on a dielectric surface.

### 6.4.2 Evolution of the Image

The antenna is lithographcally printed on a sapphire substrate and consists of two 20 $\mu$m wide striplines separated by 105 $\mu$m, and two sharp-ended 50 $\mu$m long and 20 $\mu$m wide arms, slightly shifted with respect to each other. A schematic diagram of the antenna is shown in Figure 6.16(a). The object contains only gold features oriented either parallel to the direction of polarization (dipole arms) or perpendicular to it (strip lines). The images are constructed in collection mode using a 10 $\mu$m aperture probe ($L$=4 $\mu$m) at consequent moments in time.

The series of frames in Fig. 6.16 demonstrates changes of the image with time. Frames (b) ($t$=-0.5 ps) and (d) ($t$=0) correspond to the negative and positive peaks of the pulse waveform. The images are similar except for polarity. The dipole creates a shadow in the center, which extends slightly toward the striplines. Oriented perpendicular to the incident field polarization, the striplines exhibit weaker contrast than the dipole in these images.

All object features develop well in frame (c) ($t$=-0.33 ps), which corresponds to a moment between the negative and positive peaks of the THz pulse. Both the striplines and the dipole arms are clearly seen. However, the object parts oriented perpendicularly to the polarization direction appear brighter, and the parts oriented parallel to it appear darker with a higher contrast. Resolution is comparable in both directions.

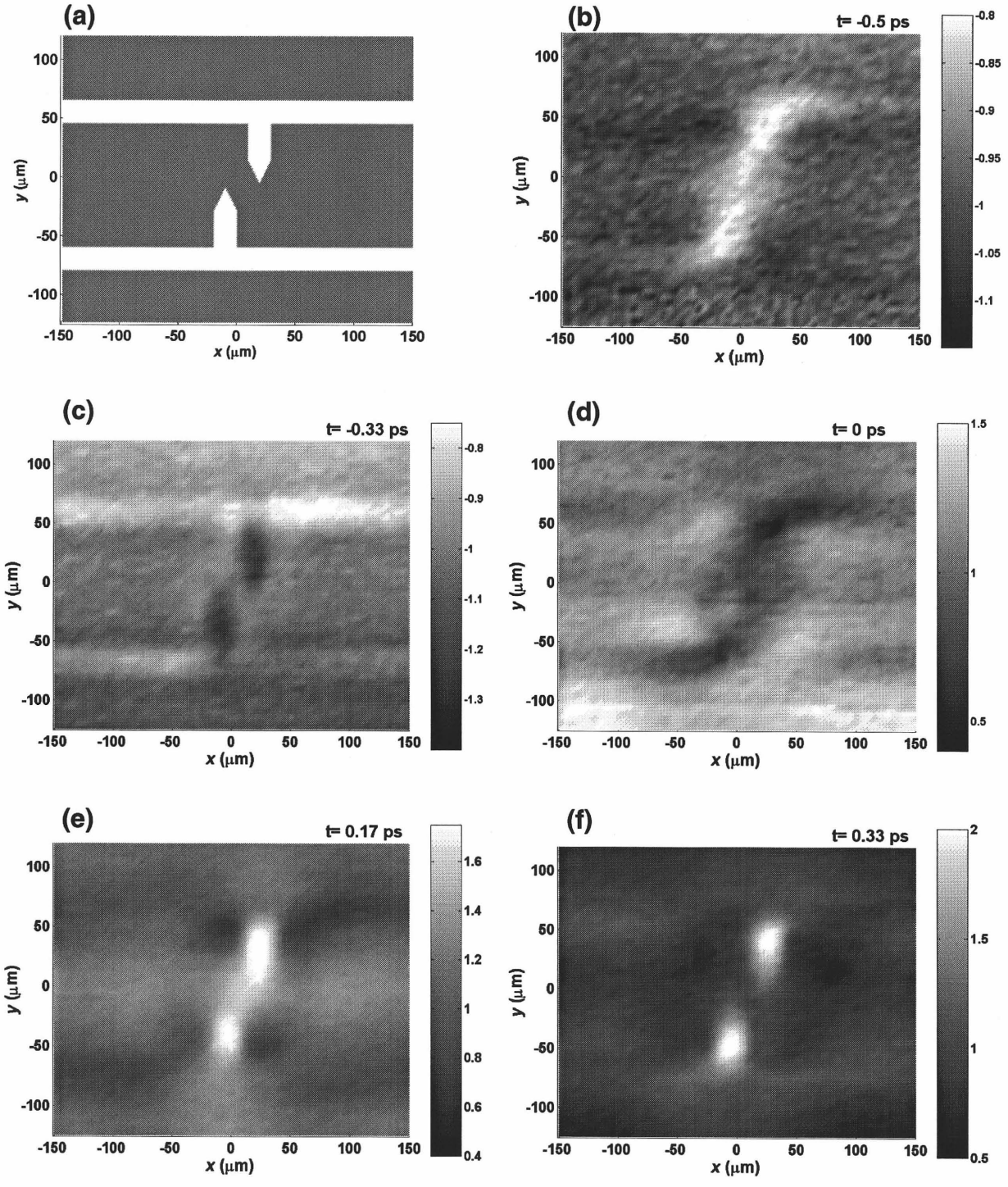


**Fig. 6.16.** A schematic diagram of a planar antenna on sapphire (a). Series of near field images taken at different time delays of the gating optical pulse(b-f). The gray level corresponds to the measured electric field.

In the frame (e) there is electric field enhancement in the middle of the antenna between the dipole arms. This effect is due to sharp corners of the electrodes, where induced charge and, therefore, electric field are singular [Jackson 1962]. Frames (e) ($t$=0.17 ps) and (f) ($t$=0.33 ps) show another effect. The dipole arms are imaged as bright spots with high contrast. Both images correspond to the positive time delay, when the background electric field amplitude has already decreased.

It is informative to consider time domain waveforms measured at various points of the object. Figure 6.17 shows THz waveforms measured aside from the structure (dotted curve), at a stripline (dashed curve), in the middle between the striplines (dash-dotted curve), and in the area of the dipole (solid curve). A schematic diagram in the right corner shows the locations of the test points. One can see an obvious perturbation of the electric field due to the dipole. A waveform measured shows slower temporal

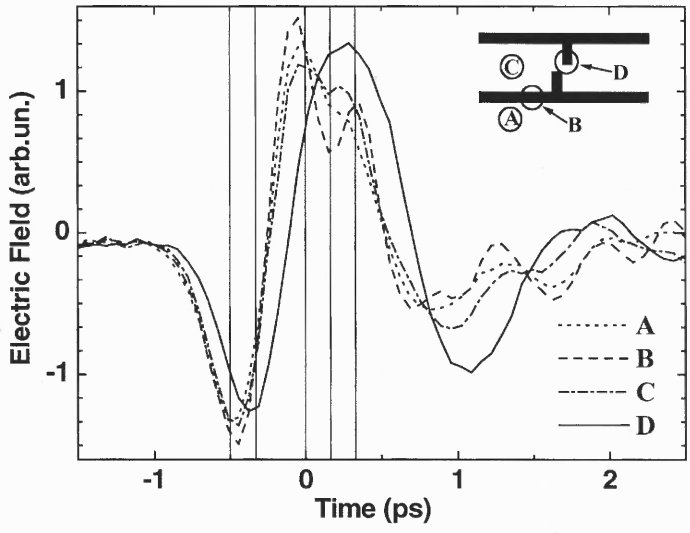


**Fig. 6.17.** THz waveforms measured in various point of the object. A schematic diagram in the right corner shows location of the test points: aside from the structure (A), at a stripline (B), in the middle between the striplines (C), and in the area of the dipole (D). The vertical lines in the plot indicate the instants in time-domain, which correspond to the image frames in Fig. 6.16.

characteristic and a delayed phase, compared to a waveform measured away from the antenna. Therefore the dipole appears glowing after the peak of the incident pulse has passed ($t$~0.2-0.5 ps). Very bright areas in frames (e) and (f) imply that there is electric field enhancement at the dipole. Effect of the striplines is less pronounced. The waveform measured at point B resembles the incident waveforms, and the image contrast of the striplines is weak.

### 6.4.3 Time-Domain vs. Frequency-Domain Imaging

From the analysis above, one can deduce two effects that mainly determine the appearance of this object in the near-field image: the polarization effect, which was discussed in the previous section and the effect of pulse deformation due to the object. The later is due to resonant properties of the dipole antenna structure. It is known that a dipole antenna absorbs and radiates within a narrow band, which corresponds to the dipole length. As a result, electric field near the dipole oscillates slower with a central frequency drawn closer to the resonant frequency of the antenna.

It is obvious that for studies of the resonant effects the full set of the time-domain data must be considered. Fourier spectra are obtained for every point of the object. Monochromatic images are then constructed using the spectral amplitude or phase information. Resonant structures, such as the considered dipole antenna, are expected to produce frequency dependent images.

One of the applications of this method, which can be called the THz spectroscopy in the near-field zone, is the transient current studies in switches. The current distribution in photoconducting switches is directly related to the geometrical structure of electrodes

and the carrier dynamics in the active area. Simulations of this process for the switch performance optimization are quite complicated. The current transients in principle can be directly measured with resolution of 5-10 $\mu$m using our near-field probe. The carriers tend to move faster in the center of the switch, where electric field is higher. The slower carriers move on the sides. This dynamics is expected to reflect in the monochromatic THz near-field images. Some effects, such as charge screening, are difficult to model in simulations, and experimental technique can provide important information about dynamics of the carriers in the switch and help in the performance optimization.

It should be mentioned that electric field waveform measured by the collection probe is not a direct replica of the field at the object. The aperture of the probe changes the waveform and the spectrum due to the frequency dependent transmission, as discussed in Chapter 5. In principle, the original waveform can be extracted if the transfer function of the aperture is known. For a simple aperture in a thin metallic film this transfer function only affects the amplitude of the spectral components of the pulse. The phase shift can be assumed to be equal to zero. (The effective phase shift due to asymmetric temporal characteristic of the THz pulse is automatically taken into account applying frequency dependent amplitude attenuation.)

The knowledge of the field spectrum before transmission through the aperture provides the correct ratio of the spectral amplitudes. However, for the monochromatic images, where brightness corresponds to the relative amplitude of a particular spectral component, this information is not necessary.

# CHAPTER 7

# CONCLUSION

## 7.1 Main Results

Application of the near-field scanning microscopy principle to the long wavelength terahertz radiation substantially improves spatial resolution capabilities. The practical limitation, related to the rapid decrease in sensitivity of the aperture type near-field probes with a decreasing aperture size, has been overcome in the new probe design. The collection mode near-field probe, which uses a subwavelength aperture to sample the electric field of an object, detects the coupled into the probe field in the aperture near-zone. The probe detects the electric field, which mostly consists of the aperture evanescent modes. Sensitivity of the new design improves by few orders of magnitude (depending on the aperture size) compared to the conventional design, where only the propagating modes are detected. The highest achieved spatial resolution of the probe is ~7 $\mu$m, which is three times better then the best of the other currently available THz imaging techniques.

A simple two-dimensional model describes propagation of the THz pulse through subwavelength apertures. Numerical calculations based on time-domain finite-difference method demonstrate that the model predicts deformation of the pulse waveform and spectrum. The time-domain formulation provides the solution without the need for the long wavelength approximation, which, in fact, is not valid for the broad band THz pulses. The pulse deformation, described as the wavelength dependent process, shows two distinct regimes: below- and above the aperture cutoff frequency. The effects of the

waveform shaping and the spectral shift differ in these regimes. The relative phase of the spectral components causes the effect of the pulse advance through the deep-subwavelength aperture with a negative time shift.

Images constructed using time resolved electric field measurements carry various artifacts. Some of them, such as the polarization related or the probe-sample separation related artifacts, are well known in optical microscopy. The other are related to the pulse shape deformation.

Aperture size determines the spatial resolution of the developed imaging system. With decreasing aperture size, the electric field coupled through the aperture decreases, as predicted by the Bethe's theory with the finite-thickness screen correction. The resolving power of the system can be further improved to the level of ~1 $\mu$m if a more powerful THz source is available.

## 7.2 Practical and Scientific Value

### 7.2.1 Practical Value

The developed imaging system provides currently the highest spatial resolution for the long wavelength THz radiation. Resolution is independent of the wavelength throughout the spectrum of the THz pulses (120 $\mu$m –1500 $\mu$m), and spectroscopy at THz frequencies can be implemented with high spatial resolution.

The technique is valuable for studies of near-field image formation. Given the large scale of the wavelength, the system can be used as a model of the near-field scanning optical microscope. The image formation mechanisms and artifacts can be

studied using enlarged samples. In the studies of the probe-sample separation effects, for example, the leading contribution of interference of reflections is demonstrated.

### 7.2.2 Scientific Value

Coupling of the broad band THz pulses through subwavelength apertures is a relatively unexplored problem. The interest to this problem arises form the fact that the cutoff frequency of the aperture is usually within the spectral bandwidth of the THz pulses. In this regime, the electromagnetic pulses experience the temporal and spectral deformations. The current study provides the analysis of the problem with explanation and experimental demonstration of certain effects. The experimental work gives a valuable data on electromagnetic wave transmission through apertures as small as 1/300 of the wavelength.

The two-dimensional model is demonstrated to describe the transmission of the THz pulses through small apertures. The numerical calculations predict the waveform and the spectrum deformation, give the qualitative field description in the near-zone, and allow studying effects of the probe geometry. Decay of the electric field amplitude with the distance from the aperture is characterized experimentally in the near-zone. The mode analysis demonstrates that the evanescent modes produce the dominant contribution within the distance equal to the aperture radius.

For apertures ranging from 50 $\mu$m to 5 $\mu$m, the electric field amplitude of the coupled field decreases approximately as the third power of the aperture size. A correction due to the finite-thickness of the aperture screen is required as the aperture size decreases. The resulting amplitude function decreases faster then the third power law when the aperture size is on the order of the screen thickness.

### 7.2.3 Future Studies

Detailed understanding of image formation in THz near-field scanning microscopy remains one of the serious challenges. The image formation is, essentially, the problem of electromagnetic wave coupling through the aperture in the presence of an object. The current study only considered few aspects of this broad problem. Extensive experimental work and numerical modeling yet need to be accomplished. Another direction of the potential research is development of THz spectroscopy. The spectral analysis can be realized with the existing setup. However, the critical issues, such as frequency dependence of the probe sensitivity, have not been addressed.

## APPENDIX A: CHARACTERIZATION OF CARRIER LIFETIME IN LT GaAs BY THE TRANSIENT REFLECTIVITY MEASUREMENTS

For the optimum performance of THz detectors, the carrier lifetime in the photoconducting material must be short, so that the incident electric field is slowly varying on the time scale of the photocurrent transient. The short lifetime is usually achieved by introduction of impurities in the semiconductor. In the same time, the dark resistivity must be high for the low noise detector. The perfect material for the switch has the high mobility and the short carrier lifetime.

The post-growth annealing balances these properties in LT GaAs [Smith *et al.* 1997]. As-grown LT GaAs is highly conductive, but after annealing the resistivity of the material increases up to $10^7$ Ohm cm. However, exposure to the temperatures increases the carrier lifetime in LT GaAs. Estimation of the lifetime from specified growth and annealing conditions is rarely accurate due to variations in the growth process and difficulties of exact temperature measurements at the surface of the material. To optimize the THz detector performance, it is important to have an apparatus for determining the carrier lifetime in the LT GaAs epilayers.

The methodology for determining the carrier lifetime is based on the femtosecond transient pump-probe technique [Bennett *et al.* 1990, Loka *et al.* 1998]. In the experiment, an intense ultrashort pump laser pulse induces changes in the optical properties of the sample. Photons with energy larger than the bandgap generate the electron-hole plasma in the semiconductor that dissipates through trapping, recombination and diffusion. The dynamics of the carriers is determined by measuring the intensity of a weaker probe pulse, either reflected or transmitted, as a function of the

delay between pump and probe pulses. Free carrier concentration due to the pump pulse can be extracted from the measured reflectivity or absorption transients.

Short optical pulses of ~100 fs duration at 100 MHz repetition rate are generated by the laser system, which consists of an $Ar^+$-ion and Ti:Sapphire lasers. A pulse is divided in two: a pump pulse and a weaker probe pulse. The pump beam is chopped by the acousto-optic modulator at frequency of 1MHz. Each pulse carries energy ranging from 0.1 nJ to 20 nJ. The probe pulse is typically one or two orders weaker and it is cross-polarized with the pump. An optical delay line allows sampling the transient reflectivity induced by the pump. The beams are focused onto the sample to a 100 $\mu$m and 70 $\mu$m diameter spots for the pump and probe respectively. The reflected light intensity is measured with a photodiode and processed using the lock-in amplifier.

A number of physical effects contribute to the pump-induced change in the dielectric constant and, consequently, in the reflection coefficient [Loka *et al.* 1998]. Bandfilling, free carrier absorption, bandgap shrinkage are the effects with the leading contribution. The lattice heating due to scattering of the excited electrons changes reflectivity as well. The relative contribution depends on the intensity of the pump and the energy of the photons [Janz *et al.* 1996, Sosnowski *et al.* 1997, Segschneier *et al.* 1997]. As a result, the change in reflectivity differs in shape, amplitude, and sign depending on the experimental parameters. The detailed analysis of the effects that change the reflectivity can be found in the paper by Bennett *et al.* (1990).

Despite the complexity of the data, the transient reflectivity usually behaves as a two step relaxation process (besides the initial rise time). Immediately after the excitation, the reflectivity of LT GaAs relaxes with a characteristic time of a fraction of

picosecond, followed by a relatively slower decay. This implies that the electrons are trapped on the midgap states first, and recombine with the holes later. The trapping time is on the same order as the carrier cooling time. Table 1 summarize the carrier dynamics in LT GaAs [Grenier and Witaker 1997]. The fast and long recombination are associated with two different types of midgap traps.

| Process | Time Constant, ps |
|---|---|
| Carrier cooling (e/h) | 0.1-0.2/0.3-0.4 |
| Carrier Trapping | 0.7-2 |
| Fast Recombination | ~10 |
| Long Recombination | >300 |

**Table A1.** Typical carrier dynamics in LT GaAs (Reference: Grenier and Witaker 1997).

Typical transient reflectivity traces are shown in Figure A2. The plot demonstrates that the dynamics depends on the annealing conditions. As the temperature

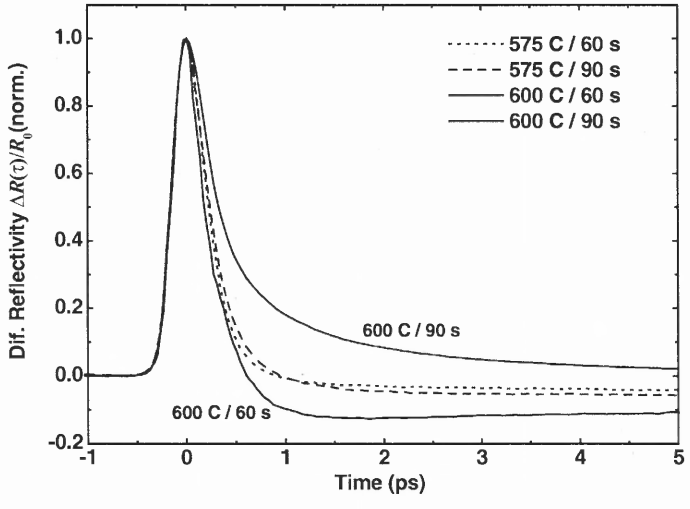


**Fig. A1.** Normalized transient differential reflectivity of typical LT GaAs (T=300°C). Variation of the annealing condition results in changes of the dynamics of the carriers.

or/and the annealing time increases, the relaxation time increases. The growth temperature also affects the relaxation time as shown by many research groups [for example Loka *et al.* 1998].

The control of growth and annealing temperatures can be used to optimize the fast response of the photoconducting antenna. The trapping and trap emptying times increase with increasing the annealing temperatures. However, the post-growth annealing is required to lower the dark conductivity of the material.

## APPENDIX B: ONE-DIMENSIONAL NUMERICAL SOLUTION OF THE PULSE TRANSMISSION THROUGH DIELECTRIC LAYERS

Transmission of an electromagnetic pulse through an air-gap between two dielectric media is numerically solved using FDTD method in one-dimensional space.

Consider the one-dimensional scalar wave equation in a lossless dielectric medium with the dielectric constant $\varepsilon$

$$\frac{\partial^2 E}{\partial t^2} = \frac{c^2}{\varepsilon}\frac{\partial^2 E}{\partial t^2}. \tag{B.1}$$

In the finite-difference approximation of the Eq. B.1 the solution $E_i^{n+1}$ at a grid point $i$ is

$$E_i^{n+1} = \frac{c^2 \Delta t^2}{\varepsilon \Delta z^2}\left(E_{i+1}^n + E_i^n + E_{i-1}^n\right) + 2E_i^n - E_i^{n-1}. \tag{B.2}$$

The approximation has a second-order accuracy in both space and time. Eq. B.2 is an explicit expression for electric field. All wave quantities on the right-hand side are obtained during the previous time steps, $n$ and $n$-1. Upon performing Eq. B.2 for all space points of interest, the process is continued again to obtain the next set of $E_i^{n+2}$. The algorithm employs a central spatial-difference scheme that requires knowledge of the field one cell to each side of an observation point. Central difference can not be implemented at the outermost boundary of the space lattice, since there is no information about the field at points outside the boundaries.

Electric field just outside the boundaries can be found using one-way-wave equations. Application of the one-way equation numerically absorbs outgoing waves impinging on the boundary. For a scalar wave propagating in one-dimensional space domain [0, $L$], the one-way equation at the $z$=0 boundary:

$$\frac{\partial^2 E}{\partial t \partial z} - \frac{c^2}{\varepsilon}\frac{\partial^2 E}{\partial t^2} = 0, \tag{B.3}$$

and for $z=L$ boundary:

$$\frac{\partial^2 E}{\partial t \partial z} + \frac{c^2}{\varepsilon}\frac{\partial^2 E}{\partial t^2} = 0. \tag{B.4}$$

In the finite-difference approximation, electric field value at the boundaries is computed by

$$E_0^{n+1} = -E_1^{n-1} + \frac{v\Delta t - \Delta z}{v\Delta t + \Delta z}\left(E_1^{n+1} + E_0^{n-1}\right) + \frac{2\Delta z}{v\Delta t + \Delta z}\left(E_1^n + E_0^n\right) \tag{B.5}$$

$$E_L^{n+1} = -E_{L-1}^{n-1} + \frac{v\Delta t - \Delta z}{v\Delta t + \Delta z}\left(E_{L-1}^{n+1} + E_L^{n-1}\right) + \frac{2\Delta z}{v\Delta t + \Delta z}\left(E_L^n + E_{L-1}^n\right), \tag{B.6}$$

where $v$ is the speed of light propagation in dielectric.

The incident THz pulse is modeled by assigning electric field at the boundary $z=0$ at every time step ($t$ is in picoseconds):

$$E_0(t) = \begin{cases} \sin(3.5(t-t_0)) \cdot e^{4(t-t_0)}, & t < t_0 \\ \sin(8(t-t_0)) \cdot \dfrac{1}{e^{6(t-t_0-0.35)}+1}, & t \geq t_0 \end{cases} \tag{B.7}$$

After the pulse is completely launched into the computational space, electric field at point $z=0$ is calculated according to Eq. B.5. Dielectric materials in the space lattice are simply modeled by defining the speed of light at each point of the lattice.

## REFERENCES


Barchiesi, D., Girard C., Martin, O. J. F., Labeke, D. V., and Courjon, D., 'Computing the optical near-field distributions around complex subwavelength surface structures: A comparative study of different methods', Phys. Rev. E 54, pp. 4285-92 (1996).

Benicewicz, P. K., Roberts, J. P., and Taylor, A. J., 'Scaling of terahertz radiation from large-aperture biased photoconductors', J. Opt. Soc. Am. B 11, pp. 2533-46 (1994).

Bennett, B. R., Soref, R. A., and Del Alamo, J., A., 'Carrier-induced change in refractive index of InP, GaAs, and InGaAsP', IEEE J. Quantum Electron. 26, pp.113-22 (1990).

Bethe, H.A., 'Theory of diffraction by small holes', Phys. Rev. 66, pp. 163-82 (1944).

Betzig, E., Isaacson, M., and Lewis, A., 'Collection mode near-field scanning optical microscopy', Appl. Phys. Lett. 51, pp. 2088-90 (1987).

Born, M. and Wolf, E., Principles of optics (Cambridge University Press, 1999).

Bouwkamp, C. J., 'On Bethe's theory of diffraction by small holes', Philips Res. Rep. 5, pp. 321-32 (1950).

Bozhevolnyi, S. I., Xiao, M., and Hvam, J. M., 'Polarization-resolved imaging with a reflection near-field optical microscope', J. Opt. Soc. Am. A 16, pp. 2649-57 (1999).

Brener, I., Hunsche, S., Cai, Y., Nuss, M.C., Wynn, J., Lopata, J., and Pfeiffer, L., 'Time resolved near field imaging and diffraction with subwavelength far-infrared dipole sources,' Ultrafast Phenomena XI, pp. 171-72 (1998).

Bromage, J., Radic, S., Agrawal, G. P., Stroud Jr., C. R., Fauchet, P. M., and Sobolevski, V., 'Spatiotemporal shaping of half-cycle terahertz pulses by diffraction through conductive apertures of finite thickness', J. Opt. Soc. Am. B 15, pp. 1399-05 (1998).

Cai, Y., Brener, I., Lopata, J., Wynn, J., Pfeiffer, L., and J. Federici, 'Design and performance of singular electric field terahertz photoconducting antennas', Appl. Phys. Lett. 71, pp. 2076-78 (1997).

Cai, Y., Brener, I., Lopata, J., Wynn, J., Pfeiffer, L., Stark, J. B., Wu, Q., Zhang, X. C., and J. Federici, 'Coherent terahertz radiation detection: Direct comparison between free-space electro-optic sampling and antenna detection', Appl. Phys. Lett. 73, pp. 444-46 (1998).

Cai, Y., 'Enhanced terahertz pulse generation and detection using electric field singularities in photo-conducting antennas', dissertation, NJIT (1998).

Chen, Q., Jiang., Xu, G. X., and Zhang, X.-C., 'Near-field terahertz imaging with a dynamic aperture', Opt. Lett. 25, pp. 1122-24 (2000).

Cheville, R. A., and Grischkowsky, D., 'Far-infrared foreign and self-broadened rotational linewidths of high-temperature water vapor', J. Opt. Soc. Am. B 16, pp. 317-22 (1999).

Chin, A., Chan, W. J., Ganikhanov, F., Lin, G.-R., Shieh, J.-M., Pan, C.-L., and Hsieh, K. C., 'Microstructure and subpicosecond photoresponse in GaAs grown by molecular beam epitaxy at very low temperatures', Appl. Phys. Lett. 69, pp. 397-99 (1996).

Corchia, A., Ciesla, C. M., Arnone, D. D., Linfield, E. H., Simmons, M. Y., and Pepper, M., 'Crystallographic orientation dependence of bulk optical rectification', J. Modern Opt. 47, pp. 1837-45 (2000).

Danzebrink, H. U., Castiaux, A., Girard C., Bouju, X., and Wilkening, G., 'Transmission scanning near-field optical microscopy with uncoated silicon tips', Ultramicroscopy 71 pp. 371-77 (1998).

Doany, F. E., Grischkowsky, D., and Chi, C.-C. 'Carrier lifetime versus ion-implantation dose in silicon on sapphire', Appl. Phys. Lett. 50, pp. 460-62 (1987).

Durig, U., Pohl, D. W., and Rohner, F., 'Near-field optical-scanning microscopy', J. Appl. Phys. 59, pp. 3318-27 (1986).

Erlig, H., Wang, S., Azfar, T., Udupa, A., Fetterman, H. R., and Streit, D. C., 'LT-GaAs detector with 451 fs response at 1.55 μm via two-photon absorption', Electron. Lett. 35, pp. 173-75 (1999).

Exter, M. V., and Grischkowsky, D. R., 'Characterization of an optoelectronic terahertz beam system', IEEE Trans. Microwave Theor. and Tech. 38, pp1684-91 (1990).

Feng, S., Winful, H. G., Hellwarth, R. W., 'Gouy shift and temporal reshaping of focused single-cycle electromagnetic pulses', Opt. Lett. 23, pp. 385-87 (1998).

Gallot, G., and Grischkowsky, D., 'Electro-optic detection of terahertz radiation', J. Opt. Soc. Am. B 16, pp. 1204-12 (1999).

Ganikhanov, F., Lin, G.-R., Chan, W.-C., Chang, C.-S., and Pan, C.-L., 'Subpicosecond carrier lifetime in arsenic-ion-implanted GaAs', Appl. Phys. Lett. 67 (1995).

Girard C., 'Transmittance of subwavelength optical tunnel junctions', Phys. Rev. B 58, pp. 12551-54 (1998).

Gupta, S., Frankel, M. Y., Valdmanis, J. A., Whitaker, J. F., Mourou, G. A., Smith, F. W., and Calawa, A. R., 'Subpicosecond carrier lifetime in GaAs grown by

molecular beam epitaxy at low temperatures', Appl. Phys. Lett. 59, pp. 3276-78 (1991).

Grenier, P., and Whitaker, J. F., Subband gap carrier dynamics in low-temperature-grown GaAs', Appl. Phys. Lett. 70, pp. 1998-2000 (1997).

Grischkowsky, D. R., Keiding, S., van Exter, M., and Fattinger, C., 'Far-infrared time-domain spectroscopy with terahertz beams of dielectrics and semiconductors', J. Opt. Soc. Am. B 7, pp. 2006-15 (1990).

Grischkowsky, D. R., 'Optoelectronic characterization of transmission lines and waveguides by terahertz time-domain spectroscopy', IEEE JST Quantum Electron. 6, pp. 1123-35 (2000).

Grober, R. D., Rutherford, T., and Harris, T. D., 'A modal approximation for the electromagnetic field of a near-field optical probe', Appl. Opt. 35, pp. 3488-95 (1996).

Harmon, E. S., Melloch, M. R., Woodall, J. M., Nolte, D. D., Otsuka, N., and Chang, C. L., 'Carrier lifetime versus anneal in low temperature growth GaAs', Appl. Phys. Lett. 63, pp. 2248-50 (1993).

Hochman, A., Paneah, P., and Leviatan, Y., 'Interaction between a waveguide-fed narrow slot and a nearby conducting strip in millimeter-wave scanning microscopy', J. Appl. Phys. 88, pp. 5987-92 (2000).

Hu, B. B, Weling, A. S., Auston, D. H., Kuznetsov, A. V., and Stanton, C. J., 'dc-electric field dependence of THz radiation induced by femtosecond optical excitation of bulk GaAs', Phys. Rev. B 49, pp. 2234-37 (1994).

Hu, B. B., and Nuss, M. C., 'Imaging with terahertz waves,' Opt. Lett. 20, pp. 1716-19 (1995).

Huber, R., Brodschelm, A., Tauser, F., and Leitenstorfer, A., 'Generation and field-resolved detection of femtosecond electromagnetic pulses tunable up to 41 THz', Appl. Phys. Lett. pp. 3191-93 (2000).

Hultgren, C. T., Dougherty, D. J., and Ippen, E. P., 'Above- and below-band femtosecond nonlinearities in active AlGaAs waveguides', Appl. Phys. Lett. 61, pp. 2767-69 (1992).

Hunsche, S., Koch, M., Brener, I., and Nuss, M. N., 'THz near-field imaging', Opt. Comm. 150, pp. 22-26 (1998).

Janz, S., Akano, U. G., and Mitchell, I. V., 'Nonlinear optical response of $As^+$-ion implanted GaAs studied using time resolved reflectivity', Appl. Phys. Lett. 68, pp. 3287-89 (1996).

Jackson, J. D., Classical electrodynamics (John Wiley & Sons, New York, 1962).

Khurgin, J. B., 'Optical rectification and terahertz emission in semiconductors excited above the band gap', J. Opt. Soc. Am. B 11, pp. 2492-01 (1994).

Knoll, B., and Keilmann, F., 'Enhanced dielectric contrast in scattering-type scanning near-field optical microscopy', Opt. Comm. 182, pp. 321-28 (2000).

Kuznetsov, A. V., Kim, C. S., and Stanton, C. J., 'Theory of the generation and detection of carriers in ultrafast pump-and-probe spectroscopy of semiconductors', J. Appl. Phys. 80, pp. 5899-908 (1996).

Kwan, T. J. T. and Peter, W., 'Microwave propagation through an apertured coaxial waveguide', Phys. Rev. A 38, pp. 4743-51 (1988).

Leitenstorfer, A., Hunsche, S., Shah, J., Nuss, M. C., and Knox, W. H., 'Femtosecond high-field transport in compound semiconductors', Phys. Rev. B 61, pp. 16642-52 (2000).

Leviatan, Y., 'Study of near-zone fields of a small aperture', J. Appl. Phys. 60, pp. 1577-83 (1986).

Liliental-Weber, Z., Cheng, H. J., Gupta, S., Whitaker, J., Nichols, K., and Smith, F. W., 'Structure and carrier lifetime in LT-GaAs', J. Electron. Mater. 22, pp. 1465-69, (1993).

Liu, X., Prasad, A., Chen, W. M., Kurpiewski, A., Stoschek, A., Liliental-Weber, Z., and Weber, E. R., 'Mechanism responsible for the semi-insulating properties of low-temperature-grown GaAs', Appl. Phys. Lett. 65, pp. 3002-04 (1994).

Lochtefeld, A. J., Melloch, M. R., Chang, C. L., and Harmon, E. S., 'The role of point defects and arsenic precipitates in carrier trapping and recombination in low-temperature grown GaAs', Appl. Phys. Lett. 69, pp. 1465-67 (1996).

Loka, H. S, Benjamin, S. D., and Smith, P. W. E., 'Optical characterization of low-temperature-grown GaAs for ultrafast all-optical switching devices', IEEE J. Quantum Electron. 34, pp. 1426-37 (1998).

Look, D. C., Walters, D. C., Manasreh, M. O., Sizelove, J. R., Stutz, C. E., and Evans, K. R., 'Anomalous Hall-effect results in low-temperature molecular-beam-epitaxial GaAs: Hopping in a dense EL2-line band', Phys. Rev. B 42, pp. 3578-81 (1990).

Markelz, A. G., Roitberg, A., and Heilweil, E. J., 'Pulsed terahertz spectroscopy of DNA, bovine serum albumin and collagen between 0.1 and 2.0 THz', Chem. Phys. Lett. 320, pp. 42-8 (2000).

Martin, O. J. F., Girard, C., and Dereux, A., 'Generalized Field Propagator for Electromagnetic Scattering and Light Confinement', Phys. Rev. Lett. 74, pp. 526-29 (1995).

Melloch, M. R., Otsuka, N., Woodall, J. M., Warren, A. C., and Freeouf, J. L., 'Formation of arsenic precipitates in GaAs buffer layers grown by molecular beam epitaxy at low substrate temperatures', Appl. Phys. Lett. 57, pp 1531-33 (1990).

Mittleman, D.M., Gupta, M., Neelamani, R., Baraniuk, R.G., Rudd. J.V., and Koch, M., "Recent advances in terahertz imaging," Appl. Phys. B 68, pp. 1085-94 (1999).

Moller, K. D., Farmer, K. R., Ivanov, D. V. P., Sternberg, O., Stewart, K. P., and Lalanne, P., 'Thin and thick cross shaped metal grids', Infrared Phys. & Tech. 40, pp. 475-85 (1999).

Moon, E.-A., Lee, J.-J., and Yoo, H. M., 'Selective wet etching of GaAs on $Al_xGa_{1-x}As$ for AlGaAs/InGaAs/AlGaAs pseudomorphic high electron mobility transistor', J. Appl. Phys. 84, pp. 3933-38 (1998).

Nahata, A., and Heinz, T. F., 'Reshaping of freely propagating terahertz pulses by diffraction', IEEE JST Quantum Electron. 2, pp. 701-8 (1996).

Novotny, L., Pohl, D. W., and Regli, P., 'Light propagation through nanometer-sized structures: the two-dimensional-aperture scanning near-field optical microscope', J. Opt. Soc. Am. A 11, pp. 1768-79 (1994).

Novotny, L., Hecht, B., and Pohl, D. W., 'Implications of high resolution to near-field optical microscopy', Ultramicroscopy 71, pp. 341-44 (1998). The original paper carries a mistake in Eqs. 4-6.

Nuss, M. C. and Orenstein, J., 'Terahertz time-domain spectroscopy', in: G. Gruner (Ed.), 'Millimeter-wave spectroscopy of solid', Springer Topics in Applied Physics, vol. 74 (Springer, Berlin 1998).

Planken, P. C. M., Nuss, M. C., Knox, W. H., Miller, D. A. B., and Goossen, K. W., 'THz pulses from the creation of polarized electron-hole pairs in biased quantum wells', Appl. Phys. Lett. 61, pp. 2009-11 (1992).

Pohl, D. W., 'Scanning near-field optical microscopy', in Advances in optical and electron microscopy (Academic, New York, 1991).

Reddick, R. C., Warmack, R. J., and T. L. Ferrell, 'New form of optical microscopy', Phys. Rev. B 39, pp. 767-70 (1989).

Reynolds, G. O., DeVelis, J. B., Parrent, Jr., G. B., and Thompson, B. J., Physical Optics Notebook: tutorials in Fourier optics (SPIE Optical Engineering Press, 1989).

Roberts, A., 'Near-zone field behind circular apertures in thick, perfectly conducting screens', J. Appl. Phys. 65, pp. 2896-99 (1989).

Roberts, A., 'Small-hole coupling of radiation into a near-field probe', J. Appl. Phys. 70, pp. 4045-49 (1991).

Segschneider, G., Dekorsy, T., Kurz, H., Hey, R., and Ploog, K., 'Energy resolved ultrafast dynamics close to the band edge of low-temperture grown GaAs', Appl. Phys. Lett. 71, pp. 2779-81 (1997).

Siegner, U., Fluck, R., Zhang, G., and Keller, U., 'Ultrafast high-intensity nonlinear absorption dynamics in low-temperature grown gallium arsenide', Appl. Phys. Lett. 69, 2566-68 (1996).

Smith, P. W. E., Benjamin, S. D., and Loka, H. S, 'Tailoring of trap-related carrier dynamics in low-temperature-grown GaAs', Appl. Phys. Lett. 71, pp. 1156-58 (1997).

Son, J.-H., Norris, T. B., and Whitaker, J. F., 'Terahertz electromagnectic pulses as probes for transient velocity overshoot in GaAs and Si', J. Opt. Soc. Am. B 11, pp. 2519-27 (1994).

Sosnowski, T. S., Norris, T. B., Wang, H. H., Grenier, P., and Whittaker, J. F., 'High-carrier density electron dynamics in low-temperature-grown GaAs', Appl. Phys. Lett. 70, pp. 3245-47 (1997).

Taflove, A. and Hagness, S., Computational Electrodynamics: The Finite-Difference Time-Domain Method (Artech House, New York 2000).

Tani, M., Lee, K.-S., and Zhang, X.-C., 'Detection of terahertz radiation with low-temperature-grown GaAs based photoconductive antenna using 1.55 mm probe', Appl. Phys. Lett. 77, pp. 1396-98 (2000).

You, D., Bucksbaum, P. H., ' Propagation of half-cycle far infrared pulses', J. Opt. Soc. Am. B 14, pp. 1651-55 (1997).

Valle, P. J., Moreno, F., Saiz, J. M., and Gonzalez, F., 'Near-field scattering from subwavelength metallic protuberances on conducting flat substrates', Phys. Rev. B 51, pp. 13681-90 (1995).

Valle, P. J., Greffet, J.-J., and Carminati, R., 'Optical contrast, topographic contrast and artifacts in illumination-mode near-field optical microscopy', J. Appl. Phys. 86, pp. 648-56 (1999).

Vasilyeva, E., and Taflove, A., 'Three-dimensional modeling of amplitude-object imaging in scanning near-field optical microscopy', Opt. Lett. 23, pp. 1155-57 (1998).

Warren, A. C., Woodall, J. M., Freeouf, J. L., Grischkowsky, D., Melloch, M. R., and Otsuka, N., 'Arsenic precipitates and the semi-insulating properties of GaAs buffer layers grown by low-temperature molecular beam epitaxy', Appl. Phys. Lett. 57, pp. 1331-33 (1990).

Weeber, J.-C., Bourillot, E., Dereux, A., Goudonnet, J.-P., Chen, Y., and Girard, C., 'Observation of light confinement effects with a near-field optical microscope', Phys. Rev. Lett. 77, pp. 5332-35 (1996).

Wynne, K. and Jaroszynski, D. A., 'Superluminal terahertz pulses', Opt. Lett. 24, pp. 25-27 (1998).

Wynne, K., Carey, J.J., Zawadzka, J., and Jaroszynski, D.A., 'Tunneling of single-cycle terahertz pulses through waveguides', Opt. Comm. 176, pp. 429-35 (2000).

Zhang, X.-C., Hu, B. B., Darrow, J. T., and Auston, D. H., 'Generation of femtosecond electromagnetic pulses from semiconductor surfaces', Appl. Phys. Lett. 56, pp. 1011-13 (1990).

Zucker, F. J., 'Surface and leaky wave antennas', in Jasik, H. J. (Ed.), Antenna Engineering Handbook, (McGraw Hill Book Company, New York 1961).